

**On Binary Asteroids: Dynamics, Formation and Parameter
Estimation**

by

Alex B. Davis

BSc Aeronautical and Astronautical Engineering, Purdue University 2015

MSc Aerospace Engineering, University of Colorado 2017

A thesis submitted to the
Faculty of the Graduate School of the
University of Colorado in partial fulfillment
of the requirements for the degree of
Doctor of Philosophy
Department of Aerospace Engineering Sciences
2020

Committee Members:

Daniel J. Scheeres

Prof. Jay W. McMahon

Prof. Hanspeter Schaub

Prof. Natasha Bosanac

Prof. Elizabeth Bradley

Davis, Alex B. (Ph.D., Aerospace Engineering)

On Binary Asteroids: Dynamics, Formation and Parameter Estimation

Thesis directed by Prof. Daniel J. Scheeres

Binary asteroids make up roughly 16% of the near Earth and Main Belt asteroid populations, while an estimated 50% of Kuiper Belt objects are believed to be binary or multi-body systems. Their abundance and unique dynamics have gained the interest of planetary scientists and mission planners alike as potential targets for future study and exploration. Several missions to binaries have already been announced, such as the DART and Hera missions to Didymos, the Lucy mission flyby of Jupiter Trojan 617 Patroclus, and the Janus mission flybys of 1996 FG3 and 1991 VH. The success of these missions and others will require a thorough understanding of binary dynamics, their formation processes, and robust navigation techniques. This thesis attempts to expand the toolsets available for the study and exploration of binary systems by implementing high fidelity dynamics models, exploring their dynamical structure, formation processes, mass parameter observability, and navigation approaches. We begin by developing an arbitrary shape and order implementation of the coupled attitude and orbit dynamics of binary asteroids, otherwise known as the Full Two-Body Problem (F2BP). Dynamical systems theory techniques are then applied to identify the equilibria of the F2BP and their associated dynamical structure. We apply these dynamical tools first to binary asteroid formation and evolution; where we study the statistical fate of a representative set of low and high mass ratio binary asteroids as they evolve from their initial fission. Next the sensitivity of the stable doubly synchronous equilibrium to the binary mass parameters is investigated to understand the remote observability of mass parameters from measurements of the binary dynamics alone. Finally, a consider covariance analysis is developed for an in-situ spacecraft estimating the masses, inertias, and higher order parameters of a target binary.

Throughout the thesis we identify many new behaviors of these complex dynamical systems and propose new techniques for their study. We first identify and map the manifolds about the

stable doubly synchronous equilibrium and characterize the breakdown of the unstable doubly synchronous equilibrium as barrier to recollision and successful binary fission. In the area of binary formation and evolution we note the importance of nonplanar dynamics in the fate of ejected secondary asteroids and the fission of captured secondaries. We prove the mathematical feasibility of remote mass parameter estimation, while identifying technical challenges that may limit its implementation. Expanding this analysis to an in-situ spacecraft, we are able to characterize the sensitivity of the dynamics to estimated mass parameters; identifying trends and characteristics in their relative importance and effect.

Dedication

For all who sacrificed so that I could reach this moment;
my parents, Beth and David, chief amongst them.

Also to my brother, Spencer, and the friends who helped along the way.

Acknowledgements

First and foremost, I'd like to thank my advisor, Prof. Dan Scheeres. I am sincerely grateful for the opportunity to work with you and the guidance and advice you provided along the way. Your vision and support helped me to find my own research interests and pursue them despite the challenges. Thanks also go to my committee members: Prof. Bosanac, Prof. Bradley, Prof. McMahon, and Prof. Schaub. Each of you played an important role in shaping the many aspects of my research. To the other professors, teachers, and mentors I have had during, and before, my time at CU goes my gratitude.

Special thanks also goes to my many mentors and colleagues throughout my internships at JPL: Ryan Park, Steve Chesley, Davide Farnocchia, Yu Takahashi, Gene Farnestock, and Eric Gustafson amongst others. Your support and advice helped me to grow as a researcher and provided me with invaluable experiences. For the same reasons, I thank my colleagues on the DART, Hera, and OSIRIS-REx missions.

I cannot begin to thank my parents, Beth and David, enough for their unwavering support throughout all my endeavors. You have helped me maintain my sanity and my passion through all the highs and lows. I could ask for nothing more. I thank my brother, Spencer, for your excitement, commiseration, and helping shape me into the person I am today. Thanks also to Katie for helping me grow as a person and the constant supply of videos and pictures of my nephew, Art.

Thank you to my friends at CU for all the fun times. Thanks in particular to Andrew, Stef, Samm, Ben, Dan, CK, Nicola, and David. My gratitude to Matt, Kevin, Cat, and Luke for your friendship and many good times throughout the years. To the members of CSML and CCAR

your camaraderie and collaboration will always be remembered and appreciated. I look forward to sharing food, drink and merriment with all of you soon.

Thanks to the NSF GRFP for the funding and recognition that helped to make this experience what it was.

Lastly, I wish to acknowledge that this work was completed on indigenous land, formerly of the Ute, South Arapaho, and other tribes.

Contents

Chapter	
1	Introduction 1
1.1	The Full Two-Body Problem 2
1.2	Formation and Evolution 3
1.3	Remote Estimation 5
1.4	In-Situ Estimation 6
1.5	Contributions 7
1.5.1	Journal Papers 7
1.5.2	Conference Papers, Talks, and Posters 8
1.5.3	Software 10
1.6	Thesis Organization 10
2	Dynamics of the Full Two-Body Problem 13
2.1	The Full Two-Body Problem 13
2.1.1	The Mutual Gravity Potential 14
2.1.2	Inertia Integrals 16
2.1.3	Gravity Accelerations and Torques 17
2.1.4	Equations of Motion 19
2.2	Model Verification and Benchmarking 20
2.2.1	Dynamical Accuracy Benchmarking 21

2.2.2	Simulation Runtime Benchmarking	24
2.3	Summary	25
3	The Equilibria and Dynamical Structure of the Full Two-Body Problem	27
3.1	Doubly Synchronous Equilibria of the Full Two-Body Problem	27
3.2	Stability and Structure about the Outer Equilibrium	30
3.2.1	The Planar Problem	31
3.2.2	Linear System Dynamical Families	33
3.2.3	Continuation of the Planar Dynamical Families	34
3.2.4	Expansion to the Nonplanar Problem	40
3.3	Stability and Structure about the Inner Equilibrium	41
3.4	Summary	44
4	Binary Formation Via Rotational Fission At the Inner Unstable Equilibrium	46
4.1	Perturbed Dynamics Model	47
4.1.1	Tidal Torques	48
4.1.2	Solar Gravity	49
4.1.3	Secondary Fission	49
4.2	Simulation Methodology	50
4.3	Moshup (1999 KW4)	52
4.3.1	Recollision	53
4.3.2	Secondary Fission	56
4.3.3	Escape	59
4.3.4	Chaotic Orbital Capture	63
4.4	1996 HW1	63
4.4.1	Recollision	66
4.4.2	Escape	68
4.4.3	Chaotic Orbital Capture	72

4.4.4	Effects of Increasing Fission Spin Rate	73
4.5	2000 DP107	74
4.5.1	Recollision	76
4.5.2	Further Analysis of Secondary Fission	78
4.5.3	Higher Energy Formation	78
4.6	Broad Comparison to Past Work	80
4.7	Summary	82
5	Remote Estimation of Doubly Synchronous Binary Asteroid Mass Parameters	84
5.1	Mass Parameter Estimation in the Planar Problem	84
5.1.1	Numerical Sensitivity of Dynamical Families to the Mass Parameters	85
5.1.2	Planar Estimation	88
5.2	Mass Parameter Estimation in the Nonplanar Problem	92
5.2.1	Dynamical Oscillation Constrained Estimation	92
5.2.2	An Idealized Estimation Method	94
5.2.3	Scaling with Ellipsoidal Shape	96
5.3	Near-Spherical Doubly Synchronous Systems	100
5.4	Summary	104
6	A Covariance Study for Gravity Estimation at Binary Asteroids	106
6.1	The Restricted Full Three-Body Problem	107
6.1.1	Equations of Motion	107
6.1.2	Partial Matrices	108
6.2	Consider Covariance Filter	110
6.2.1	Measurement Update	111
6.2.2	Time Update	112
6.2.3	Measurement Model	113
6.3	Application to 65803 Didymos	114

6.3.1	Consideration of Mass and Inertia	116
6.3.2	Consideration of Higher Order Terms	120
6.3.3	Separating Direct and Indirect Effects of Mass Parameters on the Spacecraft	122
6.3.4	Effects of Excited Mutual Dynamics	123
6.4	Summary	125
7	Conclusion	127
	Bibliography	132
	Appendix	
A	Full Two-Body Problem Partial Matrices	138
A.1	Planar Dynamics Matrix	138
A.2	Nonplanar Dynamics Matrix	141
A.3	Total Mass Partial of Nonplanar Dynamics Matrix	143
A.4	Second Order Inertia Integral Partial of Nonplanar Dynamics Matrix	144
B	Restricted Full Three-Body Problem Partial Matrices	147
B.1	Dynamics Matrix	147
B.2	Mass Parameter Partial Matrix	149
B.3	Observation-State Matrix	151
B.4	Observation-Consider Parameter Matrix	152
C	General Use Binary Asteroid Simulator	154

Tables

Table

2.1	Fractional error in mutual gravity potential evaluated by the polyhedral expansion method and inertia integral method for orders 2-7.	22
2.2	Normalized runtimes for a variety of mutual gravity potential methods integrating the Didymos system for 365 days.	24
3.1	Physical Properties of The Doubly Synchronous 617 Patroclus modeled in this study	30
3.2	Linear periods and unit direction of dynamical families about the planar doubly synchronous equilibrium evaluated for the 617 Patroclus system.	34
3.3	Linear periods of dynamical families about the nonplanar doubly synchronous equilibrium evaluated for the 617 Patroclus system.	41
4.1	Current observed Moshup States based on Ostro et al[1].	52
4.2	Monte Carlo conditions for Moshup analysis.	52
4.3	Statistical results for Moshup formation simulations	53
4.4	Comparison of secondary fission results for different models of fission for Moshup Simulations.	58
4.5	Current observed 1996 HW1 based on observations by Magri et al. and Howell et al[2][3].	64
4.6	Monte Carlo conditions for the HW1 analysis.	65
4.7	Statistical results for HW1 formation simulations	65

4.8	Statistical results for 4 hour fission period HW1 formation simulations	74
4.9	Current observed 2000 DP107 States based on Naidu et al while the mass parameters are based on a constant density evaluation of the radar shape model assuming the measured density of 1.38 g/cm^3 [4].	74
4.10	Monte Carlo conditions for the DP107 analysis.	75
4.11	Statistical results for DP107 formation simulations	76
4.12	Statistical results for DP107 formation simulations with the bi-lobed secondary fission model and a secondary mass fraction of 0.5	78
4.13	Wide Monte Carlo conditions for the DP107 analysis. We sample uniformly between the upper and lower perturbation bounds.	79
4.14	Comparison of secondary fission results for faster spin rate and wider perturbation Monte Carlo analyses of DP107.	79
5.1	Allowable observational variance of observations for 10% certainty of mass parameter estimates of the 617 Patroclus system.	95
5.2	Linear periods of dynamical families about the nonplanar doubly synchronous equilibrium evaluated for the spherical Pluto-Charon system. DNE, does not exist, is used to denote frequencies which cease to be periodic for the two sphere system	102
5.3	Linear periods of dynamical families about the nonplanar doubly synchronous equilibrium evaluated for the $\epsilon=.0008$ Pluto-Charon system.	104
6.1	Current Observed 65803 Didymos orbit parameters and spin state.	115
6.2	Current ellipsoidal dimensions for 65803 Didymos [5]	115
6.3	Perturbed Didymos secondary spin and orbit state	115

Figures

Figure

2.1	System diagram of the Full Two- Body Problem.	14
2.2	Fractional error between JPL polyhedral expansion and UCB inertia integral numerical integrations using identical LGVI integrators.	23
3.1	Diagram of the planar and second-order F2BP.	31
3.2	Nonlinear dynamical family about the planar doubly synchronous equilibrium associated with the primary phase angle, ϕ_1 . Where ΔE is the increase in energy away from the equilibrium energy.	37
3.3	Nonlinear dynamical family about the planar doubly synchronous equilibrium associated with the secondary phase angle, ϕ_2 . Where ΔE is the increase in energy away from the equilibrium energy.	38
3.4	Nonlinear dynamical family about the planar doubly synchronous equilibrium associated with the relative separation, r . Where ΔE is the increase in energy away from the equilibrium energy.	39
3.5	Diagram of the nonplanar doubly synchronous equilibrium and surrounding linear dynamical families.	40
3.6	Diagram from Scheeres 2009 which depicts the energy of a second order planar ellipsoid-ellipsoid binary as a function of the primary's radius for a fixed angular momentum[6].	42

3.7	Relative geometry of inner unstable equilibrium evaluated at order 2 (above) and order 4 (below).	43
3.8	Relative separation of Moshup dynamics when perturbed slightly from inner equilibrium state evaluated for the given order of the dynamics.	44
4.1	Fission conditions for modeled asteroids with primaries colored grey and secondaries colored blue. From left to right: Moshup, 1996 HW1, 2000 DP107	47
4.2	Location of impact locations for collision cases shown in the body fixed frame of the Moshup primary.	54
4.3	Instantaneous surface velocities of colliding secondaries at the moment of impact for Moshup simulations.	55
4.4	Complex spin state of the secondary at the moment of secondary fission for Moshup Simulations.	57
4.5	Complex spin state of the secondary at the moment of secondary fission using the bi-lobed secondary fission model with $\nu_s=0.5$ for Moshup Simulations.	60
4.6	Magnitude of relative velocity as the secondary crosses the primary's sphere of influence for Moshup Simulations. The sphere of influence for the Moshup primary is 10370 meters.	61
4.7	Complex spin state of the secondary at the moment of escape for Moshup Simulations.	61
4.8	Complex spin state of the primary at the moment of secondary escape for Moshup Simulations.	62
4.9	Complex spin state of the secondary in chaotically captured cases after one year of integration for Moshup Simulations.	63
4.10	Split lobes of current 1996 HW1 geometry[7].	64
4.11	Location of impact locations for collision cases shown in the body fixed frame of the HW1 primary.	66
4.12	Evolution of the relative separation in a colliding case for HW1 simulations.	67

4.13	Instantaneous surface velocities of colliding secondaries at the moment of impact for HW1 simulations.	68
4.14	Complex spin state of the primary at the moment of secondary escape for HW1 simulations.	69
4.15	Complex spin state of the secondary at the moment of secondary escape for HW1 simulations.	70
4.16	Magnitude of relative velocity as the secondary crosses the primary's sphere of influence for HW1 simulations. The sphere of influence for the HW1 primary is 28951 meters.	70
4.17	Example of angular momentum transfer in the HW1 system.	71
4.18	Complex spin state of the primary in chaotically captured cases after one year of integration for HW1 simulations.	72
4.19	Complex spin state of the secondary in chaotically captured cases after one year of integration for HW1 simulations.	73
4.20	Relative geometry of the initial geometry at fission for DP107.	75
4.21	Location of impact locations for collision cases shown in the body fixed frame of the DP107 primary.	76
4.22	Instantaneous surface velocities of colliding secondaries at the moment of impact. . .	77
5.1	Behavior of planar doubly synchronous dynamical family linear periods as the density of the system is scaled.	86
5.2	Behavior of planar doubly synchronous dynamical family linear periods as the volume of each body is scaled.	86
5.3	Behavior of planar doubly synchronous dynamical family linear periods as the length of each ellipsoid axis is scaled.	87
5.4	Projection of planar mass parameter estimates onto the solution nullspace plane. . .	91

5.5	Effects of secondary mass parameter scaling on mass parameter covariance matrix with magnitude of matrix elements shown in log color.	98
5.6	Effects of secondary mass parameter scaling on mass parameter correlation matrix with magnitude of matrix elements shown in linear color.	99
5.7	Linearized change in Pluto-Charon dynamical family periods as shape is modified by ϵ parameter.	103
6.1	Diagram of RF3BP geometry.	107
6.2	Terminator and retrograde orbits in the Didymos rotating frame over a 24 hour period.	116
6.3	Relative position and velocity of binary state error(blue), 1 sigma covariance(red) and 1 sigma consider covariance(black) for T_B^{200} based on a spacecraft in a terminator orbit.	117
6.4	Values of the 1 sigma consider covariance after 24 hours. Results for the the masses and second order inertia integrals of both asteroids considering a spacecraft in the terminator and retrograde orbits.	118
6.5	Spacecraft state 1 sigma consider covariance for each considered mass parameters based on a spacecraft in a retrograde orbit.	119
6.6	Values of the 1 sigma consider covariance after 24 hours. Results for the the masses and second order inertia integrals of both asteroids considering a spacecraft in the terminator and retrograde orbits both with and without DSN measurements.	119
6.7	Values of the 1 sigma consider covariance after 24 hours. Results for all mass parameters of the primary considering a spacecraft in the terminator and retrograde orbits.	121
6.8	Values of the 1 sigma consider covariance after 24 hours. Results for all mass parameters of the secondary considering a spacecraft in the terminator and retrograde orbits.	121

6.9	Values of the 1 sigma consider covariance after 24 hours. Results for all mass parameters of the primary considering a spacecraft in the terminator and retrograde orbits.	123
6.10	Values of the 1 sigma consider covariance after 24 hours. Results for all mass parameters of the secondary considering a spacecraft in the terminator and retrograde orbits.	123
6.11	Values of the 1 sigma consider covariance after 24 hours. Results for all mass parameters of the primary considering a spacecraft in the terminator and retrograde orbits.	124
6.12	Values of the 1 sigma consider covariance after 24 hours. Results for all mass parameters of the secondary considering a spacecraft in the terminator and retrograde orbits.	125
C.1	General Use Binary Asteroid Simulator Software Flowchart	155

Chapter 1

Introduction

In 1993 the Galileo spacecraft discovered the first binary asteroid system during its flyby of asteroid Ida. A small satellite body, Dactyl, was identified in spacecraft images and determined to be an asteroid satellite[8]. In the interim a number of binary asteroids have been identified, including 48 Trans-Neptunian binaries and approximately 16% of near-Earth asteroids (NEAs)[9][10][11]. It is now believed that most small body populations contain a significant number of binary asteroid systems as well as more complex multi-body systems[12]. Despite these discoveries, the Ida and Dactyl system remains the only binary asteroid visited by a spacecraft. Binary asteroids largely fall into two categories, the doubly synchronous configuration, which generally consists of two similarly sized bodies both tidally locked to each other, and the singly synchronous systems in which a smaller secondary asteroid is tidally locked to the primary, while the primary spins freely. Due to their prevalence, questions about their formation, and potential insight they may provide into solar system formation, the scientific community has voiced a growing interest in exploring binary asteroid systems [13][10]. As a result of this interest a growing number of missions have begun targeting binaries, requiring the engineering community to understand how to safely and effectively interact with these unique systems. Flyby missions like NASA's Lucy or Janus missions will need the tools to remotely observe and measure these systems, while impactor and orbiter missions like NASA's DART mission or ESA's Hera mission will need to orbit, navigate, and estimate parameters of these systems[14][15][16]. In preparation for these missions, the dynamical environment around binary asteroids, as well as, remote and in-situ estimation of binaries will need

to be well understood. In this thesis we seek to understand fundamental questions of the dynamics, formation and estimation of binary asteroid systems. This leads to the thesis of this work:

Thesis Statement: High fidelity modeling and estimation of binary asteroid systems will enable a better understanding of their formation and evolution, more robust mission planning to, and safer navigation about these systems; providing the tools necessary to produce valuable science when exploring these systems.

1.1 The Full Two-Body Problem

The study of F2BP dynamics have their roots in the study of the Earth-Moon system beginning with Cassini's laws, and later the attitude of Earth-orbiting spacecraft, both of which experience the translational and rotational coupling characteristic of the F2BP [17][18][19]. While binary asteroids had been theorized in the intervening years, only after the Ida-Dactyl encounter was the standard form of the F2BP, as it applies to binary asteroids, developed by Maciejewski. In this formulation, both bodies are treated as two rigid, arbitrarily shaped mass distributions whose complex mutual gravity potential results in coupled orbit and attitude of their relative dynamics [20]. Maciejewski's dynamical model was unfortunately limited by the lack of an effective mutual gravity potential representation. This led to the development of a variety of high-fidelity mutual gravity potential formulations; chief among them the packed spheres method, the polyhedral expansion method and the inertia integral method. The packed spheres method represents the mass distributions of the two bodies as a collection of spherical masses, enabling the potential to be exactly modeled as that of the more standard N-body problem, while sacrificing the accuracy with which the mass distributions can be efficiently represented [21][22]. The polyhedral expansion method, proposed by Werner and Scheeres and developed further by Fahnestock and Scheeres, instead discretizes the bodies as polyhedra and expands the mutual gravity between each pairwise set of tetrahedra. In this way, the model is able to very accurately capture the mass distributions, but the attitude and mass distribution remain coupled, such that the mass distribution must be

re-evaluated for each evaluation of the mutual gravity potential [23][24]. In the inertia integral method, the mass distributions are modeled as inertia integrals up to some truncation order, which allows them to be initialized from any shape or discretization approach. The benefit of which is that the mass distribution can be accurately represented and decoupled from the attitude, providing increased computational efficiency. The development of the inertia integral method was independently begun by Tricarico, Ashenberg, and Boue and Laskar; while Ashenberg and Boue and Laskar both developed the inertia integral method as truncated expansions, Tricarico was able to develop a complex, but general formulation of the mutual gravity potential to arbitrary order [25][26][27]. In 2016, Hou et al. reformulated the inertia integral method using a recursive binomial expansion in such a way that the evaluation of the mutual gravity potential is orders of magnitude faster than previous mutual gravity potential formulations, while providing numerically identical accuracy to the polyhedral expansion method [28]. Building upon this model we have developed the General Use Binary Asteroid Simulator (GUBAS) as an open-source simulation tool for binary asteroids; it has been adopted by the DART and Hera mission teams[29].

1.2 Formation and Evolution

Binary asteroids are widely believed to be produced by Yarkovsky-O’Keefe-Radzievskii-Paddack (YORP) effect driven rotational fission of rubble pile asteroids[13][30]. A number of past studies have supported the plausibility of the YORP effect as the driving evolutionary process which led the asteroid population to its current dynamical richness. In general the proposed evolutionary pathway begins with YORP driven spinup of a rubble pile asteroid. Eventually, the asteroid spin rate exceeds some critical value, leading to mass-shedding or outright fission[13][31][32]. After fission the expelled mass coalesces into a secondary asteroid which either settles into a stable orbit about the primary asteroid, re-collides with the parent body, or escapes from the system and forms an asteroid pair.

This pathway was initially proposed as an explanation for observations of a wide range of asteroids by Pravec et al. who show an upper spin limit of about 2.2 hours throughout the

observed population [33][34]. In response theorists began to explore YORP spinup induced fission. Work by Scheeres explored YORP spinup as a driver for contact binary fission, while Walsh et al. studied YORP-driven rubble pile mass shedding as a formation process for binary asteroids [31][13]. Scheeres focused on contact binary fission, assuming the asteroid was initially two distinct bodies resting on one another. On the other hand Walsh et al. treated the asteroids as a collection of small spherical masses which would be shed from a single asteroid and then coalesce into the secondary asteroid. Both of these works showed the potential of YORP spin up to explain both the observed spin barrier of NEA's, as well as the dynamical complexity of observed NEA systems. However, the binary systems formed by both theories showed significant energetic excitement compared with the energetically relaxed binaries commonly observed amongst NEA's. This required a powerful source of energy dissipation to match these predictions to the observed population. Work by Jacobson and Scheeres (JS2011) explored the potential sources of this energy dissipation. They modeled the post-fission dynamics for the contact binary case with a simplified gravity model, the effects of solar gravity, tidal torques, and the cohesive strength of the secondary asteroid. Their work identified secondary fission, or structural failure of the secondary, driven by mutual momentum transfer between the asteroids as a powerful source of energy dissipation for low mass ratio systems ($\lesssim 0.2$). For larger mass ratio systems the study suggested a slower relaxation into the doubly synchronous equilibrium, eventually evolving into a contact binary or asteroid pair. With these two processes their work was able to describe a complete evolutionary map for NEA binaries, asteroid pairs, and other NEA systems [30]. However, their analysis ignored both nonplanar effects and higher order gravity terms. Later work by Boldrin et al. did begin to investigate the effects of nonplanar dynamics, but limited their investigation to the formation of contact binaries[35].

Since the JS2011 analysis, the computational efficiency of binary asteroid dynamics models has improved significantly. Within this thesis we apply more rigorous dynamics models to past studies in order to understand how their conclusions may be affected. Of particular interest for our analysis are the expected formation rates and conditions for the most common multi-body asteroid system categories. The categories of interest here are asteroid pairs, contact binaries, low

mass ratio binaries, and high mass ratio binaries. In this nomenclature asteroid pairs are defined as a collection of two or more bodies which can be shown to have similar orbit elements and to have had small relative velocities and separations in the past. It has been suggested that asteroid pairs form after the fission of a parent body similar to observations of P/2013 R3 [36]. Contact binaries are defined as bi-lobed asteroids which appear to be two distinct bodies resting on one another. Examples are Itokawa and 1996 HW1[37][3]. The binary asteroid population of the NEAs are commonly separated into low mass ratio and high mass ratio binaries. Low mass ratio binaries are defined to have a mass ratio below 0.2, but tend towards a mass ratio of 0.05 with a top-shaped primary, similar to Moshup (1999 KW4) and 65803 Didymos[1][38]. The majority of low mass ratio binaries also exhibit a singly synchronous arrangement where the smaller secondary is tidally locked and the primary has a nearly constant spin rate. High mass ratio binaries on the other hand tend towards bodies of similar size, such as 1994 CJ1 and 2017 YE5[39][40]. The dynamics of these systems tend instead toward the doubly synchronous equilibrium where both bodies are tidally locked. In addition to these multi-body asteroid categories, we are also interested in the source of the equatorial craters seen on 2000 DP107 and 2008 EV5 and the potential for these to be the result of a fission event[41]. While both JS2011 as well as Walsh et al 2008. provided constraints to the formation of these various objects, the aim of this work is to further constrain and explore the feasibility of these formation processes.

1.3 Remote Estimation

As observers and spacecraft begin to study binary systems in more detail from afar, it is important to understand how the mass parameters may influence the observed dynamics and affect assumptions made about the system behavior. We analyze these effects by applying estimation techniques based on observational measurements of translational and rotational coupling to constrain the asteroid mass parameters. Such an approach, while unprecedented for binary asteroids, has been leveraged during missions to small bodies and asteroid flybys of the Earth. Most notably, Takahashi and Scheeres used observations of the spin state of 4179 Toutatis during several Earth

flybys to estimate its moments of inertia[42]. At Vesta the Dawn mission was able to use the spacecraft’s orbital behavior to place constraints on the interior structure and mass distribution of Vesta and similar papers have used the same approach for the OSIRIS-Rex mission to Bennu[43][44]. Similarly, the ejecta observed by OSIRIS-REx at Bennu has been tracked by the spacecraft to independently measure the gravity field at Bennu[45][46]. Development of these capabilities for binaries would enable more reliable measurements and more robust mission planning for upcoming missions to binary asteroids. To understand the sensitivity of the binary systems to mass parameters we study the estimation of each mass parameter. To maintain simplicity of the investigation the simulated binary system is assumed to be in, or oscillating near, a doubly synchronous equilibrium, meaning both bodies are near tidally locked in a relaxed orbit about their mutual center of mass. We also assume knowledge of the center of mass and principal axes of the target bodies so as to better study the direct effects of the mass parameters themselves on the observable dynamics. Thus, we provide ideal limits on the estimation of the mass parameters based purely on observations of a binary system’s mutual motion.

1.4 In-Situ Estimation

Traditionally, in-situ spacecraft motion in binary asteroid systems is modeled as the restricted full three body problem (RF3BP). The RF3BP treats the spacecraft as a massless particle under the gravitational influence of two asteroids, treated as arbitrary mass distributions. This builds on the more traditional circular restricted three body problem (CR3BP) by eliminating the assumption that the two larger bodies are point masses behaving under Keplerian dynamics. The dynamics of the two asteroids must instead be modeled with the F2BP. Because of the computational burden of the mutual gravity potential in the F2BP, past RF3BP studies have simplified the binary system geometry to allow for more general analysis. Work by Scheeres and Bellerose simplified the RF3BP to a planar ellipsoid-sphere system and was able to identify zero-velocity to curves of the system in order to characterize the motion of a massless spacecraft [47]. Using a similar model, Dell’Elce et al. were able to characterize the stability of trajectories about asymmetric binary systems. Specifically,

they identifying terminator orbits beyond the secondary and retrograde orbits between the primary and secondary as the only long term stable orbits in the system [48]. Work by Chappaz and Howell expanded on this analysis by implementing a two ellipsoid binary model to explore bounded periodic motion of spacecraft in binary systems [49]. Recently work by Feng and Hou was able to generalize CR3BP libration point orbits into a second-order two ellipsoid system [50]. In this analysis we build on our remote estimation analysis to develop consider covariance analysis tools for the RF3BP.

1.5 Contributions

The following journal, conference, and software contributions resulted from the work presented in this thesis.

1.5.1 Journal Papers

- A.B. Davis, D.J. Scheeres, “A Covariance Study for Gravity Estimation of Binary Asteroids,” *Journal of Guidance, Control, and Dynamics* [In Prep.]
- A.B. Davis, D.J. Scheeres, “High Fidelity Modeling of Rotationally Fissioned Asteroids,” *The Planetary Science Journal* [In Revisions]
- A.B. Davis, D.J. Scheeres, “Doubly Synchronous Binary Asteroid Mass Parameter Observability,” *Icarus*, Vol. 341 (2020), <https://doi.org/10.1016/j.icarus.2019.113439>
- D.J. Scheeres, A.S. French, ... A.B. Davis, ... D.S. Lauretta, “Heterogenous mass distribution of the rubble-pile asteroid (101955) Bennu”, *Science* [Submitted]
- S.R. Chesley, A.S. French, A.B. Davis, ... D.S. Lauretta, “Trajectory estimation for particles observed in the vicinity of (101955) Bennu” *JGR: Planets* [Submitted]
- D. S. Lauretta, C.W. Hergenrother, S.R. Chesley, ... A.B. Davis ... C.A. Bennet, “Episodes of particle ejection from the surface of the active asteroid (101955) Bennu” *Science* 2019

- H.F. Agrusa, D.C. Richardson, A.B. Davis, et al., “A Simulation Benchmarking and Sensitivity Study of the Full Two-Body Gravitational Dynamics of the DART Mission Target, Binary Asteroid 65803 Didymos”, *Icarus* [Accepted]
- M. Hirabayashi, S.R. Schwartz, Y. Yu, A.B. Davis, ... A. F. Cheng, “Assessing possible mutual orbit period change by shape deformation of Didymos after a kinetic impact in the NASA-led Double Asteroid Redirection Test,” *ASR* 2019
- M. Hirabayashi, A.B. Davis ..., S.P. Naidu, “Constraints on the perturbed mutual motion in Didymos due to impact-induced deformation of its primary after the DART impact,” *MNRAS* 2017
- C. M. Elder, A. M. Bramson, L. W. Blum, ... A. B. Davis, ... K. L. Mitchell, “OCEANUS: A high science return Uranus orbiter with a low-cost instrument suite,” *Acta Astronautica* 2018

1.5.2 Conference Papers, Talks, and Posters

- A.B. Davis, D.J. Scheeres. “High-Fidelity Dynamics of Post-Fission Asteroid Evolution,” talk accepted at 51st Lunar and Planetary Science Conference, The Woodlands, Texas, Cancelled 2020
- A.B. Davis, D.J. Scheeres. “A Covariance Study for Gravity Estimation of Binary Asteroids,” talk and paper presented at 2020 AAS Guidance, Navigation and Control Conference, Breckenridge, Colorado, February 2020
- A.B. Davis, D.J. Scheeres. “Sensitivity of Trajectories to Mass Parameters in the Restricted Full ThreeBody Problem,” talk and paper presented at 27th AAS/AIAA Astrodynamics Specialist Meeting, Portland, Maine, August 2019
- A.B. Davis, D.J. Scheeres. “High-Fidelity Testing of Binary Asteroid Formation with Applications to 1999 KW4,” talk presented at 50th AAS/Division of Dynamical Astronomy

Meeting, Boulder, Colorado, June 2019

- A.B. Davis, D.J. Scheeres. “Applications of Inertia Integrals to Dynamical Modelling of the Double Asteroid Redirection Test (DART) target (65803) Didymos,” eLightning presentation at AGU Fall Meeting, Washington D.C., December 2018
- A.B. Davis, D.J. Scheeres. “Dynamical Applications of the Full Two-Body Problem,” poster presentation at 50th AAS/Division of Planetary Sciences Meeting, Knoxville, Tennessee, October 2018
- A.B. Davis, D.J. Scheeres. “Full two-body problem mass parameter observability explored through doubly synchronous systems,” talk presented at 49th AAS/Division of Dynamical Astronomy Meeting, San Jose, California, April 2018
- A.B. Davis, D.J. Scheeres. “Mass Parameter Estimation of Doubly Synchronous Binary Asteroid Systems Through Visual Observation,” poster presented at 49th Lunar and Planetary Science Conference, The Woodlands, Texas, March 2018
- M., Hirabayashi, A.B. Davis, et al. “NASA’s DART Mission to Didymos: The Effect of Shape Deformation of the Primary and Ellipticity of the Secondary on Post-Impact Orbital Period,” poster presented at 49th Lunar and Planetary Science Conference, The Woodlands, Texas, March 2018
- A.B. Davis, D.J. Scheeres. “Estimating Mass Parameters of Doubly Synchronous Binary Asteroids,” talk presented at 49th AAS/Division of Planetary Sciences Meeting, Provo, Utah, October 2017
- M., Hirabayashi, S.A. Jacobson, A.B. Davis. “Binary asteroid orbit evolution due to primary shape deformation,” poster presented at 49th AAS/Division of Planetary Sciences Meeting, Provo, Utah, October 2017

- A.B. Davis, D.J. Scheeres. “High Fidelity Modeling of Mass Distribution Perturbations of the Didymos System,” AIDA 3rd International Workshop, Laurel, Maryland, June 2017
- A.B. Davis, D.J. Scheeres. “Constraining Binary Asteroid Mass Distributions Based On Mutual Motion,” talk presented at 48th AAS/Division of Dynamical Astronomy Meeting, London, UK, June 2017
- A.B. Davis, D.J. Scheeres. “Binary Asteroid Orbit Sensitivity to Gravity Field Coefficients: Applications to the AIDA Mission Target 65803 Didymos,” poster presented at 48th Lunar and Planetary Science Conference, The Woodlands, Texas, March 2017
- A.B. Davis, D.J. Scheeres. “Dynamics and Modeling of a Binary Asteroid System with Applications to 65803 Didymos,” talk and paper presented at 27th AAS/AIAA Space Flight Mechanics Meeting, San Antonio, Texas, February 2017

1.5.3 Software

- A.B. Davis. “General Use Binary Asteroid Simulator,” August 2019, <https://github.com/alex-b-davis/gubas>

1.6 Thesis Organization

This thesis begins by reviewing the development of the inertia integral implementation of the F2BP and benchmarking between different F2BP models. The discussion defines the mutual gravity potential and introduces the inertia integrals. Building on the mutual gravity potential, the associated gravity accelerations and torques are developed for use in the equations of motion. From here, the equations of motion for all 9 degrees of freedom are developed to appropriately capture the dynamical coupling present in binary systems. Finally, we detail a verification and benchmarking campaign from the DART mission which tests the numerical accuracy and computational efficiency of various F2BP implementations.

Chapter 3 further studies the dynamics of the F2BP by identifying the equilibria in the system and studying the dynamic structure in their vicinity. The conditions for the equilibria are first developed for arbitrary F2BP systems and then split into the outer stable equilibrium and inner unstable equilibrium. While the outer equilibrium can be found in nature and is an important end state for binary evolution, the inner equilibrium acts as a barrier to fission during binary asteroid formation at the second order. In trying to understand the behavior of binaries at or near the outer equilibrium we identify the dynamical manifolds of the system. They are first developed for the planar implementation of the F2BP and then expanded to the nonplanar problem. This analysis is later used to study the remote estimation of binary mass parameters. We then study the structure about the inner unstable equilibrium. While past analysis of the planar and second order F2BP identified this equilibrium as a barrier between recollision and successful fission, we find that this structure breaks down once the dynamics are expanded to a fourth order, nonplanar implementation.

In Chapter 4 we build on the breakdown of the inner equilibrium as a barrier to recollision to study its broader impacts on binary formation and evolution. This study largely follows the analysis in Jacobson and Scheeres 2011 which used planar second order dynamics, whereas we apply nonplanar fourth order dynamics to understand the impact of the change in the dynamical structure under these improved dynamics. We perform a set of Monte Carlo simulations following three representative binaries from the moment of fission for a year of integrated time. The binaries studied are Moshup (1999 KW4), a low mass ratio binary, 1996 HW1, a high mass ratio and contact binary, and 2000 DP107, a low mass ratio binary with an equatorial crater. The statistical breakdown and details of the binary fates for all three systems are analyzed and contrasted with the Jacobson and Scheeres results amongst others. While most results show good agreement with past analysis, we identify the new possibility of recollision as well as identifying differing effects of secondary fission models. In addition our study of DP107 identifies the challenges of forming an equatorial crater from binary fission as theorized by Tardivel et al.[41].

To understand the remote estimation of binary mass parameters, Chapter 5 builds on the

dynamical structure of the outer equilibrium to understand its sensitivity to the mass parameters. The chapter begins by returning to the planar problem and performing a sensitivity analysis of the fundamental frequencies to various mass parameters in the system. Then a more rigorous analytical approach is used to derive the partials of these frequencies to the mass parameters. These partials are used to develop a gradient descent method of estimating binary mass parameters from measurements of the fundamental frequencies. While this approach is under-constrained for the planar problem, it can be expanded to the nonplanar problem where it is well conditioned. The approach is applied to 617 Patroclus as an example study and then to a more broad scaling of ellipsoidal shapes. Due to singularities for this approach with spherical binaries, we develop a modified approach for near-spherical systems and apply it to the Pluto-Charon system. While these studies show implementation difficulties for each estimation approach, it does prove the mathematical feasibility of such an approach.

Finally, Chapter 6 develops an implementation of the RF3BP and consider covariance analysis to understand the sensitivity of an in-situ spacecraft to binary asteroid mass parameters. The RF3BP implementation expands on the inertia integral F2BP by adding a point mass spacecraft. The partial matrices for the spacecraft dynamics and sensitivity to the binary mass parameters are then derived for use in a consider covariance analysis. The consider covariance analysis uses a standard CKF and simplified DSN and relative navigation measurement models. The analysis is applied to the DART and Hera target Didymos. The sensitivity of the spacecraft to the masses, inertias, and higher order mass parameters of each asteroid is found to be generally significant enough for effective estimation of these parameters. The effect of model and estimation errors on the analysis are also examined and found to primarily impact the mass and inertia estimation. The effect of excited binary dynamics are also studied and found to generally provide better estimates due to the more observable dynamics.

Chapter 2

Dynamics of the Full Two-Body Problem

In this chapter we detail the mathematical models used to simulate the Full Two-Body Problem and describe validation and benchmarking efforts for our implementation. To begin we define the assumptions and framework of the F2BP. Next the inertia integral mutual gravity potential is introduced along with the development of associated gravity accelerations and torques. Leveraging these, the generalized equations of motion are derived. Given this implementation, a broad campaign of verification and benchmarking between a variety of F2BP simulations is detailed. The accuracy and computational efficiency of the inertia integral method is compared against other methods under the framework of the DART mission. The benchmarking effort concludes that the inertia integral method provides equal or greater accuracy than other methods, while requiring orders of magnitude less computational time.

2.1 The Full Two-Body Problem

Binary asteroids represent a dynamically complex system which challenges many of the standard assumptions made in orbital mechanics. To accurately model these systems the gravitational effect of each body's irregular mass distribution must be tracked. This results in a coupled system wherein the relative position of the bodies as well as their individual attitudes are interlinked. This nine degree of freedom system is commonly referred to as the Full Two-Body Problem (F2BP). In this work we focus on the most general form of the F2BP, making only the assumption that the asteroids are rigid bodies of arbitrary mass distribution. This realization of the F2BP, Fig. 2.1,

treats the primary asteroid, A , and secondary asteroid, B , as collections of infinitesimal mass elements, dm_1 and dm_2 , each with density ρ and ρ' respectively. Each body has a principally aligned, body-fixed frame, \hat{x} and \hat{x}' respectively, defined relative to some inertial frame \hat{n}

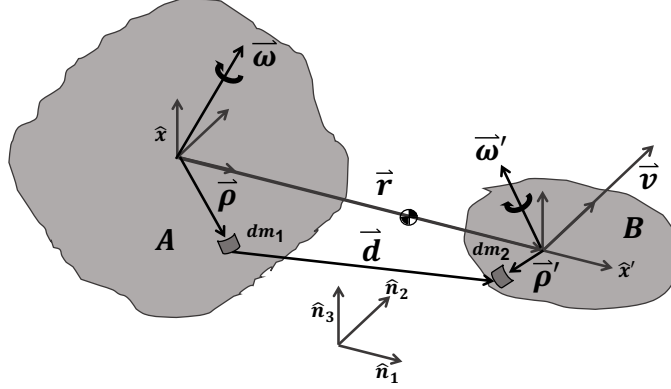


Figure 2.1: System diagram of the Full Two- Body Problem.

From the system diagram one can infer that a concentration of mass on some part of the primary could lead to both gravitational acceleration of the secondary off of the relative separation line, \vec{r} , and create a gravitational torque on the secondary. Through this interplay the coupled dynamics of the F2BP become apparent. To fully capture the gamut of gravitational effects within the system we develop the mutual gravity potential as a function of the relative position and attitude of the bodies.

2.1.1 The Mutual Gravity Potential

Within the F2BP the mutual gravity potential must account for the full effect of each body's irregular mass distribution. As such its derivation begins from the double integral over all mass elements making up both bodies

$$U = -G \int_A \int_B \frac{1}{d} dm_A dm_B \quad (2.1)$$

where G is the gravity constant and d represents the distance between pairs of mass elements. Unlike the standard point mass gravity formulation, the mutual gravity potential cannot be analytically reduced further without mathematical approximations. In this work we follow the method of deriving the mutual gravity potential presented by Hou et al. 2016[28]. The approach reformulates the mutual gravity potential as a recursive binomial expansion in combination with a Legendre polynomial expansion up to some truncation order N . In this form, the mutual gravity potential consists of an outer summation

$$U = -G \sum_{n=0}^N \frac{1}{R^{n+1}} \tilde{U}_n \quad (2.2)$$

which gathers the contribution of each order of the expansion over the mass distribution. The inner summation term, \tilde{U}_n , is then

$$\begin{aligned} \tilde{U}_n = \sum_{k(2)=n}^0 t_k^n & \sum_{(i_1, i_2, i_3)(i_4, i_5, i_6)(j_1, j_2, j_3)(j_4, j_5, j_6)} a_{(i_1, i_2, i_3)(i_4, i_5, i_6)}^k b_{(j_1, j_2, j_3)(j_4, j_5, j_6)}^{n-k} \\ & e_x^{i_1+i_4} e_y^{i_2+i_5} e_z^{i_3+i_6} M_A T_A^{(i_1+j_1), (i_2+j_2), (i_3+j_3)} \\ & M_B T_B'^{(i_4+j_4), (i_5+j_5), (i_6+j_6)} \end{aligned} \quad (2.3)$$

Where $k(2)$ implies stepping by 2 as opposed to 1

Where the terms e_i are the components of the relative position unit vector, M_A and M_B are each body's mass, and T_A and T_B' are the sets of inertia integrals representing each body's mass distribution. The inertia integrals are derived as the Legendre coefficients for the expansion. The prime in T_B' denotes the rotation of these terms into the primary's body fixed frame. The term t_k represents the recursive expansion coefficient which go as

$$t_{k+2}^n = -\frac{(n-k)(n+k+1)}{(k+2)(k+1)} \quad (2.4)$$

while a and b are the binomial expansion coefficients whose equations are

$$\begin{aligned} a_{(i_1, i_2, i_3)(i_4, i_5, i_6)}^k &= a_{(i_1-1, i_2, i_3)(i_4, i_5, i_6)}^{k-1} + a_{(i_1, i_2-1, i_3)(i_4, i_5, i_6)}^{k-1} + a_{(i_1, i_2, i_3-1)(i_4, i_5, i_6)}^{k-1} \\ &- a_{(i_1, i_2, i_3)(i_4-1, i_5, i_6)}^{k-1} - a_{(i_1, i_2, i_3)(i_4, i_5-1, i_6)}^{k-1} - a_{(i_1, i_2, i_3)(i_4, i_5, i_6-1)}^{k-1} \end{aligned} \quad (2.5)$$

$$\begin{aligned}
b_{(j_1, j_2, j_3)(j_4, j_5, j_6)}^k &= b_{(j_1-2, j_2, j_3)(j_4, j_5, j_6)}^{k-2} + b_{(j_1, j_2-2, j_3)(j_4, j_5, j_6)}^{k-2} + b_{(j_1, j_2, j_3-2)(j_4, j_5, j_6)}^{k-2} \\
&+ b_{(j_1, j_2, j_3)(j_4-2, j_5, j_6)}^{k-2} + b_{(j_1, j_2, j_3)(j_4, j_5-2, j_6)}^{k-2} + b_{(j_1, j_2, j_3)(j_4, j_5, j_6-2)}^{k-2} - 2b_{(j_1-1, j_2, j_3)(j_4-1, j_5, j_6)}^{k-2} \\
&- 2b_{(j_1, j_2-1, j_3)(j_4, j_5-1, j_6)}^{k-2} - 2b_{(j_1, j_2, j_3-1)(j_4, j_5, j_6-1)}^{k-2}
\end{aligned} \tag{2.6}$$

Whose indices are defined as

$$k = i_1 + i_2 + i_3 + i_4 + i_5 + i_6 \tag{2.7}$$

$$n - k = j_1 + j_2 + j_3 + j_4 + j_5 + j_6 \tag{2.8}$$

2.1.2 Inertia Integrals

Central to this reformulation of the mutual potential is the use of inertia integrals to describe the mass distribution. As previously stated the inertia integrals are derived as the Legendre polynomial expansion coefficients. The general form of the inertia integrals is

$$T^{l,m,n} = \frac{1}{MR^{l+m+n}} \int_B x^l y^m z^n dm, \text{ where } l + m + n = N \tag{2.9}$$

where the l , m , and n are the Cartesian degree for a term evaluated at some expansion order N . In this way the inertia integrals can be considered analogous in use to spherical harmonics[25]. The mathematical form of the inertia integrals, however is more similar to that of the moments and products of inertia for a rigid body wherein each term represents the mass distribution about some axis. As such the inertia integrals represent arbitrary order N form of the moments of inertia. At the second order the inertia integrals can describe the moments of inertia as a linear combination. Here we provide the mass and length normalized form of an inertia integral along with the 0th and

2nd order coefficients in terms of the normalized moments and product of inertia.

$$T^{l,m,n} = \frac{1}{MR^{l+m+n}} \int_B x^l y^m z^n dm, \text{ where } l + m + n = N \quad (2.10)$$

$$1 = T^{0,0,0} \quad (2.11)$$

$$I_{xx} = T^{0,2,0} + T^{0,0,2} \quad (2.12)$$

$$I_{yy} = T^{2,0,0} + T^{0,0,2} \quad (2.13)$$

$$I_{zz} = T^{2,0,0} + T^{0,2,0} \quad (2.14)$$

$$I_{xy} = -T^{1,1,0} \quad (2.15)$$

$$I_{xz} = -T^{1,0,1} \quad (2.16)$$

$$I_{yz} = -T^{0,1,1} \quad (2.17)$$

It is of note that the 0th order inertia integral is equal to the mass for the non-normalized form, thus it is equal to one in the normalized form.

2.1.3 Gravity Accelerations and Torques

Building upon the mutual gravity potential, the expressions for the gravity accelerations and torques are generated. Both terms are partials of the mutual gravity potential with respect to either the relative separation or relative attitude. The equation of the gravity acceleration follows the standard approach as a the partial of the gravity potential with respect to the relative separation. Thus the gravity acceleration can be computed for the i th Cartesian direction component as

$$\frac{\partial U}{\partial r_i} = -G \sum_{n=0}^N \left(\frac{1}{R^{n+1}} \frac{\partial \tilde{U}_n}{\partial r_i} - \frac{(n+1)r_i}{R^{n+1}} \frac{\partial \tilde{U}_n}{\partial r_i} \right) \quad (2.18)$$

where $\frac{\partial \tilde{U}_n}{\partial r_i}$ is

$$\begin{aligned} \frac{\partial \tilde{U}_n}{\partial r_i} = & \sum_{k(2)=n}^0 t_k^n \sum_{(i_1, i_2, i_3)(i_4, i_5, i_6)(j_1, j_2, j_3)(j_4, j_5, j_6)} a_{(i_1, i_2, i_3)(i_4, i_5, i_6)}^k b_{(j_1, j_2, j_3)(j_4, j_5, j_6)}^{n-k} \\ & \left[(i_1 + i_4) e_y^{i_2+i_5} e_z^{i_3+i_6} \frac{\partial e_x^{i_1+i_4-1}}{\partial r_i} + (i_2 + i_5) e_x^{i_1+i_4} e_z^{i_3+i_6} \frac{\partial e_y^{i_2+i_5-1}}{\partial r_i} + (i_3 + i_6) e_x^{i_1+i_4} e_y^{i_2+i_5} \frac{\partial e_z^{i_3+i_6-1}}{\partial r_i} \right] \\ & M_A T_A^{(i_1+j_1), (i_2+j_2), (i_3+j_3)} M_B T_B'^{(i_4+j_4), (i_5+j_5), (i_6+j_6)} \end{aligned} \quad (2.19)$$

Where $k(2)$ implies stepping by 2 as opposed to 1

The derivation of the gravity torques, as originally described in Maciejewski 1995, follows a more roundabout path[20]. To begin, the total angular momentum is computed as

$$\vec{M}_A + \vec{M}'_B = \vec{r} \times \frac{\partial U}{\partial \vec{r}} \quad (2.20)$$

where \vec{M}_i is the torque on experienced by body i due to the gravity of the opposing body. The $'$ in \vec{M}'_B denotes that it has been rotated from the secondary's body fixed frame into that of the primary. \vec{M}'_B is then computed as

$$\vec{M}'_B = -\vec{\alpha} \times \frac{\partial U}{\partial \vec{\alpha}} - \vec{\beta} \times \frac{\partial U}{\partial \vec{\beta}} - \vec{\gamma} \times \frac{\partial U}{\partial \vec{\gamma}} \quad (2.21)$$

Where the $\vec{\alpha}$, $\vec{\beta}$, and $\vec{\gamma}$ are columns of the rotation matrix

$$\mathbf{C}_{B/A} = \begin{bmatrix} \vec{\alpha} & \vec{\beta} & \vec{\gamma} \end{bmatrix} \quad (2.22)$$

which maps from the secondary's body fixed frame into the primary's body-fixed frame. The torque on the primary is thus

$$\vec{M}_A = \vec{r} \times \frac{\partial U}{\partial \vec{r}} - \vec{M}'_B \quad (2.23)$$

Each partial of the potential with respect to the columns of the rotation matrix, i.e. $\frac{\partial U}{\partial \vec{\alpha}}$, is then a vector of partials of the potential with respect to the elements of the rotation matrix, \mathbf{C}_{ij} . This partial of the mutual gravity potential is trivially computed as

$$\frac{\partial U}{\partial \mathbf{C}_{ij}} = -G \sum_{n=0}^N \frac{1}{R^{n+1}} \frac{\partial \tilde{U}_n}{\partial \mathbf{C}_{ij}} \quad (2.24)$$

Where $\frac{\partial \tilde{U}_n}{\partial \mathcal{C}_{ij}}$ is

$$\frac{\partial \tilde{U}_n}{\partial \mathcal{C}_{ij}} = \sum_{k(2)=n}^0 t_k^n \sum_{(i_1, i_2, i_3)(i_4, i_5, i_6)(j_1, j_2, j_3)(j_4, j_5, j_6)} a_{(i_1, i_2, i_3)(i_4, i_5, i_6)}^k b_{(j_1, j_2, j_3)(j_4, j_5, j_6)}^{n-k} \quad (2.25)$$

$$e_x^{i_1+i_4} e_y^{i_2+i_5} e_z^{i_3+i_6} M_A T_A^{(i_1+j_1), (i_2+j_2), (i_3+j_3)}$$

$$M_B \frac{\partial T_B^{(i_4+j_4), (i_5+j_5), (i_6+j_6)}}{\partial \mathcal{C}_{ij}}$$

Where k(2) implies stepping by 2 as opposed to 1

Where $\frac{\partial T_B^{(i_4+j_4), (i_5+j_5), (i_6+j_6)}}{\partial \mathcal{C}_{ij}}$ is computed as the partial of the equation for inertia integral rotation as described in Hou et al. 2016[28].

2.1.4 Equations of Motion

Given the the mutual gravity potential and its partials, the equations of motion (EOMs) for the F2BP can be generated. The inertial form of the F2BP has 12 degrees of freedom, however, using the relative dynamics it can be reduced to 9 degrees of freedom[20].

$$\vec{X} = \left[\vec{r} \quad \vec{\theta}_1 \quad \vec{\theta}_2 \quad \dot{\vec{r}} \quad \vec{\omega}_1 \quad \vec{\omega}_2 \right]^T \quad (2.26)$$

where \vec{r} is the relative separation vector measured from the primary to secondary, the vectors $\vec{\theta}_1$ and $\vec{\theta}_2$ are Euler 123 angle sets defining the inertial orientation of the primary and the orientation of the secondary relative to the primary, the vectors $\vec{\omega}_1$ and $\vec{\omega}_2$ are the angular velocities. We select the Euler angles as the attitude state because of their intuitive structure, but any attitude representation could be used instead. The angular velocities correspond to the Euler angles such that

$$\dot{\vec{\theta}}_i = \mathbf{B}_i \vec{\omega}_i \quad (2.27)$$

$$\mathbf{B}_i = \frac{1}{\cos \theta_{i,2}} \begin{bmatrix} \cos \theta_{i,3} & -\sin \theta_{i,3} & 0 \\ \cos \theta_{i,2} \sin \theta_{i,3} & \cos \theta_{i,2} \cos \theta_{i,3} & 0 \\ -\sin \theta_{i,2} \cos \theta_{i,3} & \sin \theta_{i,2} \sin \theta_{i,3} & \cos \theta_{i,2} \end{bmatrix} \quad (2.28)$$

The rotation matrix corresponding to the Euler angle sets are

$$\mathbf{C}_i = \mathbf{C}(\vec{\theta}_i) \quad (2.29)$$

where the Euler angle set is the Euler 123 body set.

Following the implementation of Maciejewski, the F2BP EOMs can be derived from Newton's second law and Euler's EOMs as [20].

$$\ddot{\vec{r}} = -\left(\mathbf{I}_A^{-1}\left(\left(\mathbf{I}_A \vec{\omega}_1\right) \times \vec{\omega}_1 + \vec{M}_A\right)\right) \times \vec{r} - 2\tilde{\omega}_1 \dot{\vec{r}} - \tilde{\omega}_1 \tilde{\omega}_1 \vec{r} - \frac{1}{m} \frac{\partial U}{\partial \vec{r}} \quad (2.30)$$

$$\dot{\vec{\omega}}_1 = \mathbf{I}_A^{-1}\left(\left(\mathbf{I}_A \vec{\omega}_1\right) \times \vec{\omega}_1 + \vec{M}_A\right) \quad (2.31)$$

$$\begin{aligned} \dot{\vec{\omega}}_2 = & \mathbf{C}_{B/A} \mathbf{I}_B^{-1} \mathbf{C}_{B/A}^T \left(\left(\mathbf{C}_{B/A} \mathbf{I}_B \mathbf{C}_{B/A}^T (\vec{\omega}_1 + \vec{\omega}_2)\right) \times \vec{\omega}_1 + \vec{M}_B\right) \\ & - \left(\dot{\mathbf{C}}_{B/A} \mathbf{I}_B \mathbf{C}_{B/A}^T + \mathbf{C}_{B/A} \mathbf{I}_B \dot{\mathbf{C}}_{B/A}\right) \\ & \cdot (\vec{\omega}_1 + \vec{\omega}_2) - \mathbf{I}_A^{-1}\left(\left(\mathbf{I}_A \vec{\omega}_1\right) \times \vec{\omega}_1 + \vec{M}_A\right) \end{aligned} \quad (2.32)$$

Where the $(\tilde{})$ operator describes the skew-symmetric matrix transform on a vector in \mathbb{R}^3 .

\mathbf{I}_i denotes the inertia tensor of body i as represented in the primary's body fixed frame.

$$\tilde{f} = \begin{bmatrix} 0 & -f_3 & f_2 \\ f_3 & 0 & -f_1 \\ -f_2 & f_1 & 0 \end{bmatrix} \quad (2.33)$$

2.2 Model Verification and Benchmarking

This particular implementation of the F2BP was selected for its relative simplicity, accuracy and computational speed. The historic challenge in simulating binary asteroid dynamics, or the F2BP, has been the computational burden of the mutual gravity potential between two arbitrary and asymmetric mass distributions. In order to verify the improvements gained from the Hou, or inertia integral, method a broad benchmarking effort was necessary. There are two parameters with which to compare mutual gravity potential representations: accuracy of solutions and computational

efficiency. All benchmarking efforts described here were performed as a part of the DART mission and were thus performed for 65803 Didymos, the mission target [51]. Other current F2BP simulation methods attempt to reformulate the F2BP and reduce the computational burden imposed in two ways. Packed spheres methods decouples the orientation of the bodies from the mutual gravity potential and allows for an exact solution by discretizing each body as a collection of spherical masses while sacrificing the accuracy with which the mass distributions can be captured. The polyhedral expansion method instead focuses on capturing the mass distributions very accurately, but is unable to decouple the attitude and mass distribution. This means that the mass distributions must be reevaluated at each time step to account for changes in the relative orientation of the bodies [24]. The inertia integral method however is able to accurately capture the mass distribution while also decoupling the attitude and mass distribution in the mutual potential evaluation. This results in significant improvements to the computational efficiency of F2BP simulations. In addition, the inertia integrals are not tied directly to shape or density distribution, and can thus be used to approximate the mass distributions absent a shape model or other knowledge of composition. In comparison to the polyhedral expansion method, the inertia integral approach can be shown to give numerically identical results for the mutual gravity potential at each expansion order and inertia integral based simulations can be run in small fractions of the wall-time compared to the polyhedral expansion and packed sphere methods.

2.2.1 Dynamical Accuracy Benchmarking

In comparing the accuracy of solutions, two approaches can be considered; the first being a direct comparison of the mutual gravity potential evaluated at an arbitrary state and the second being a comparison of integration results over some time period. We first compare the mutual gravity potential at the same arbitrary state evaluated by the inertia integral and polyhedral expansion methods. The packed spheres method is not included because its spherical discretization of the mass distributions prevents an exact match with the inertia integral or polyhedral mass distributions. To compare between the inertia integral method and polyhedral method, four realizations

of the Didymos system were evaluated with each body axially aligned and the nominal separation value of 1.18 km. These realizations are a two cube system, a two sphere system, a two ellipsoid system, and polyhedral Didymos primary and ellipsoidal secondary. In all cases the primary and secondary shapes are scaled by volume to match the current the estimated mass of each body, assuming the constant density. We compare the total mutual gravity potential truncated at orders 2-7 for each of the four system realizations and see agreement down to numerical noise, Table 2.1.

Table 2.1: Fractional error in mutual gravity potential evaluated by the polyhedral expansion method and inertia integral method for orders 2-7.

Order	Cube - Cube	Sphere - Sphere	Ellipsoid - Ellipsoid	Polyhedron - Ellipsoid
2	-2.50E-15	-3.54E-15	-1.25E-15	-3.11E-15
3	-2.50E-15	4.16E-16	-1.66E-15	5.40E-15
4	2.29E-15	1.46E-15	5.40E-15	1.66E-15
5	2.29E-15	0.0	-8.30E-16	2.08E-15
6	-3.12E-15	-1.46E-15	-2.08E-15	-8.30E-16
7	-3.12E-15	1.66E-15	1.45E-15	2.08E-16

It is worth pointing out that cube case shows identical fractional error for every two orders; this is a result of the cube being exactly representable via a polyhedral discretization with odd orders of the inertia integrals for an ideal cube going to zero due to symmetry. Continuing from this, if the sphere and ellipse cases were generated from the ideal shapes, as opposed to the polyhedral discretization necessary for comparison, their mutual gravity potential's would show the same behavior.

Following the direct benchmarking of the mutual gravity potentials, we compare a 150 day integration of the polyhedron-ellipsoid model for the JPL polyhedral expansion implementation and the inertia integral implementation, Fig. 2.2. Both integrations are performed using the Lie group variational integrator (LGVI) with a 40 second time step and a 4th order mutual gravity truncation. The LGVI is a symplectic integrator which constrains the attitude solution to the Lie group, thus preserving both the Hamiltonian and rotational accuracy. We compare the relative position, linear momentum, primary and secondary angular momenta, and the attitude matrices for the inertial and relative orientations[52]. For each comparison we plot the value of the states

from each integration as well as the fractional error between the two integrations. The position and momenta fractional errors are computed as $\frac{|\vec{v}_1| - |\vec{v}_2|}{|\vec{v}_1|}$. For the orientation the fractional error is computed as $\|I_{3 \times 3} - C_1^T C_2\|$. While these parameters do not account for component errors between the two models states, it provides a clear comparison; the detailed comparison of each model including directional errors can be found in Agrusa et al. 2020[53]. The results over the integration show good agreement between the two implementations. Though errors do clearly grow over time this is likely due to numerical precision differences in the method by which the initial conditions and system parameters are loaded into each implementation as well as difference caused by the unit normalization of the dynamics between the two implementation.

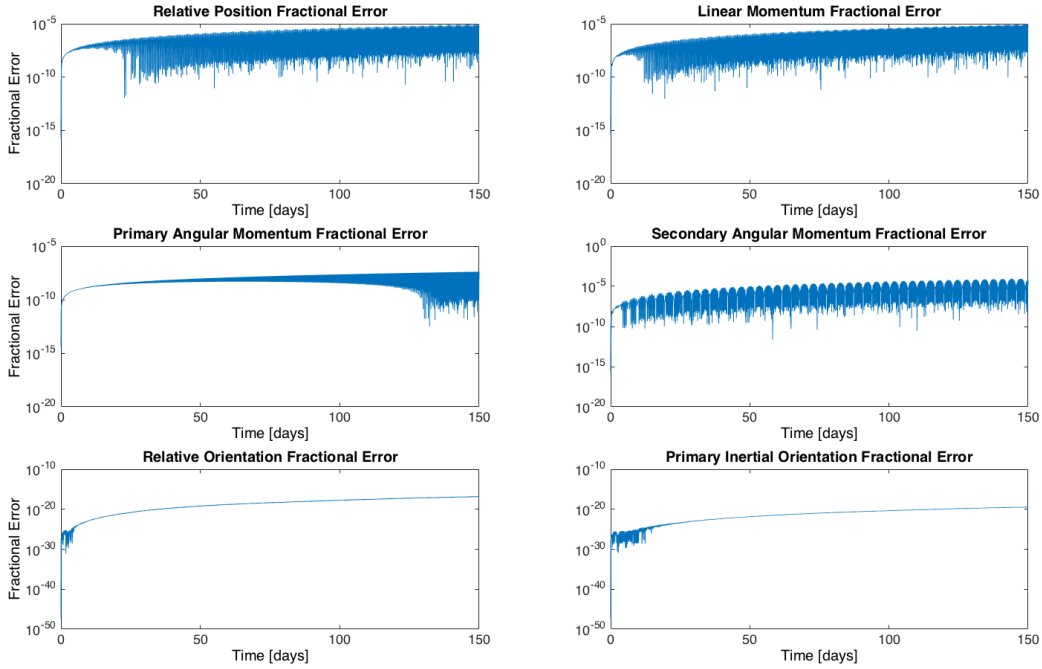


Figure 2.2: Fractional error between JPL polyhedral expansion and UCB inertia integral numerical integrations using identical LGVI integrators.

2.2.2 Simulation Runtime Benchmarking

In comparing the simulation runtimes we must account for computational and integration implementations because we do not have each mutual gravity potential method implemented in the same environment. To compare runtimes, we use the same four realizations of Didymos as the previous analysis. Four F2BP implementations are compared: the inertia integral method, the polyhedral expansion methods implemented at JPL and GSFC, and the packed spheres method implemented at Univeristy of Maryland (UMD). Both of the polyhedral expansion implementations and the inertia integral implementation use the LGVI with a 40 second integration step which requires only one mutual gravity evaluation per integration step. The UMD packed spheres implementation uses a leapfrog symplectic integration technique with a 1.875 second and 15 second integration step, but has not specified the number of mutual gravity evaluations needed for each integration step. In comparing the runtimes of each case we normalize by the number of processors used and the simulation duration, $\frac{n_{processors}}{T_{duration}}$. The normalized runtimes for each implementation and Didymos realization for a simulation duration of 365 days are provided in Table 2.2. The expansion order of the mutual gravity potential used for a given simulation is provided in parentheses in the table. It should be noted that while the packed spheres method provides an exact solution

Table 2.2: Normalized runtimes for a variety of mutual gravity potential methods integrating the Didymos system for 365 days.

Method	Integration	Cube - Cube	Sphere - Sphere	Ellipsoid - Ellipsoid	Polyhedron - Ellipsoid
Inertia Integrals	LGVI, dt=40 sec	0.032 (N=4)	0.032 (N=4)	0.032 (N=4)	0.032 (N=4)
JPL Polyhedral Expansion	LGVI, dt=40 sec	0.017 (N=4)	3.351 (N=3)	3.351 (N=3)	12.104 (N=3)
GSFC Polyhedral Expansion	LGVI, dt=40 sec	0.081 (N=3)	5.446 (N=3)	5.446 (N=3)	20.288 (N=3)
UMD Packed Spheres	Leapfrog, dt=1.875 sec	NA	NA	NA	4.395 (Exact)
UMD Packed Spheres	Leapfrog, dt=15 sec	NA	NA	NA	0.592 (Exact)

to the mutual gravity potential, denoted in the table as (Exact), it contains discretization error due to its approximation of the bodies as collections of spheres. The results in the table show the inertia integral method to be significantly faster than both methods in all but the simple cube

case having two 12 facet shape models. In the cube-cube system, we see that the JPL polyhedral expansion is faster than other methods, this is because a cube is expressible as only 12 tetrahedra; ideal for the polyhedral expansion method which is optimized to evaluate large numbers of tetrahedron for each mutual gravity evaluation and this reduces in number of computations from hundreds or thousands to tens. It should also be pointed out that the results in the table do not compare the accuracy between the simulations, this analysis can be found in Agrusa et al. 2020[53]. The previous comparison of the accuracy of the inertia integral method relative to the polyhedral expansion method shows that the two methods used in similar integration environments achieve similar levels of simulation accuracy. The version of the GSFC polyhedral method tested is fixed to order 3, while the JPL polyhedral method and inertia integral methods are implemented to expand to arbitrary orders. The polyhedral method run beyond orders 3 and 4 can be prohibitively slow; this is why the JPL polyhedral expansion method is reduced to order 3 for the high facet count models used in the sphere, ellipsoid and polyhedron cases in Table 2.2. If orders beyond 3 and 4 are determined to be necessary to reach the mission requirements and simulation accuracy this severely limits the polyhedral expansion method. For the inertia integral method higher orders would result in an increased runtime, but the effect is much less significant because the inertia integrals are pre-computed, taking fractions of a second through fourth order and less than a minute at higher orders. If an analysis would require the integration time step to be smaller than the 40 second time step used by both polyhedral expansion implementations, this would represent a corresponding, and possibly prohibitive, factor of growth in the polyhedral method run times.

2.3 Summary

In this chapter we provide the details of the inertia integral formulation of the F2BP. The associated mutual gravity potential is provided and its associated gravity accelerations and torques are derived. The details of the inertia integrals and their relationship to other mass parameter realizations is described. The F2BP EOMs, which enable the research presented herein, are then detailed. We finally provide F2BP benchmarking analysis which shows the inertia integral im-

plementation to have superior computational efficiency than other F2BP implementations while maintaining numerical accuracy.

Chapter 3

The Equilibria and Dynamical Structure of the Full Two-Body Problem

In this chapter we identify the two equilibria in the F2BP and explore the dynamical structure about them. From the structure about the equilibria we are able to identify generalized behaviors of the system which have impacts on binary formation and mass parameter estimation. Initially the general constraints for equilibria in the F2BP are derived. Building on this, a stability constraint is identified, separating the equilibria into the inner unstable equilibrium and outer stable equilibrium. As the outer stable equilibrium is a potential end state of binary evolution, the dynamical structure about the equilibrium is investigated to understand current binaries. For both the planar and nonplanar cases of the F2BP, the dynamical families about the outer equilibrium are characterized and explored. While the inner unstable equilibrium is rarely observable in nature, it is a vital step in the formation of binary asteroids. A number of past studies have shown this equilibrium to behave as a barrier to binary fission. To understand how higher order and nonplanar effects impact binary formation, we study the inner equilibrium. The results reveal a much more complicated behavior near the unstable equilibrium than previously identified.

3.1 Doubly Synchronous Equilibria of the Full Two-Body Problem

The high dimensionality of the F2BP makes dynamical analysis of the general system complex and unwieldy. We thus turn to the doubly synchronous equilibrium for use as a simplified dynamical sandbox. For the F2BP the doubly synchronous equilibrium occurs when the bodies are principally aligned, tidally locked, and co-orbiting. While this definition of the equilibria allows for any number

of combinations of principal axis alignment, we assume long axis alignment as this is the only condition for which the dynamics can cause passive realignment. Thus only the long-axis alignment can achieve stability conditions beyond marginal stability. Two such equilibria exist in the F2BP, referred to here as the inner and outer solutions. The inner equilibrium exists for a separation when the two bodies are nearly touching and the outer exists when the two bodies are separated by multiple radii of the primary. Only the outer solution is stable and seen in nature, while the inner equilibrium is unstable[6]. In order to compute the doubly synchronous equilibria for a given system the amended potential and its partials with respect to the degrees of freedom must be investigated[54]. The amended potential is defined as

$$\mathcal{E} = \frac{H^2}{2\mathbf{I}_H} + U \quad (3.1)$$

Where H is the angular momentum magnitude and \mathbf{I}_H is the moment of inertia about the angular momentum axis,

$$\mathbf{I}_H = \hat{H} \bullet \left(\mathbf{I}_A + \mathbf{I}_B + m \left[R^2 \bar{\bar{\mathbf{U}}} - \vec{r}\vec{r} \right] \right) \bullet \hat{H} \quad (3.2)$$

the matrix $\bar{\bar{\mathbf{U}}}$ denotes the identity matrix and \bullet denotes the dot product. The scalar m is the reduced mass

$$m = \frac{M_1 M_2}{M_1 + M_2} \quad (3.3)$$

Where M_1 and M_2 denote the masses of the primary and secondary. \hat{H} defines the unit direction of the angular momentum .

$$\hat{H} = \begin{bmatrix} \cos \delta \\ \sin \delta \sin \lambda \\ \sin \delta \cos \lambda \end{bmatrix} \quad (3.4)$$

Where δ and λ are the nutation and precession angles respectively.

Based on knowledge of the doubly synchronous equilibrium orientation, we can simplify \mathbf{I}_H to

$$I_H = I_{A,zz} + I_{B,zz} + mr^2 \quad (3.5)$$

The subscript zz denotes the z-axis moment of inertia, or the polar moment of inertia for the body.

For a given angular momentum of the system and set of mass parameters, the zeroes of the partials of the amended potential with respect to the system degrees of freedom can be used to identify an equilibrium.

$$\mathcal{E}_{\vec{r}}, \mathcal{E}_{\dot{\vec{r}}}, \mathcal{E}_{\vec{\theta}}, \mathcal{E}_{\dot{\vec{\theta}}}, \mathcal{E}_{\delta}, \mathcal{E}_{\lambda} = 0 \quad (3.6)$$

The detailed formulation of the amended potential partials used to find the extrema are

$$\frac{\partial \mathcal{E}}{\partial \vec{r}} = -\frac{H^2}{I_H^2} m \left[I_{3x3} - \hat{H} \hat{H} \right] \bullet \vec{r} + \frac{\partial U}{\partial \vec{r}} \quad (3.7)$$

$$\frac{\partial \mathcal{E}}{\partial \vec{\theta}} = -\frac{H^2}{2I_H^2} \frac{\partial I_H}{\partial \vec{\theta}} + \frac{\partial U}{\partial \vec{\theta}} \quad (3.8)$$

$$\frac{\partial \mathcal{E}}{\partial \xi} = -\frac{H^2}{2I_H^2} \left[2\hat{H} \bullet I_T \bullet \frac{\partial \hat{H}}{\partial \xi} \right] \quad (3.9)$$

Where ξ is either λ or δ

To be stable, the Hessian of the amended potential evaluated at the equilibrium point must be positive definite.

$$\|\mathcal{E}_{\vec{X}\vec{X}}\|_{eq} > 0 \quad (3.10)$$

In Scheeres 2009 it is shown that for the long-axis aligned equilibria the Hessian condition for stability can be reduced to a function purely of the relative separation magnitude, R [6]. As such the condition becomes

$$\mathcal{E}_{RR} > 0 \quad (3.11)$$

Heuristically this inequality is a balance of the potential energy and angular momentum sensitivities to the relative separation based on Eq. 3.1

$$-\frac{\partial^2}{\partial R^2} \left[\frac{H^2}{2I_H} \right] > \frac{\partial^2}{\partial R^2} [U] \quad (3.12)$$

Table 3.1: Physical Properties of The Doubly Synchronous 617 Patroclus modeled in this study

Density	Primary			Secondary			Orbit	
ρ [kg/m^{-3}]	a [km]	b [km]	c [km]	a [km]	b [km]	c [km]	r [km]	Period [days]
881	63.5	58.5	49	58.5	54	45	664.6	4.41

By inspection, a larger separation minimizes the mutual gravity potential such that the outer equilibrium is able to meet the stability criterion described in Eq. 3.11, while the inner equilibrium would be unable to meet this criterion. A more rigorous derivation of this stability is available in Scheeres 2009 and is discussed for the planar case in Sec. 3.2.1[6].

3.2 Stability and Structure about the Outer Equilibrium

To best understand the dynamics of binary asteroids observed in nature we leverage the dynamical structure about the stable outer equilibrium to draw conclusions about the general motion of stable binary systems. While this will not provide a full description of the potential behaviors of observed binary asteroids it will help build intuition for the mutual motion and behaviors of these systems. We begin the analysis by further simplifying to the planar problem. Within the planar problem we identify the stability condition for the outer equilibrium and the linearized dynamical families about the equilibrium. We then use continuation techniques to map the nonlinear dynamical families of the system. From this point we return to the nonplanar problem and identify the nine dimensional linearized dynamical families.

Throughout this section we apply our analysis to the 617 Patroclus system, a Trojan binary and flyby target of the Lucy mission. The system is believed to consist of two nearly ellipsoidal bodies behaving at or near the doubly synchronous equilibrium. As such it represents a realistic case of the various assumptions applied to the F2BP in this section. The physical parameters describing 617 Patroclus implemented for this study are listed in Table 3.1 and based on the results of the 2013 stellar occultation study performed by Buie et al. In line with the analysis of Buie et al. we assume the system to be homogeneous of constant density[55].

3.2.1 The Planar Problem

To understand the system behavior at a fundamental level, we first simplify it further by applying a planar and second-order assumption. These assumptions reduce the system to four degrees of freedom, as illustrated in Fig. 3.1, such that it can be described as an inertial orbit angle θ , a relative separation magnitude R , and the phase angle of each body relative to the separation line ϕ_1 and ϕ_2 .

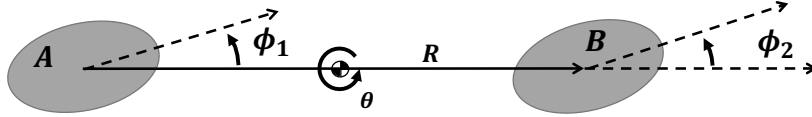


Figure 3.1: Diagram of the planar and second-order F2BP.

The equations of motion for this simplified system can be derived from a Lagrangian analysis of the dynamics[6]. The Lagrangian for the planar problem is

$$L = \frac{1}{2}I_{A,zz}\dot{\phi}_1^2 + \frac{1}{2}I_{B,zz}\dot{\phi}_2^2 + \frac{1}{2}m\dot{R} + \frac{1}{2}(I_{A,zz} + I_{B,zz} + mR^2)\dot{\theta}^2 + (I_{A,zz}\dot{\phi}_1 + I_{B,zz}\dot{\phi}_2)\dot{\theta} - U_{pl}(R, \phi_1, \phi_2) \quad (3.13)$$

Application of Lagrange's equation yields the following EOMs

$$\ddot{R} = \dot{\theta}^2 R - \frac{1}{m} \frac{\partial U_{pl}}{\partial R} \quad (3.14)$$

$$\ddot{\theta} = \frac{1}{mR^2} \frac{\partial U_{pl}}{\partial \phi_1} + \frac{1}{mR^2} \frac{\partial U_{pl}}{\partial \phi_2} - 2 \frac{\dot{R}\dot{\theta}}{R} \quad (3.15)$$

$$\ddot{\phi}_1 = \left(1 + \frac{mR^2}{I_{A,zz}}\right) \frac{1}{mR^2} \frac{\partial U_{pl}}{\partial \phi_1} - \frac{1}{mR^2} \frac{\partial U_{pl}}{\partial \phi_2} + 2 \frac{\dot{R}\dot{\theta}}{R} \quad (3.16)$$

$$\ddot{\phi}_2 = \left(1 + \frac{mR^2}{I_{B,zz}}\right) \frac{1}{mR^2} \frac{\partial U_{pl}}{\partial \phi_2} - \frac{1}{mR^2} \frac{\partial U_{pl}}{\partial \phi_1} + 2 \frac{\dot{R}\dot{\theta}}{R} \quad (3.17)$$

Where U_{pl} is the planar second order simplification of Eq. 2.1.1

$$U_{pl} = -\frac{GM_1M_2}{r} \left\{ 1 + \frac{1}{2R^2} \left[\text{Tr}(\bar{I}_A) + \text{Tr}(\bar{I}_B) - \frac{3}{2} (I_{A,xx} + I_{A,yy} + I_{B,xx} + I_{B,yy} - \cos 2\phi_1 (I_{A,yy} - I_{A,xx}) - \cos 2\phi_2 (I_{B,yy} - I_{B,xx})) \right] \right\} \quad (3.18)$$

For this realization of the system, the conditions for the doubly synchronous equilibrium can be restated using the system states to specify axial alignment and a circular mutual orbit[56].

$$\phi_1 = \phi_2 = \dot{\phi}_1 = \dot{\phi}_2 = \dot{R} = 0 \quad (3.19)$$

By definition of an equilibrium we can also define the constraint

$$\ddot{\phi}_1 = \ddot{\phi}_2 = \ddot{\theta} = 0 \quad (3.20)$$

Thus the necessary equilibrium rotation rate, $\dot{\theta}^*$, for an equilibrium separation, R^* is

$$\dot{\theta}^{*2} = \frac{1}{mR^*} \frac{\partial U_{pl}}{\partial R} \quad (3.21)$$

$$\dot{\theta}^{*2} = \frac{G(M_1 + M_2)}{R^{*3}} \left[1 + \frac{3}{2R^{*2}} \left[\text{Tr}(I_A) + \text{Tr}(I_B) - 3I_{A,xx} - 3I_{B,xx} \right] \right] \quad (3.22)$$

The separation still must be selected to ensure the stability of the equilibrium as defined by the second partial of the amended potential in Eq. 3.11. With the planar and second-order

assumption the relative separation can be reduced to a scalar value which allows us to identify the condition for stability[6].

$$R^* > \sqrt{\frac{3(I_{A,zz} + I_{B,zz})}{m}} \quad (3.23)$$

3.2.2 Linear System Dynamical Families

Because the doubly synchronous equilibrium is an energetically stable arrangement, oscillations about the equilibrium will move along closed cycles, referred to as dynamical families. In their linear form each dynamical family has an associated and unique frequency which can define a dynamical family or periodic orbits. This results from the purely imaginary eigenvalue associated with the given dynamical family[57]. To begin this analysis, we first must identify the eigenvalues of the dynamical system. This is accomplished by computing the characteristic equation of the linearized system. The linearized dynamics are described by

$$\dot{\vec{X}} = \mathbf{A}\vec{X} = \begin{bmatrix} 0 & 0 & 0 & 0 & 1 & 0 & 0 & 0 \\ 0 & 0 & 0 & 0 & 0 & 1 & 0 & 0 \\ 0 & 0 & 0 & 0 & 0 & 0 & 1 & 0 \\ 0 & 0 & 0 & 0 & 0 & 0 & 0 & 1 \\ \frac{\partial \ddot{R}}{\partial R} & 0 & \frac{\partial \ddot{R}}{\partial \phi_1} & \frac{\partial \ddot{R}}{\partial \phi_2} & 0 & \frac{\partial \ddot{R}}{\partial \theta} & 0 & 0 \\ \frac{\partial \ddot{\theta}}{\partial R} & 0 & \frac{\partial \ddot{\theta}}{\partial \phi_1} & \frac{\partial \ddot{\theta}}{\partial \phi_2} & \frac{\partial \ddot{\theta}}{\partial R} & \frac{\partial \ddot{\theta}}{\partial \theta} & 0 & 0 \\ \frac{\partial \ddot{\phi}_1}{\partial R} & 0 & \frac{\partial \ddot{\phi}_1}{\partial \phi_1} & \frac{\partial \ddot{\phi}_1}{\partial \phi_2} & \frac{\partial \ddot{\phi}_1}{\partial R} & \frac{\partial \ddot{\phi}_1}{\partial \theta} & 0 & 0 \\ \frac{\partial \ddot{\phi}_2}{\partial R} & 0 & \frac{\partial \ddot{\phi}_2}{\partial \phi_1} & \frac{\partial \ddot{\phi}_2}{\partial \phi_2} & \frac{\partial \ddot{\phi}_2}{\partial R} & \frac{\partial \ddot{\phi}_2}{\partial \theta} & 0 & 0 \end{bmatrix} \begin{bmatrix} R \\ \theta \\ \phi_1 \\ \phi_2 \\ \dot{R} \\ \dot{\theta} \\ \dot{\phi}_1 \\ \dot{\phi}_2 \end{bmatrix} \quad (3.24)$$

where the details of each element are described in Appendix A. The eigenvalues of the system are roots of the characteristic equation

$$|\mathbf{A} - \lambda \mathbf{I}_{8 \times 8}| = 0 \quad (3.25)$$

which can be related to a period of motion of the linearized oscillations

$$P_{\beta_i} = \frac{2\pi}{\mathbf{Im}(\lambda_i)} \quad (3.26)$$

Table 3.2: Linear periods and unit direction of dynamical families about the planar doubly synchronous equilibrium evaluated for the 617 Patroclus system.

Families	Linear Period [days]
r	3.93
ϕ_1	13.60
ϕ_2	12.12
Orbit Period	4.41

Here β_i specifies the imaginary component of the corresponding root or eigenvalue, λ_i . The described periodic behavior moves along a linear dynamical family defined by a deviation vector from the equilibrium

$$\delta\vec{X}_{\lambda_i} = \frac{\mathbf{Re}(\vec{u}_i)}{\|\mathbf{Re}(\vec{u}_i)\|_2} \cos \theta_i + \frac{\mathbf{Im}(\vec{u}_i)}{\|\mathbf{Im}(\vec{u}_i)\|_2} \sin \theta_i \quad (3.27)$$

Where \vec{u}_i are the eigenvectors corresponding to a given eigenvalue.

For the planar system we have already identified one fundamental frequency in the form of the equilibrium orbit rate constraint, $\dot{\theta}^*$. The eigen decomposition provides an additional three oscillations, or fundamental frequencies. Each is associated with one of the planar states; that is the relative separation R , and the primary and secondary phase angles, ϕ_1 and ϕ_2 . Because the orbit angle θ is an ignorable coordinate it has a zero eigenvalue and thus no associated frequency from the eigen decomposition. In Table 3.2 the linear periods for the 617 Patroclus system, a doubly synchronous binary flyby target of the Lucy mission, are listed.

3.2.3 Continuation of the Planar Dynamical Families

We next turn to a nonlinear analysis of the dynamical families to understand the robustness of the behavior of these oscillations to nonlinearities in the dynamics. Nonlinear dynamical families can be thought of as a family of periodic cycles centered about an equilibrium point defined by some corresponding eigenvalue and eigenvector pair. The eigenvector can be used to define the deviation direction of the dynamical family from the equilibrium. The family of periodic cycles grows more complex in its behavior as it is perturbed further from the central equilibrium point, but each cycle is functionally parallel to its nearest neighbors and each member cycle of the family

can be shown to be perpendicular to a family tangent vector along its entire period[57]. This is analogous to the resonances often used in solar system studies, but provides an approach agnostic to the types of dynamics and states selected to model a given system. To map the behavior of a nonlinear dynamical family, continuation methods leverage the family tangent and similarity between neighbors to step through a set of periodic cycles in the dynamical family. The specific method used herein applies techniques used by Howell and Olikara who implemented a family tangent constraint and phase constraint to step between cycles in the family, Eq. 3.28[58].

$$F(\vec{x}_0, T) = \vec{0} = \begin{bmatrix} \vec{x}_F - \vec{x}_0 \\ \langle \vec{x}_0 - \tilde{\vec{x}}_0, \dot{\tilde{\vec{x}}}_0 \rangle \\ \langle \vec{x}_0 - \tilde{\vec{x}}_0, \tilde{\vec{x}}_0' \rangle + (T - \tilde{T})\tilde{T}' - \Delta s \end{bmatrix} \quad (3.28)$$

In this method each cycle in a family is computed by a shooting method which corrects to an initial guess of the cycle such that it becomes a closed periodic trajectory. This aspect of the continuation method is represented as the first entry in Eq. 3.28 relating the initial and final states, \vec{x}_0 and \vec{x}_F respectively. Next the continuation method enforces the Poincare phase constraint, the second row of Eq. 3.28, which ensures that each cycle in the family is at the same phase as the previous cycle. The previous cycle is represented here by the tilde. In this case the phase constraint ensures that change in the initial conditions between the current cycle, \vec{x}_0 , and the previous cycle, $\tilde{\vec{x}}_0$, is perpendicular to the previous cycle's initial state changes, $\dot{\tilde{\vec{x}}}_0$. Finally, the continuation method uses a pseudo-arclength continuation constraint to ensure the cycle lies along the family tangent, the final row of Eq. 3.28. Here the family tangent is approximated by the fundamental period and dynamical family deviation of the previous cycle in the continuation, \tilde{T}' and $\tilde{\vec{x}}_0'$. The pseudo-arclength aspect of the continuation comes from the pseudo-arclength magnitude, Δs , a tuning parameter which limits the size of the continuation step by limiting the amount of change in the initial states or cycle period between continuation steps. When computing a continuation for a given dynamical family, the vector $F(\vec{x}_0, T)$ is differentially corrected to the zero vector for each periodic cycle in the family. After each cycle converges, an initial guess of the family tangent is used to initialize the next cycle in the family. We perform this analysis for each of the three

dynamical families about the planar doubly synchronous equilibrium and find that their behavior remains closed and periodic as each trajectory is perturbed relatively far from the equilibrium. This shows that the fundamental frequencies are feasibly identifiable in the vicinity of the doubly synchronous equilibrium for estimation.

Using this continuation method, the dynamical families for the relative separation r , and the phase angles, ϕ_1 and ϕ_2 , are explored in the nonlinear regime, Fig. 3.2-3.4. We can see from these dynamical families that orbits remain periodic as they are perturbed further into the nonlinear regime and that for the coordinates, the topology of the trajectories does not change significantly. This is especially true for the relative separation dynamical family which appears to mimic a Keplerian elliptic orbit with simple oscillations of the phase angles, even when perturbed far from the equilibrium. The rates in the dynamical family for the secondary phase angle shows more complex behavior, changing from a one-cycle to a three-cycle trajectory. The amount of coupling between the three states hints at difficulties in extrapolating the mass parameters from these dynamics.

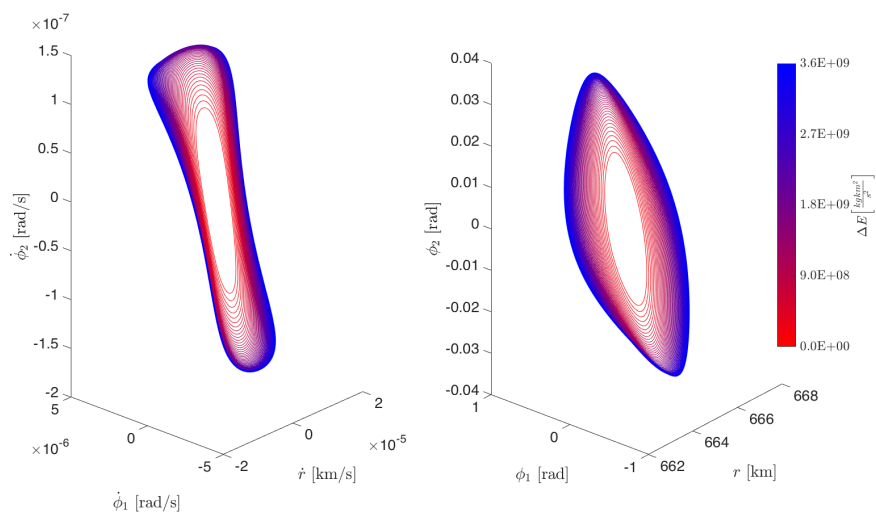


Figure 3.2: Nonlinear dynamical family about the planar doubly synchronous equilibrium associated with the primary phase angle, ϕ_1 . Where ΔE is the increase in energy away from the equilibrium energy.

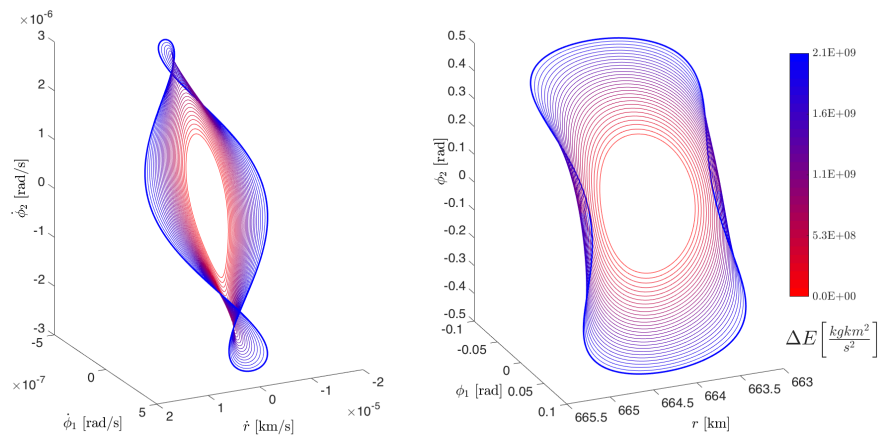


Figure 3.3: Nonlinear dynamical family about the planar doubly synchronous equilibrium associated with the secondary phase angle, ϕ_2 . Where ΔE is the increase in energy away from the equilibrium energy.

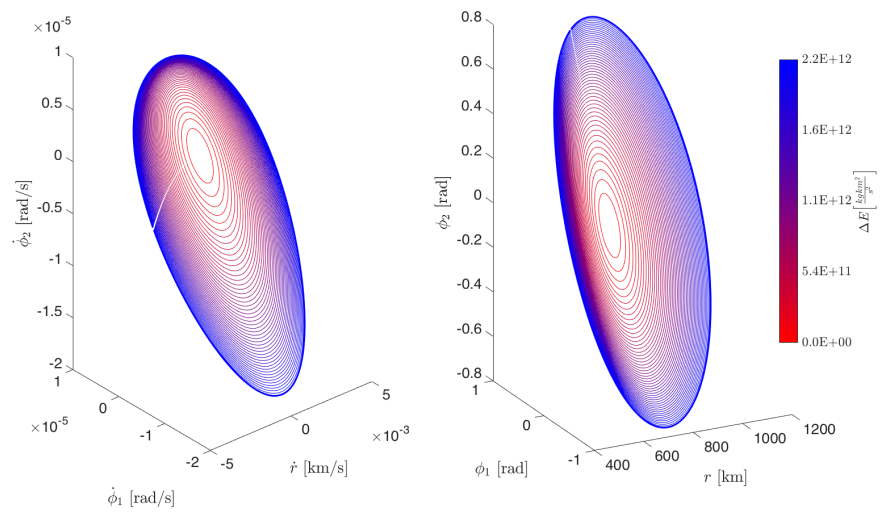


Figure 3.4: Nonlinear dynamical family about the planar doubly synchronous equilibrium associated with the relative separation, r . Where ΔE is the increase in energy away from the equilibrium energy.

3.2.4 Expansion to the Nonplanar Problem

The restrictions of the planar system enable a simple, but limited, approach to detailed analysis of the dynamics. However, understanding the impact of out-of-plane motion on the number of dynamical families and their behavior is vital for a full understanding of the real dynamics. We thus expand our dynamics model to the more general model with the mutual gravity potential truncated at order two, recalling Eq. 2.2 and 2.3. The dynamics matrix for the nonplanar case can be found in Appendix A. The increased dimensionality of the nonplanar system results in seven system dynamical families from the eighteen states, as opposed to the three families from eight states in the planar problem. There are also two ignorable coordinates associated with zero-valued eigenvalues as opposed to the single ignorable coordinate of the planar case. Because of the complexity of developing the mutual gravity potential and torques as well as the equations of motion we choose not to reduce the state representation to a minimal set. Because the doubly synchronous behavior does not change from the planar to nonplanar dynamics the $\dot{\theta}$ constraint remains unchanged. The behaviors of each of these eight fundamental frequencies are illustrated in Fig. 3.5.

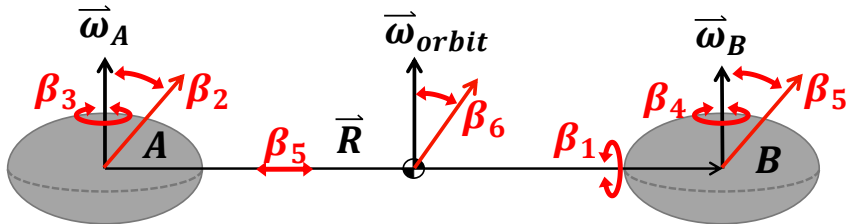


Figure 3.5: Diagram of the nonplanar doubly synchronous equilibrium and surrounding linear dynamical families.

Table 3.3: Linear periods of dynamical families about the nonplanar doubly synchronous equilibrium evaluated for the 617 Patroclus system.

Families	Behavior	Linear Period [days]
β_1	Rel. Twist	18.97
β_2	Pri. Precession	15.67
β_3	Pri. Libration	13.65
β_4	Sec. Libration	12.13
β_5	Rel. Separation	4.41
β_6	Orbit Precession	3.86
β_7	Sec. Precession	2.91
Orbit Period	Orbital Motion	4.41

We see that the three dynamical families from the planar case remain for the nonplanar case, now being referred to as β_3 , β_4 , and β_5 . Two of the new dynamical families are associated with precession and nutation of the primary and secondary, respectively β_2 and β_7 . The remaining two new dynamical families are associated with a relative axial twist about the radial axis, β_1 , and the precession and nutation of the orbit plane, β_6 . The periods of the linear dynamical families for these fundamental frequencies are shown for the 617 Patroclus system in Table 3.3.

3.3 Stability and Structure about the Inner Equilibrium

While the inner unstable equilibrium cannot provide direct insight into the current dynamics of binary asteroids, it plays an important role in binary formation. The inner equilibrium acts as a dynamical barrier to asteroid fission and thus is a key pathway for binary formation. In Scheeres 2009 the structure about the second-order planar unstable inner equilibrium was explored, initially revealing this dynamical barrier, Fig. 3.6[6].

The figure illustrates the zero-velocity curves, in red, of the second-order planar F2BP given the critical fission angular momentum of an asteroid. The blue dashed line indicates the normalized energy of the inner unstable equilibrium and functions as an upper bound for the allowable region assuming a conservative system. The inner equilibrium itself is the local maxima near a normalized radius of 1, where the normalizing parameter is the minimum separation between the two bodies. If

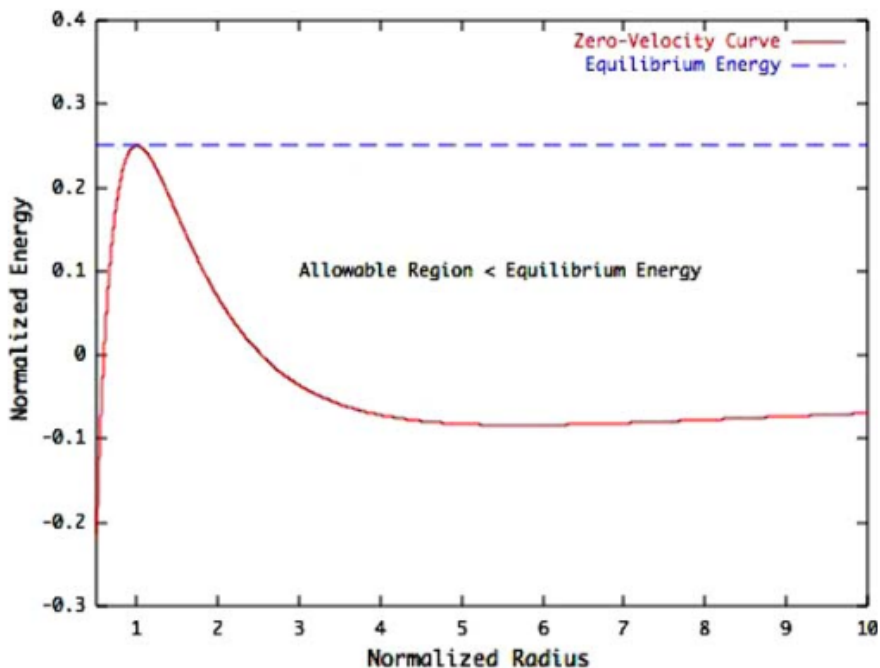


Figure 3.6: Diagram from Scheeres 2009 which depicts the energy of a second order planar ellipsoid-ellipsoid binary as a function of the primary’s radius for a fixed angular momentum[6].

a fissioning secondary is located at a lower normalized radius it will recollide with the primary. If the normalized radius is greater than that of the inner equilibrium it will enter a chaotically captured orbit about the primary bounded by the allowable region. When expanding to the arbitrary order nonplanar F2BP the dynamical structure identified by Scheeres 2009 is warped significantly such that even the principal alignment of the equilibrium breaks down. In this section we identify the changes to the state of the inner equilibrium as well as the dynamical structure surrounding it

In trying to expand the understanding of binary formation from a planar and second order model, we first identify the changes to the unstable equilibrium with these assumptions lifted. To compute the generalized state of the inner unstable equilibrium under nonplanar and arbitrary order conditions we move away from the amended potential and instead identify the state that nullifies the equations of motion presented in Sec. 2.1. Using a Newton-Raphson differential corrector and the nonplanar dynamics matrix in Appendix A we can identify the equilibrium state given system parameters and a truncation order. The differential corrector constrains only the system

spin rate, leaving all other states free to be varied. For the examples herein we compute the inner equilibrium for the well characterized asymmetric binary 66391 Moshup evaluated at order 4[1], Fig. 3.7. For comparison we also compute the equilibrium state for Moshup evaluated at order 2. Both equilibrium states are shown from an isometric view in the primary fixed frame; looking 45 degrees downward and perpendicular to the relative separation vector. The top image shows the equilibrium evaluated at order 2 with a red secondary and the bottom image shows the fourth order evaluation with a blue secondary. While both evaluations of the equilibrium appear to maintain

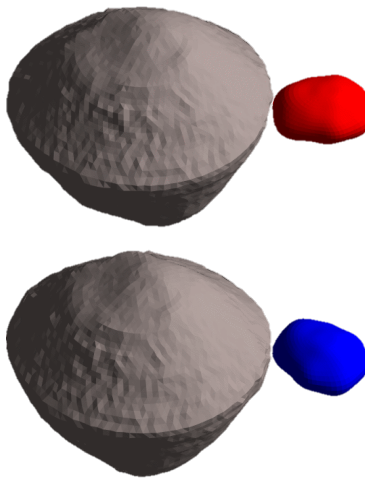


Figure 3.7: Relative geometry of inner unstable equilibrium evaluated at order 2 (above) and order 4 (below).

nearly identical relative separations the relative attitudes clearly differ. When the equilibrium is evaluated at the second order it maintains the principal alignment condition. Whereas, for the fourth order, the relative attitude of the secondary is rotated about the out of plane axis. Once asymmetric higher order terms are accounted for, gravity torques are able to pull the system away from principal alignment as seen for the fourth order evaluation. It is of note that this does not occur for the outer equilibrium because the bodies are much further apart in that case. There may exist a higher order facsimile for axial alignment found by appropriate rotation of a body's inertia integrals which can explain this torquing. Such a derivation however does not serve the

goal of this work as the current approach is still able to identify the equilibrium geometry. The change in alignment, combined with the higher dimensionality when moving from the planar to nonplanar problem, warps the zero-velocity curves at the equilibrium such that the equilibrium no longer acts as a boundary to collision. To illustrate this, Fig. 3.8 shows the relative separation magnitude evolution when the Moshup system is perturbed slightly from the order 2 and order 4 inner equilibria. The bodies are considered to collide when they fall below the collision separation value shown in black. As is shown, the order 2 system shows chaotic orbit capture which comes

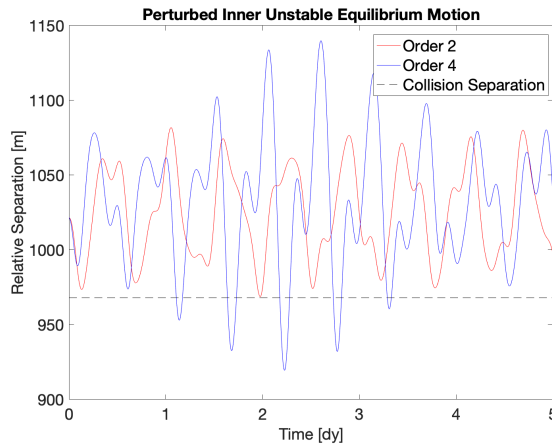


Figure 3.8: Relative separation of Moshup dynamics when perturbed slightly from inner equilibrium state evaluated for the given order of the dynamics.

close, but does not, recollide. On the other hand the order 4 system can be seen to collide several times. It is of note that the numerical integration does not sense collisions and because of the nature of the inertia integrals the equations of motion will not hit a singularity unless the bodies fully envelop one another. The recollision shown for the order 4 system is possible because the nonplanar and asymmetric higher order terms can excite the relative attitude and break down the zero-velocity curve structure shown for order 2 in Fig. 3.6.

3.4 Summary

This chapter identifies the conditions for equilibria in the F2BP and their stability. Equilibria are split into the inner unstable and outer stable equilibria. Analysis of the outer stable equilibrium

identifies the dynamical families and structure about the equilibrium for the planar and nonplanar problem. The increased fidelity provided by the arbitrary shape and order implementation of the F2BP enables a more detailed look at these dynamics than past studies. The analysis finds several families of oscillations about the stable equilibrium which Ch. 5 will leverage to estimate the mass parameters of binaries near the outer equilibrium. In the analysis of the inner unstable equilibrium it is shown that nonplanar and higher order dynamics warp the dynamical structure about the equilibrium, such that it is not longer a barrier to collision as for the second order. This distortion of the dynamical structure has potential impact on the formation processes and evolution of binary asteroid systems. This is explored in Ch. 4.

Chapter 4

Binary Formation Via Rotational Fission At the Inner Unstable Equilibrium

Within this chapter we identify the influence of higher order and nonplanar dynamics on the binary formation process described in Jacobson and Scheeres 2011 (JS2011)[30]. In their work, Jacobson and Scheeres identified a dynamical path from YORP induced rotational fission of single asteroids to the various forms of binary and multi-body asteroid systems seen throughout the inner Solar System. One key discovery of which, was structural fission of the secondary asteroid as a means of energy dissipation in low mass ratio binaries. Their proposed process begins from the inner unstable equilibrium. In Sec. 3.3 we showed that this equilibrium and dynamical structure are significantly distorted by increasing the fidelity of the F2BP dynamics model. In order to broadly capture the behavior of different types of binary systems, we study three representative systems: 66391 Moshup (1999 KW4), 1996 HW1 and 2000 DP107. These example systems represent low mass ratio binaries (Moshup and DP107) and high mass ratio binaries (HW1). We also use DP107 to test the feasibility of the Tardivel et al. proposal that NEA equatorial craters may be markers of binary fission[41]. For all three systems, the initial fission geometry, shown in the figure, is analogous to that of a fissioning contact binary. The fission geometry of all three systems is illustrated in Fig. 4.1

For each system we perform a Monte Carlo analysis of the binary fission conditions centered about the unstable inner equilibrium. To match the JS2011 study we include dynamical perturbations coming from solar gravity and mutual tidal torques between the asteroids. Each Monte Carlo analysis considers the first year of evolution after fission and sorts the results into four binary

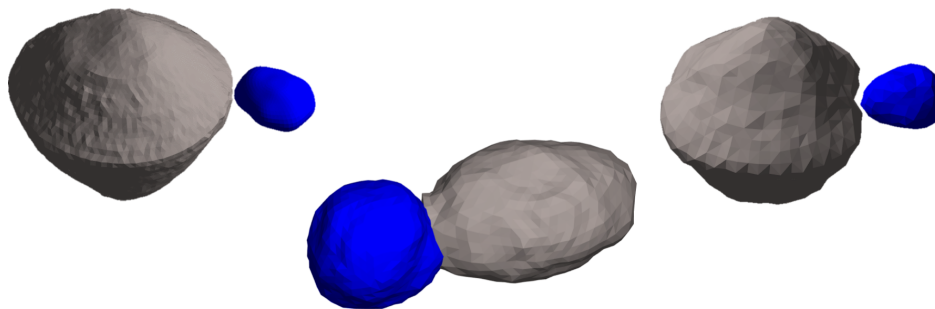


Figure 4.1: Fission conditions for modeled asteroids with primaries colored grey and secondaries colored blue. From left to right: Moshup, 1996 HW1, 2000 DP107

fates: recollision, escape, secondary fission and chaotic orbital capture. The statistical breakdown of these binary fates are then compared with the results of JS2011 in addition to the more detailed conditions of the fate for each simulation. In general we find agreement between our high fidelity model and the results of JS2011. However, some significant discrepancies are identified relating to the spin state of escaping secondaries, the differing models of secondary fission, and recollision of the asteroids.

4.1 Perturbed Dynamics Model

The goal of our dynamics model is to capture the higher order effects of the mutual gravity interactions between both bodies as well as the other significant perturbations experienced by the system. We use the inertia integral model of the F2BP to capture the mutual gravity interactions of the bodies, accounting for nonplanar effects and gravity terms up to the fourth order for both bodies[28]. This model, as described in Sec. 2.1, also assumes the bodies to be rigid, unlike previously mentioned work by Walsh et al. and others since[13][59]. Because our study is concerned with the dynamical evolution as opposed to the fission mechanics at work, we do not include the effects of non-rigidity beyond tidal torques. In order to account for the mutual tidal torques between the bodies we apply the model described by Murray and Dermott[60][61]. For our solar gravity model we build on the relative Hill acceleration models described in Jacobson and Scheeres as well as Fahnestock and Scheeres [30][24]. In addition to the integrated dynamics, our post-processing

analysis evaluates the dynamics for cohesive failure of the secondary, referred to for simplicity as secondary fission.

4.1.1 Tidal Torques

The tidal torques arise from reshaping of a body due to a gravitational pull from another body which forms a tidal bulge on the surface. This is the same process by which the Moon incites ocean tides on the Earth. Throughout an orbit the influence of gravity on the tidal bulge can induce a torque on the body. For fissioning rubble-pile binaries this can be an important effect. To model the tidal torques we implement the classical model described in Murray and Dermott[60][61]. This model simplifies the system to a sphere orbited by a point mass where the sphere is torqued by the motion of the point mass. For the purposes of our dynamics model this torque is accounted for on both bodies simultaneously. The torque induced on the body of interest is

$$\Gamma_i = \text{sgn}(\vec{\omega}_i \cdot \vec{\Omega}) \frac{3}{2} k_i \left(\frac{3}{4\pi\rho_i} \right)^2 \frac{GM_i^2 M_j^2}{r_{ij}^6 R_i} \sin \frac{1}{Q_i} \quad (4.1)$$

where $\vec{\omega}_i$ is the inertia spin rate of the body, $\vec{\omega}_i$ is the orbital angular velocity, r_{ij} is the relative position magnitude between the bodies and R_i is the mass-equivalent spherical radius of the body. The quantities k_i and Q_i describe the structural elasticity of the body. k_i is the tidal love number which describes the rigidity of the body; $k_i = 0$ being a fully rigid body. Q_i is the specific tidal dissipation function which describes the lag between the orbital motion of the point mass and the location of the tidal bulge. By convention these values are considered to be $k_i = 10^{-5}$ and $Q_i = 100$ for rubble-pile asteroids. While this model is only a first order approximation it allows us to capture the the approximate effect of tidal torques on the dynamics and match the model implemented in JS2011.

4.1.2 Solar Gravity

While the mutual gravity of fissioning binaries dominates over most accelerations they might otherwise be experiencing, the effect of their heliocentric orbit on their mutual orbit can also be significant over long periods of time. For simplicity we assume that the binaries remain in the same circular heliocentric orbit throughout their evolution. To capture the effect this has on the binary's mutual orbit we use a Hill approximation to compute a perturbing acceleration[24][30]. This introduces a perturbation to the relative acceleration and mutual orbit spin acceleration as

$$\ddot{r}_{Hill} = 3n^2 r \cos \theta + 2nr\dot{\theta} \quad (4.2)$$

$$\dot{\Omega}_{Hill} = -2nr\dot{\theta} \quad (4.3)$$

Where \ddot{r}_{Hill} is considered along the relative separation vector and $\dot{\Omega}_{Hill}$ is about the mutual orbit normal. The mean motion, n , is based on a circular heliocentric orbital radius and θ is the orientation of the mutual orbit relative to the sun-binary barycenter line.

4.1.3 Secondary Fission

To identify secondary fission, we compute a critical spin rate for cohesive failure and check the secondary's spin rate throughout a simulation. The critical spin rate is computed as a function of elongation, α , density, ρ , strength, σ , angle of friction, ϕ , and the gravity constant, G [62][63].

$$\omega_c^2 = \frac{4\pi G\rho}{3} + \frac{2\sigma}{\rho\alpha^2} \frac{3 - \sin \phi}{3 + \sin \phi} \quad (4.4)$$

Within each simulation the elongation is selected as the long axis of the body. The gravity constant, density and strength are selected based on the selected conditions for the simulation. For the angle of friction we refer to the values studied by Sanchez and Scheeres to analyze cohesive failure, ranging from 45 to 90 deg [64][32]. Using values from either end of this range our analysis does not show significant differences in the critical spin rate beyond fractional percentages.

4.2 Simulation Methodology

The goal of simulation for all three systems studied is to evaluate their dynamic evolution and to understand the influence fission conditions have on their evolved state. Each of the three targets is selected to explore the evolution of different system types: 66391 Moshup (1999 KW4) represents current low mass ratio binaries, 1996 HW1 represents contact binaries and high mass ratio binaries, and 2000 DP107 further explores the low mass ratio regime while also providing insight for formation of equatorial craters from binary fission. For each system we identify the conditions for its fission based on the body shapes and equilibria. A Monte Carlo analysis is then performed with initial conditions perturbed from the identified fission state and simulated for one year of integration time. For simplicity it is assumed that all fissions occur in the ecliptic plane. This assumption likely skews the orbital states of the formed binaries towards being more relaxed, as solar gravity would likely excite more out of plane effects for a binary forming off of the ecliptic. Each simulation is then post-processed to evaluate the fate of the fissioned binary; the fates fall into four categories: collision, escape, secondary fission, and chaotic orbital capture. Collision is assumed to occur when system geometry aligns such that the best fit ellipsoid for each of the two bodies intersect. To account for potential inaccuracies due to this simplified method of collision detection, the ellipsoids are heuristically evaluated to ensure that the moment of collision is accurate to the shape models and gives no false positives or negatives. Escape occurs when the secondary crosses the sphere of influence of the primary's gravity. Secondary fission occurs when the secondary spin rate exceeds the critical spin rate as defined in Eq. 4.4 above. Because we are primarily interested in dynamical events which Jacobson and Scheeres predict to occur within the first one hundred days and the run time of these simulations is significant we limit the numerical integration to one full year. The numerical integration is performed with an adaptive Dormand-Prince RK7(8) while collision detection, escape and secondary fission are evaluated in post-processing[65]. When classifying the fate of each simulation, the processes leading to each fate tend towards the same behavior and similar geometry between similarly categorized simulations for a given binary. As

such little information is lost by using these classifications.

We define the simulations to begin from the moment of fission. Within the framework of the F2BP a binary system must gain enough energy from YORP or other processes to pass through the inner unstable equilibrium of the F2BP. As described in Sec. 3.3, the inner unstable equilibrium acts as an energetic barrier between collision and chaotic orbital capture for the planar second-order model used in JS2011[31][6][30]. We note that this condition for fission assumes non-cohesive fission. In our Monte Carlo we use perturbations from this ideal fission condition to account for the potential increase in the fission spin rate due to weak cohesive forces.

Using the methodology for computing F2BP equilibria described in Ch. 3, we evaluate the inner unstable equilibrium for the fourth order. The angular momentum value for the calculation is selected as the circular orbit rate for near-contact geometry dependent on the system of interest. Our evaluation of the equilibrium at the fourth order finds that the symmetric alignment of the principal axes present for the second order models breaks down as does the barrier this equilibrium represents. As a part of the Monte Carlo investigation we evaluate the perturbation to this barrier. The Monte Carlo conditions for each system are seeded at this equilibrium and perturbed uniformly in their relative position, velocity, fission spin rate, and relative orientation. Perturbation of the relative position and velocity are directed only along the relative separation vector to avoid aliasing with the effects of the spin rate and orientation perturbations. The perturbations of spin rate maintain the direction of the system angular velocity at fission, but vary the magnitude. Relative orientation is perturbed by rotating the orientation of the secondary in all three dimension relative to the equilibrium state. For perturbations of the the position, velocity, and spin rate the values are only increased to avoid reducing the energy of the system below the minimum for mutual orbit. To maintain consistency across the three sample systems we compute the perturbation range as a relative percentage of the computed equilibria.

4.3 Moshup (1999 KW4)

Asteroid Moshup, previously known by its provisional name 1999 KW4, is an asymmetric NEA binary that has been extensively studied since its initial discovery. Radar measurements and shape modeling were performed by Ostro et al. and adopted for this study. The system characteristics are reported in Table 4.1 with the mass parameters computed assuming a constant density of 2.0g/cm^3 .

Table 4.1: Current observed Moshup States based on Ostro et al[1].

Orbit Period [hr]	SMA [m]	Ecc.	Total Mass [kg]	Mass Fraction
17.4223 ± 0.036	2548 ± 15	$4\times 10^{-5} \pm 1.9\times 10^{-3}$	2.61×10^{12}	0.0372

To identify the fission conditions of the Moshup system we compute the inner unstable equilibrium when the bodies are nearly resting on one another. We select the Monte Carlo perturbation to be relatively small, but account for the potential effects of cohesion. The selected initial conditions and perturbations are provided in Table 4.2, where the relative Euler angles are a 1-2-3 set relating the two body frames.

Table 4.2: Monte Carlo conditions for Moshup analysis.

State	Equilibrium Value	Lower Pert. Bound	Upper Pert. Bound
Radial Separation [m]	1038.7	0.0	25
Radial Velocity [mm/s]	0.0	0.0	2.0
System Spin Rate [rad/s]	4.029×10^{-4}	0.0	2×10^{-5}
Rel. Euler Axis 1 [deg]	0.07	-30	30
Rel. Euler Axis 2 [deg]	-0.15	-30	30
Rel. Euler Axis 3 [deg]	20.84	-30	30

The simulations of the Moshup system provide us with a well-characterized binary to explore low mass ratio binary fission. Of the 150 simulated cases the majority either collide or experience secondary fission, with a subset of secondaries escaping and a handful remaining in a chaotic captured orbit. Table 4.3 provides the statistical breakdown of these results along with the median time for the different evolutionary events to occur.

Table 4.3: Statistical results for Moshup formation simulations

Fate	Captured	Collision	Escape	Secondary Fission
#	4	64	27	55
%	2.7%	42.7%	18.0%	36.7%
Median Time	N/A	0.52 dy	131.7 dy	84.1 dy

A few immediate comparisons can be made between these results and those of JS2011. Most significant is the occurrence of recollision after the moment of fission. Recollision appears to be limited to within the first two days after fission, with the majority occurring within the first half day. These recollisions likely occur as a result of higher-order and asymmetric mass parameters warping the topology around the unstable equilibrium such that the allowable region of the dynamics no longer excludes the full primary’s surface. In the case of secondary fission we also see that our rate of secondary fission, 36.7%, falls within the $40\% \pm 4\%$ rate seen in JS2011. This comparison is not one to one, as our model for secondary fission accounts for cohesion. JS2011 has no cohesion, but assume full disruption of the secondary. We explore the effect of the secondary fission model later in the section. Finally, we see that the rate of chaotic capture is almost identical to the 2% seen in JS2011. The clearest point of disagreement is the median time for each events with escape and secondary fission taking roughly 5 to 10 times as long to occur. This slowing of the evolution and disruption of the system results from the slower angular momentum transfer from the primary to the secondary under the higher fidelity dynamics; JS2011 in fact predicts this.

4.3.1 Recollision

Looking more closely at the recollision events, we can better understand the nature and potential result of the collision. The two key factors of interest here are the location of the impact on the primary and the surface velocity of the impact. We define the surface velocity as the relative velocity between the surface of the primary and secondary at the moment of collision as opposed to the relative velocity between the centers of mass. In Fig. 4.2 the locations of collision on the Moshup primary are identified along with the magnitude of the surface velocity at the moment of

impact. The points in the figure are colored by the magnitude of the surface velocity at impact. All secondary's are initialized roughly at the equator as identified by the arrow. The point of maximum extent identifies a bulge on the equatorial ridge that is roughly 20 meters further from the center of mass than the rest of the equatorial ridge.

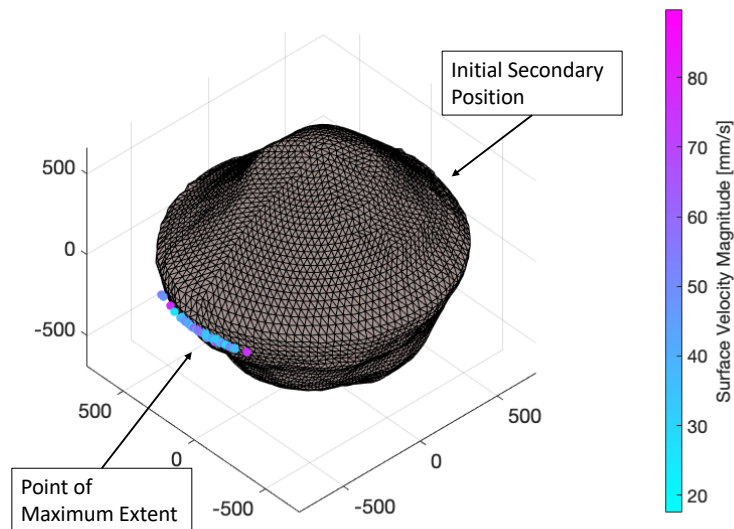


Figure 4.2: Location of impact locations for collision cases shown in the body fixed frame of the Moshup primary.

It is clear that the collisions bias towards the location of maximum extent. This occurs because that location extends roughly 20 meters further from the center of mass than the rest of the equatorial bulge. Thus secondaries orbiting just above the surface of the primary will hit this location first. The surface velocity for these collisions ranges from about 20-90 mm/s. This would be a slow grazing collision unlikely to cause significant fracturing of either body. For context a fall from 1 cm on Earth will have an impact velocity of about 50 mm/s. We further probe the impact conditions by mapping the directional distribution of the surface velocity at impact, as in Fig. 4.3. The velocities are provided in the secondary's orbit frame where the radial direction is from the primary's center of mass to that of the secondary, the cross-track direction is along the orbit in the direction of the orbital motion and the normal direction is along the orbit normal. The surface velocity is the relative velocity between the surface of the primary and secondary at the moment

of impact, accounting for relative spins and velocity.

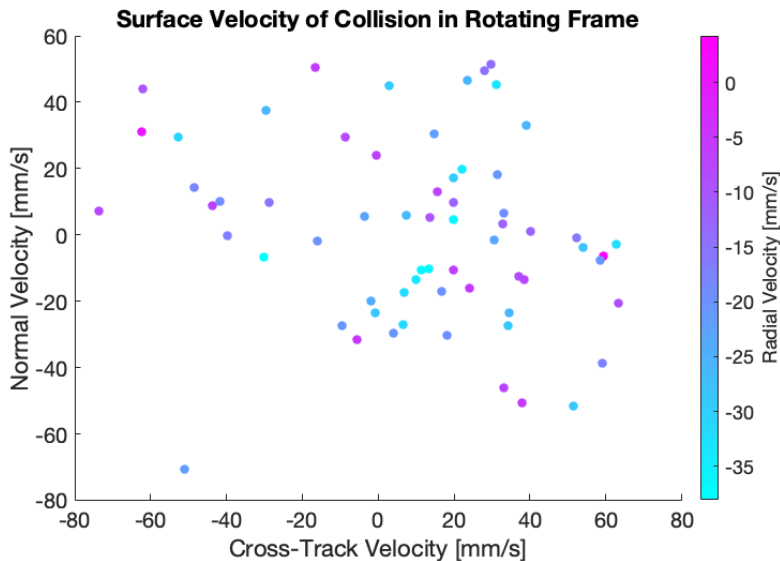


Figure 4.3: Instantaneous surface velocities of colliding secondaries at the moment of impact for Moshup simulations.

The range of the radial impact velocities, shown as the color in the figure, is relatively smaller than the other directions and almost entirely negative, or towards the primary. While positive radial velocity at impact may not be intuitive, it results from combining the rotation of each body and relative velocity into the surface velocity. One can imagine that the secondary may be moving away from the primary but rotate from an orientation with the longest axis pointing along the orbit to an orientation with the longest axis pointing towards the primary, such that the secondary swings tangentially into the surface of the primary. The wide range of cross-track and normal velocities for the impact also implies that these impacts are not only slow but likely would be grazing or rolling collisions as opposed to more violent and direct impacts. Likely this means that simulating the results of any potential reformation of the system would require sophisticated models of the cohesive forces and continuum mechanics at play, an important point for future work.

4.3.2 Secondary Fission

The most interesting aspect of secondary fission in our model is the out of plane behavior of the secondary at the moment of secondary fission. In past studies the dynamics have been assumed to be planar, such that all debris or tertiary bodies remain within the plane. The inclusion of higher fidelity dynamics in our models shows that secondary fission is likely to be a much more complex process. To illustrate this we define the dynamic inertia, I_D , and effective spin of the secondary, ω_l , at the moment of secondary fission as

$$I_D = \frac{H^2}{2T} \quad (4.5)$$

$$\omega_l = \frac{2T}{\sqrt{H^2}} \quad (4.6)$$

where H and T are respectively the angular momentum and kinetic energy of the secondary. Fig. 4.4 illustrates the effective spin and dynamic inertia for the fissioning secondaries of the Moshup system superimposed over the secondary's moments of inertia. The horizontal bars indicate the values of the secondary's moments of inertia. The spin states cluster about the intermediate axis indicating complex tumbling motion at the time of fission

The dynamic inertia of the bodies is clustered about the intermediate axis, implying complex tumbling or separatrix motion. This means that any fissioned debris is likely to enter an excited an out of plane orbit. The implication here is that debris impacting the primary is likely to cause more randomly located and global craters and potential reshaping events. Likewise debris exiting the system may be well out of plane.

In comparing the JS2011 secondary fission behavior to this analysis several differing assumptions must be pointed out and compared. The JS2011 secondary fission model assumes the secondary to be a contact binary made up of two similarly sized spheres without cohesion. In this model the fission of the secondary can be seen as a balance between the spin of the secondary, the mutual gravity between the two spheres making up the secondary and the effects of the primary's gravity on each lobe of the secondary[30]. Our model assumes the material separated from the sec-

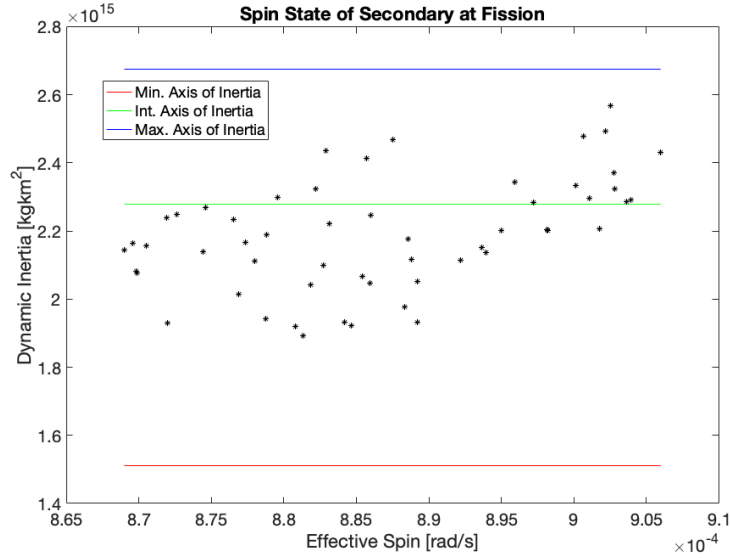


Figure 4.4: Complex spin state of the secondary at the moment of secondary fission for Moshup Simulations.

ondary to be much smaller than the secondary itself such that the gravity of the secondary alone dominates and cohesive forces have a significant effect. As a result we use standard techniques for tracking cohesive failure on single asteroids[64][32]. While we do not presume which model is more accurate, there is value in comparing the results of the two models. To implement the JS2011 secondary fission model we define the mass fraction of the components making up the secondary as $\nu_s = M_b / (M_a + M_b)$, where M_a is the mass of the component initially closest to the primary and M_b is the mass of the component initially further from the primary. To create the bi-lobed secondary for the fission model we constrain the sphere radii such that the total mass of the secondary is constrained to the mass of the polyhedral secondary shape. The centers of each sphere are fixed to the semi-major axis of the polyhedral secondary's principal frame and moved along the axis to maintain the inertial location of the secondary's center of mass. The bi-lobed secondary is only used within the evaluation of secondary fission and does not affect any other aspect of the dynamics model or later analysis. In Table 4.4 we present a comparison of the Moshup results pro-

cessed with our cohesive secondary fission model as well as the JS2011 bi-lobed secondary fission model given a range of values for $\nu_s = M_b/(M_a + M_b)$. The median time for secondary fission is provided in parenthesis in the secondary fission column. The cohesive model is denoted as COH and is described in Eq. 4.4. The bi-lobed sphere model is denoted with BL and the value of ν_s . The entry labelled IBL identifies a secondary fission model which uses the bi-lobed framework, but assumes it is isolated from the primary and thus ignores the gravitational influence of the primary.

Table 4.4: Comparison of secondary fission results for different models of fission for Moshup Simulations.

Model	Secondary Mass Fraction	Captured	Collision	Escape	Secondary Fission
COH	N/A	4	64	27	55 (84.1 dy)
IBL	1.5×10^{-5}	5	64	27	54 (95.6 dy)
BL	1.5×10^{-5}	10	64	36	40 (109.3 dy)
BL	$1-1.5 \times 10^{-5}$	7	64	35	44 (114.2 dy)
BL	1.0×10^{-3}	0	64	11	75(59.1 dy)
BL	$1-1.0 \times 10^{-3}$	0	64	12	74 (61.1 dy)
BL	5.0×10^{-2}	0	63	0	87 (3.7 dy)
BL	$1-5.0 \times 10^{-2}$	0	63	0	87 (3.8 dy)
BL	0.5	0	54	0	96 (1.0 dy)

The first comparison to be made is between the cohesive case and isolated bi-lobed case. If the gravity effects of the primary are ignored and the secondary has a sufficiently small fissioning lobe, $\nu_s=1.5 \times 10^{-5}$ or a lobe radius of about 5 meters, the two models can be easily compared. Both cases have a fairly close median time for secondary fission and see nearly identical secondary fates. Once the gravitational influence of the primary is considered in the lobed model, the results reflect the importance of the secondary mass ratio. Comparing the two $\nu_s=1.5 \times 10^{-5}$ cases we see that that the primary's gravity slows the secondary fission process. Further if we compare to the $\nu_s=1-1.5 \times 10^{-5}$ the significance of the arrangement of the secondary's lobes is also apparent. In general if the smaller lobe begins closer to the primary ($\nu_s > 0.5$) then the secondary fission process is slowed, compared to when the larger lobe is closer to the primary ($\nu_s < 0.5$). As the lobes grow closer in size the secondary fission process speeds up. This is in part because as the smaller lobe

grows relative to the larger lobe of the secondary the separation between their centers grows. Under the inverse square form of the lobes' mutual gravity this reduces the force each lobe exerts on the other. Likewise the growth in mass of the secondary increases the gravitation pull it experiences from the primary. The structure of the secondary, whether it be mostly one coherent mass or an amalgamation of several large masses thus will have significant influence on the secondary fission process. Regardless, it is clear that in most cases secondary fission is a feasible evolutionary event for a low mass ratio binary.

Because the secondary fission analysis is done as a post-processing step, the selection of either model does not affect the out of plane evolution of the system beyond the timing of the fission. This is to say that the out of plane excitement evolves regardless of the secondary fission model. However, when fission occurs earlier in the simulation timeline, there will likely be less out of plane excitement of the secondary. As an example, Fig. 4.5 identifies the complex spin state of the secondary at fission for the bi-lobed case when $\nu_s=0.5$. This case has a very quick median time of secondary fission at roughly 1 day, yet still sees significant excitement of the spin state towards complex or tumbling motion. The horizontal bars indicate the values of the secondary's moments of inertia. The spin states cluster about the intermediate axis indicating complex tumbling motion at the time of fission.

4.3.3 Escape

The cases of escaping secondaries can give us insight into a potential formation process for asteroid pairs. Here the relative velocity at escape and spin states of each body at escape are of interest for comparing to observed asteroid pairs. Because the escape condition here is the moment that the secondary crosses the primary's sphere of influence, we can provide a histogram of relative velocities when a potential asteroid pair could have formed, Fig. 4.6. For reference the sphere of influence for the Moshup primary is 10370 meters.

We see that the relative velocities are fairly slow, on the order of 5-10 cm/s, and fairly well distributed across this range. Once again plotting the dynamic inertia and effective spin of the

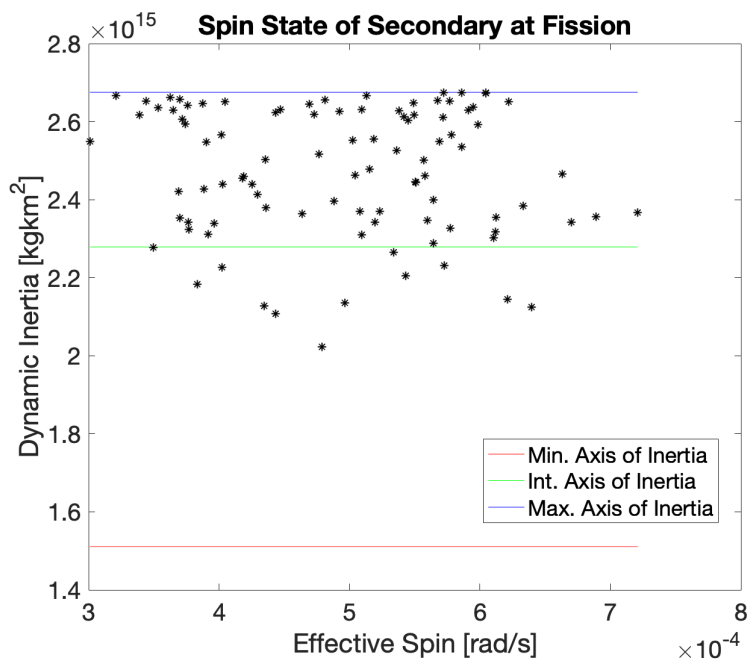


Figure 4.5: Complex spin state of the secondary at the moment of secondary fission using the bi-lobed secondary fission model with $\nu_s=0.5$ for Moshup Simulations.

secondary, we can probe the behavior at the moment of escape, Fig. 4.7.

These spin states imply a fairly excited state for the ejected secondary that would likely have a significant affect on its continued evolution as a single and small complex rotating asteroid. The same cannot be said of the primary whose spin state, Fig. 4.8, is largely unaffected by the ejection of the secondary, beyond the minor effects of the initial fission.

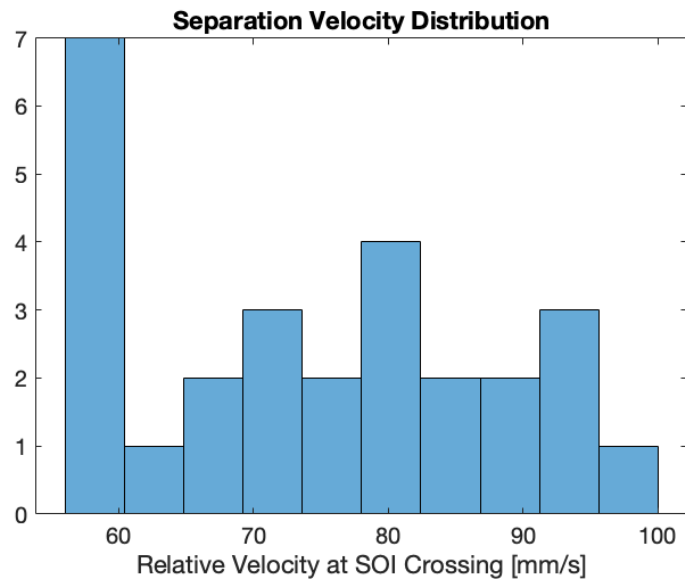


Figure 4.6: Magnitude of relative velocity as the secondary crosses the primary's sphere of influence for Moshup Simulations. The sphere of influence for the Moshup primary is 10370 meters.

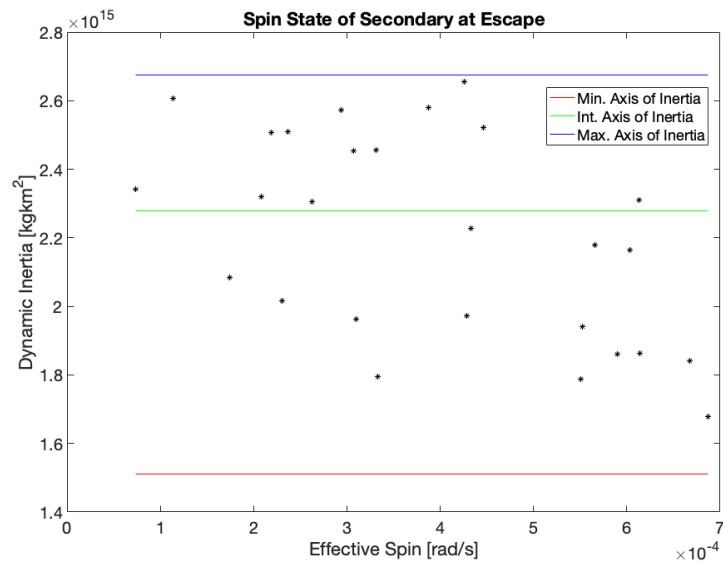


Figure 4.7: Complex spin state of the secondary at the moment of escape for Moshup Simulations.

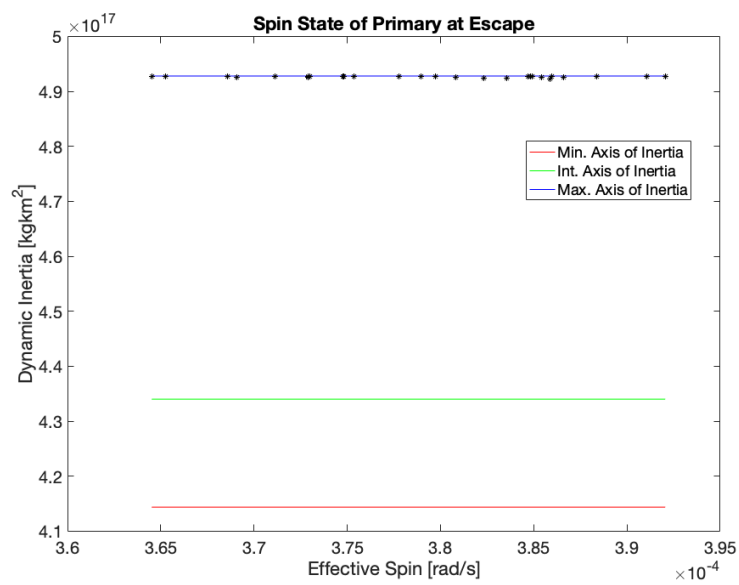


Figure 4.8: Complex spin state of the primary at the moment of secondary escape for Moshup Simulations.

4.3.4 Chaotic Orbital Capture

The small handful of captured secondaries remaining in orbit after a year of integration are likely statistically insignificant, but can still provide useful insight. Probing their secondary spin states after a year of integration, Fig. 4.9, reveals very excited systems likely not far from a disruptive event, based on the 2.2-2.3 hour spin barrier identified in past work by Pravec et al. 1998 and Sanchez and Scheeres 2014[33][64]. The horizontal bars indicate the values of the secondary's moments of inertia. The spin states are well distributed, but perturbed significantly from the relaxed spins about the minimum or maximum moments of inertia.

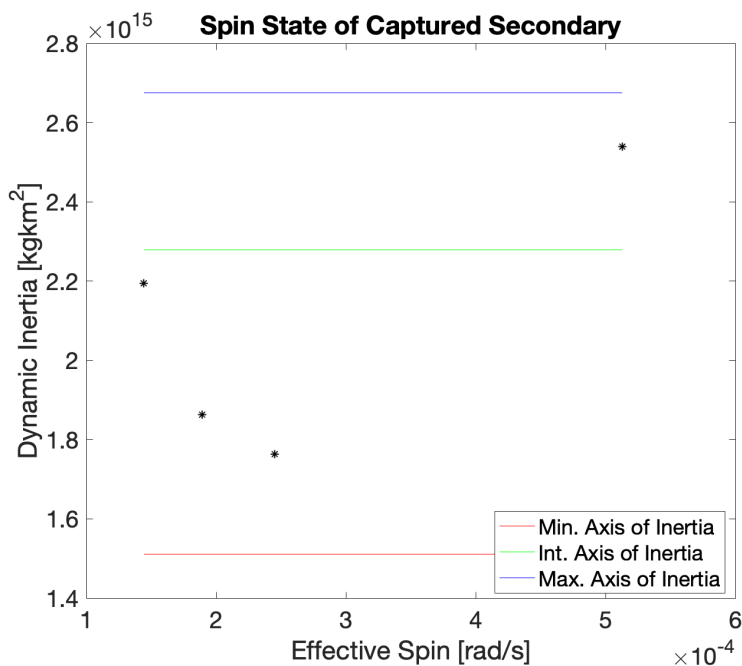


Figure 4.9: Complex spin state of the secondary in chaotically captured cases after one year of integration for Moshup Simulations.

4.4 1996 HW1

HW1 is used to represent two categories of NEA binary: fissioning contact binaries and high mass ratio binaries. The current geometry of HW1 is that of a contact binary, however we use a

fictitiously fissioned model for this study, Fig. 4.10.

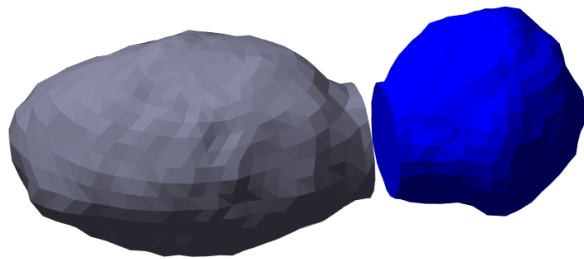


Figure 4.10: Split lobes of current 1996 HW1 geometry[7].

The current observed characteristics of HW1 are presented in Table 4.5[2][3]. The mass parameters are based on a constant density evaluation of the radar shape model assuming a density of $2.0\text{g}/\text{cm}^3$. Two values are provided for each ellipsoidal semi-axis, where the first value corresponds to the approximate ellipsoidal semi-axis of the primary and the second value corresponds to the secondary.

Table 4.5: Current observed 1996 HW1 based on observations by Magri et al. and Howell et al[2][3].

Spin Period [hr]	a [m]	b [m]	c [m]	Total Mass [kg]	Mass Fraction
$8.76 \pm 4 \times 10^{-5}$	1213 / 773	816 / 70.	761 / 692	8.68×10^{12}	0.33

The fictitiously fissioned shape models were developed in past work by Hirabayashi and Scheeres which derived the minimum strength of the asteroid for its current geometry [7]. While these shape models both have sharp angles at the neck where the fission is assumed to occur, the approximation of the mass distribution at the fourth order smooths this discontinuity because it does not converge identically to the shape. Table 4.6 identifies the uniform distribution of initial conditions used for the Monte Carlo simulations of the fission. We sample uniformly between the upper and lower perturbation bounds. The relative Euler angles define the relative orientation between the primary and secondary away from the current contact geometry. For the radial velocity and system spin rate two values for each entry are provided, where the first corresponds to the cohesion-less fission and the second corresponds to an additional set of simulations considered to

fission at a 4 hour spin period.

Table 4.6: Monte Carlo conditions for the HW1 analysis.

State	Equilibrium Value	Lower Pert. Bound	Upper Pert. Bound
Radial Separation [m]	1756.2	0.0	44
Radial Velocity [mm/s]	0.0	0.0	3.2 / 6.1
System Spin Rate [rad/s]	3.681×10^{-4} / 6.981×10^{-4}	0.0	1.85×10^{-5} / 3.49×10^{-5}
Rel. Euler Axis 1 [deg]	0.0	-30	30
Rel. Euler Axis 2 [deg]	0.0	-30	30
Rel. Euler Axis 3 [deg]	0.0	-30	30

For the simulations of HW1, the larger secondary in such a system significantly slows the transfer of angular momentum from the primary to the secondary, resulting in a much different evolutionary pathway. The statistical results from these simulations are presented in Table 4.7.

Table 4.7: Statistical results for HW1 formation simulations

Fate	Captured	Collision	Escape	Secondary Fission
#	114	59	2	0
%	65.1%	33.7%	1.1%	0%
Median Time	N/A	2.1 hr	146.0 dy	N/A

The most significant difference from the low mass ratio Moshup system is the lack of secondary fission and rarity of escape. Additionally we see that the rate of collision decreases slightly and the rate of chaotic capture increases significantly. While the rate of collision is likely dependent on the dynamical state, the rate of capture results from the slower angular momentum transfer prevents disruption of the system by escape or secondary fission. This agrees with the results of JS2011, whose longer integrations of high mass ratio binary evolution indicate a slower relaxation towards the outer stable doubly synchronous equilibrium on the order of 10^4 to 10^6 , depending on the mass distributions of the asteroids.

4.4.1 Recollision

While the collision rate for HW1 is relatively close to that of the Moshup system, the behavior is much different. In Fig. 4.11 we identify the location on the primary of impact and the surface velocity magnitude of the collision. The points are colored by the magnitude of the surface velocity at impact. All secondaries are initialized roughly resting on the flattened surface of the primary shape model.

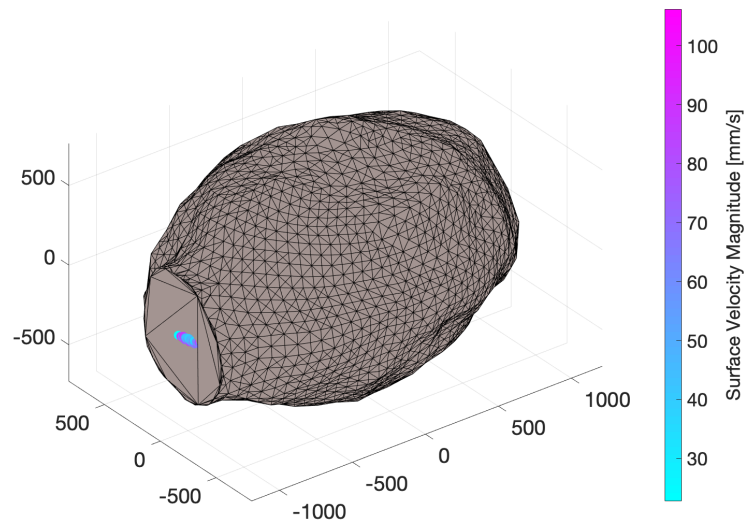


Figure 4.11: Location of impact locations for collision cases shown in the body fixed frame of the HW1 primary.

In this case we see that all of the collisions occur immediately after the fission, but still at relatively low surface velocities. This implies that the topology of the inner unstable equilibrium for HW1 is actually shifted further away from the body by higher order effects where many simulations are simply initialized within the topologically distorted collision barrier, rather than more slowly falling inwards as was the case for Moshup. Fig. 4.12 shows an example of the relative separation evolution for a collision case, showing a fast and direct fall inwards.

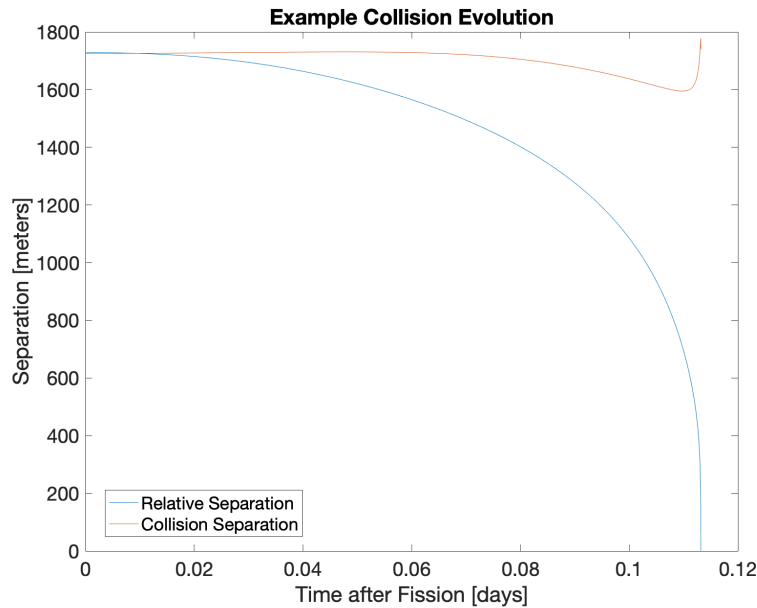


Figure 4.12: Evolution of the relative separation in a colliding case for HW1 simulations.

The collision separation, red, represents the the minimum distance between the two asteroid barycenters before they collide given their instantaneous relative attitude and position throughout an integration. The relative separation, blue, shows the actual separation between the two asteroid barycenters throughout the integration. Once the relative separation falls below the collision separation the asteroids are considered to have collided. For this case we see that the system is initialized just above the collision separation. After roughly 0.02 days the asteroids experience their initial collision. Within the post-processing this would be considered the time of collision. The evolution of the dynamics beyond this point shows a quick descent as opposed to a slow orbital decay over several periods.

Turning next to the distribution of the surface velocity at impact we see similarly slow velocities, Fig. 4.13. The velocities are provided in the secondary's orbit frame where the radial direction is from the primary's center of mass to that of the secondary, the cross-track direction is along the orbit in the direction of the orbital motion and the normal direction is along the

orbit normal. The surface velocity is the relative velocity between the surface of the primary and secondary at the moment of impact, accounting for relative spins and velocity.

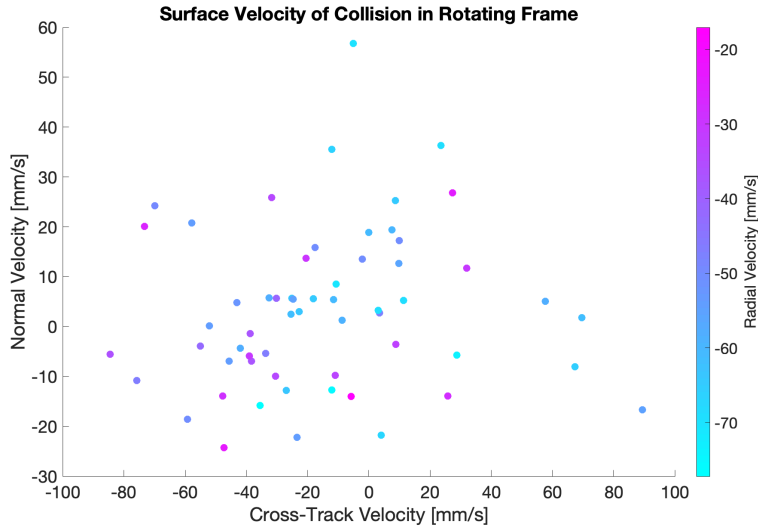


Figure 4.13: Instantaneous surface velocities of colliding secondaries at the moment of impact for HW1 simulations.

However the radial velocity range is much larger in magnitude than that of Moshup and does not come nearly as close to 0. This results from the more immediate collisions seen for this case, likely due to the higher dimensionality morphing of the topology of the inner equilibrium barrier to collision.

4.4.2 Escape

Although there are only two escaping cases, likely outliers, it is still of interest to investigate their states at the moment of escape. We provide the complex spin state of the primary and secondary, Fig. 4.14 and 4.15, and the relative velocities at escape, Fig. 4.16.

We see that the spin state of the primary is much more excited at the moment of escape than for the case of Moshup, while the behavior of the secondary is fairly similar. The excited primary

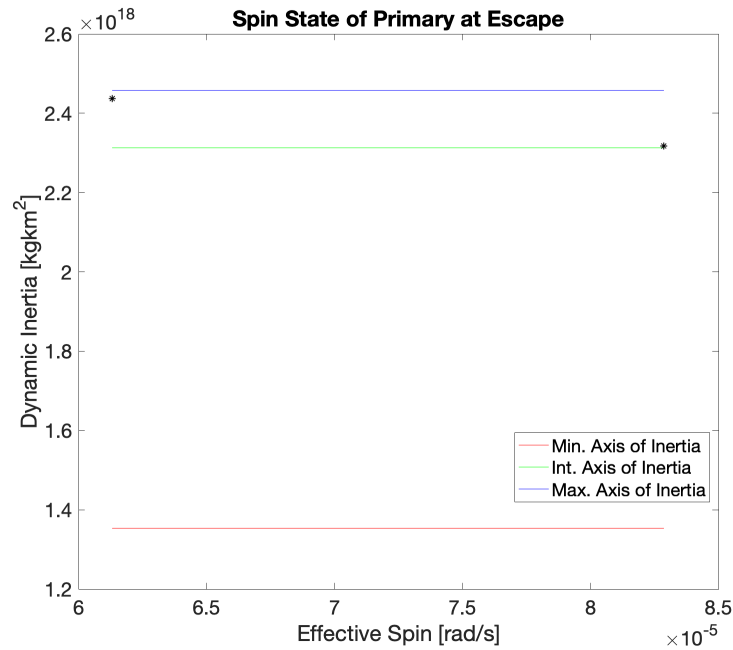


Figure 4.14: Complex spin state of the primary at the moment of secondary escape for HW1 simulations.

spin state result partially from its elongated shape being more susceptible to gravity torques from the secondary but also is due to the secondary large mass. This may imply that for high mass ratio asteroid pairs the spin states will be particularly excited.

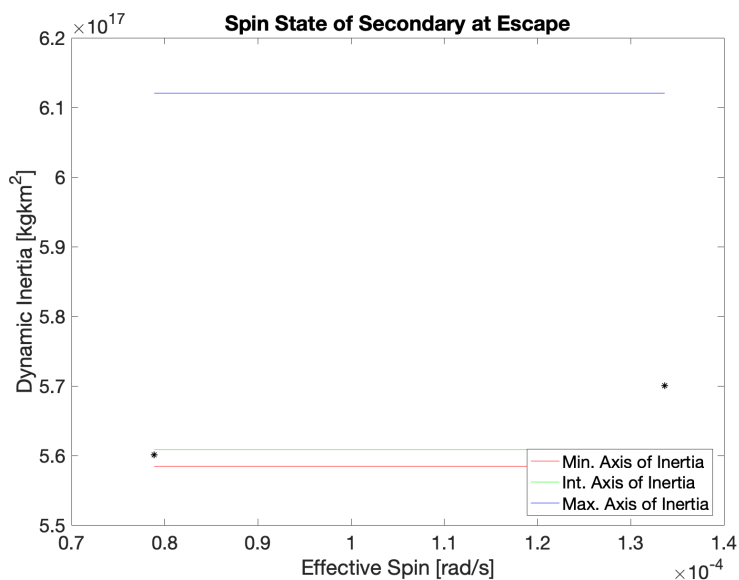


Figure 4.15: Complex spin state of the secondary at the moment of secondary escape for HW1 simulations.

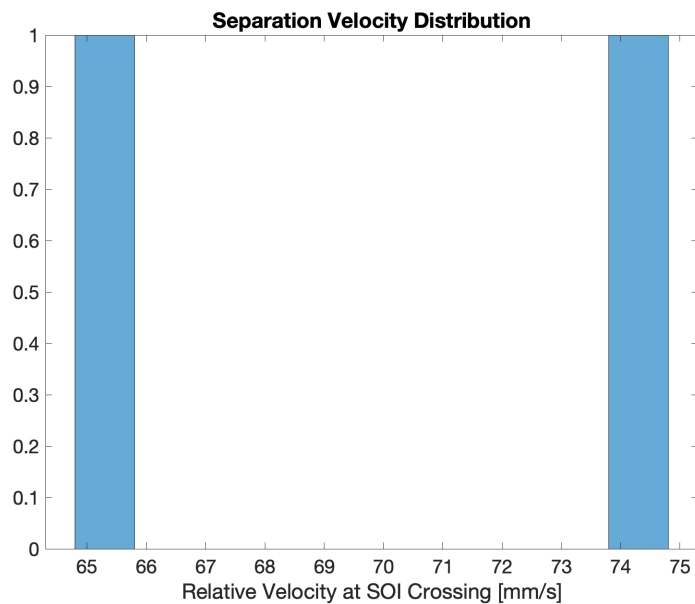


Figure 4.16: Magnitude of relative velocity as the secondary crosses the primary's sphere of influence for HW1 simulations. The sphere of influence for the HW1 primary is 28951 meters.

In addition to the particular details of the asteroid dynamics at the time of escape, HW1 provides a good example to explore the angular momentum transfer process which excites binary orbits from captured to escape trajectories. The process of angular momentum transfer from binary asteroid spin states into the orbital states has been studied extensively by Scheeres, Harris, Walsh and others[66][67][13][68]. The essential idea of the process is that as the secondary moves towards periapsis its orbital motion couples with the primary's spin and the primary's shape is able to torque the orbit of the secondary, transferring the primary's the angular momentum and energy into the mutual orbit. In Fig. 4.17 we identify this interaction in a simulation of HW1 which occurs just before the secondary escapes the system. The system is shown in the primary's principal frame with its angular momentum oriented out of the page.

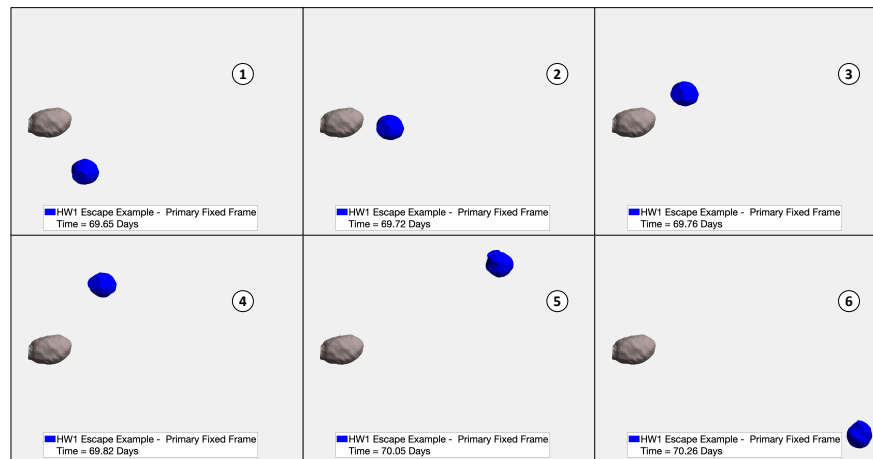


Figure 4.17: Example of angular momentum transfer in the HW1 system.

The six frames show the secondary moving through periapsis and gaining angular momentum from the primary's spin and shape before moving towards an escaping trajectory. As the secondary approaches periapsis in, frame 1 to 2, it is moving with a lower angular velocity than the primary's spin. Its periapsis occurs nearly in exact alignment with the primary's major axis, maximizing the gravitational torque it experiences. After periapsis passage the secondary has been orbitally torqued such that its angular velocity surpasses that of the primary. Shortly afterwards the secondary is

moving along a trajectory to escape the system.

4.4.3 Chaotic Orbital Capture

The abundance of chaotically captured secondaries at the end of a year of integration is in stark contrast to the low mass ratio Moshup results. As previously described the higher mass ratio of HW1 prevents the large flow of angular momentum from the primary to the secondary. Instead the bodies exchange angular momentum between each other and the orbital state more freely. While this prevents either body from reaching a critical spin rate for fission regardless of the fission model used, it does lead to a much more excited spin state of each body and a rapidly changing mutual orbit. Fig. 4.18 and 4.19 provide the complex spin state for the chaotically captured primaries and secondaries after a year of integration.

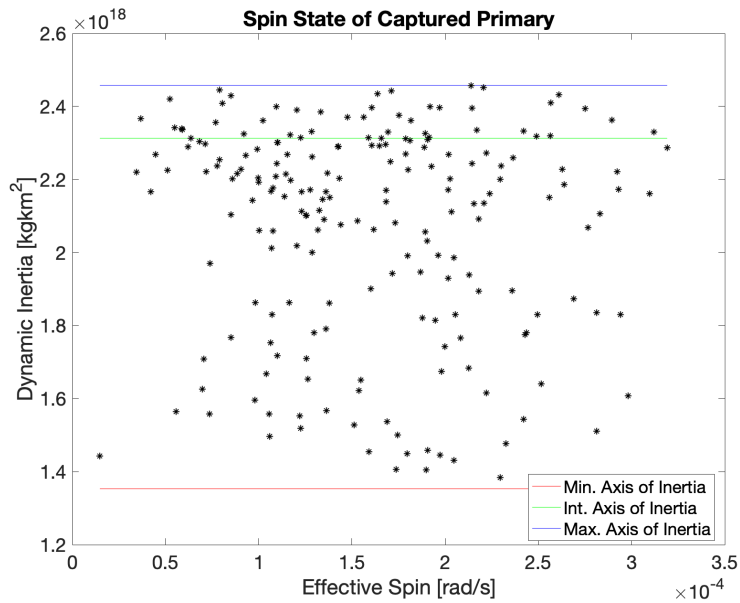


Figure 4.18: Complex spin state of the primary in chaotically captured cases after one year of integration for HW1 simulations.

The excited spin states of both bodies are clear, and the excitement of the primary towards the tumbling state is extreme when compared to the low mass ratio cases. Because no secondary

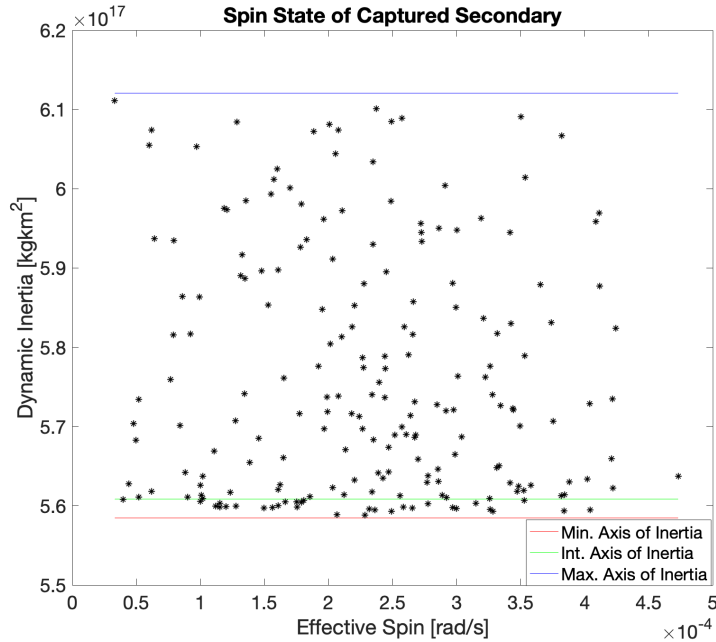


Figure 4.19: Complex spin state of the secondary in chaotically captured cases after one year of integration for HW1 simulations.

fission occurs for these cases, even when the simulations are extended for an additional year of integration, slower methods of energy dissipation dominate. Over these longer periods of time, the planar second-order dynamics modelled in JS2011 likely dominate and the systems would slowly relax towards the doubly synchronous state, as seen in JS2011[30].

4.4.4 Effects of Increasing Fission Spin Rate

We further explore the effect of the initial fission spin rate and potential for cohesive fission to change the end state of the binary's evolution. To do this we run an additional set of simulations for HW1 with a fission spin rate of 4 hours, as opposed to the previous 4.74 hours. Other than the spin rate all other states are initialized with the same values as presented in Table 4.6 above. We do not recompute the unstable equilibrium in order to isolate the potential effects of cohesion under the same fission geometry. Table 4.8 provides the statistics for this faster spinning fission case.

Table 4.8: Statistical results for 4 hour fission period HW1 formation simulations

Fate	Captured	Collision	Escape	Secondary Fission
#	0	11	137	0
%	0%	7.4%	92.6%	0%
Median Time	N/A	< 1 hr	6.6 dy	N/A

The increase in the initial energy and angular momentum at fission results in a much faster and nearly inevitable disruption of the system, with 93% of secondaries escaping in a median time of 6.6 days. All other systems collide with the primary. This suggests that, at least for high mass ratio binaries, the initial fission must be relatively gentle and not dominated by cohesive forces.

4.5 2000 DP107

Previous studies of rotational asteroid fission and binary pairs predict equatorial craters to be a result of the inset mass ejection fission model and identify potential craters on binary pair shape models[41][69]. Both NASA’s OSIRIS-REx mission and JAXA’s Hayabusa 2 identify this type of topography on their target asteroids, potentially suggesting the fission process is more common in the NEA population than previously thought[70][71]. DP107 thus provides a convenient example to test the feasibility of the equatorial crater as a topographic marker for this model of fission by testing formation rates of binaries and asteroid pairs. Radar shape models of DP107 identify an equatorial crater on the primary similar in size to the secondary asteroid[4]. The current state based on these measurements is provided in Table 4.9.

Table 4.9: Current observed 2000 DP107 States based on Naidu et al while the mass parameters are based on a constant density evaluation of the radar shape model assuming the measured density of 1.38 g/cm^3 [4].

Orbit Period [hr]	SMA [m]	Ecc.	Total Mass [kg]	Mass Fraction
42.48 ± 0.48	2659 ± 80	0.019 ± 0.01	4.8430×10^{11}	0.0469

To approximate mass inset fission we seed the unstable equilibrium solver with the secondary asteroid placed within the current crater, illustrated in Fig. 4.20. The view is isometric, looking 10 degrees down onto the orbit plane. The secondary is inset within the crater of the primary but

a few meters from the surface.

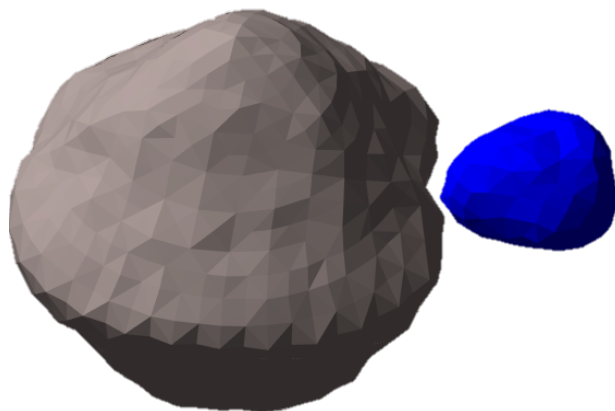


Figure 4.20: Relative geometry of the initial geometry at fission for DP107.

Because the secondary is placed within the crater and not principally aligned, the equilibrium solver identifies a facsimile to the unstable equilibrium which is essentially an orbit instantaneously near a doubly synchronous states. The distribution of initial conditions sampled for the Monte Carlo is provided in Table 4.10.

Table 4.10: Monte Carlo conditions for the DP107 analysis.

State	Equilibrium Value	Lower Pert. Bound	Upper Pert. Bound
Radial Separation [m]	652.0	0.0	16
Radial Velocity [mm/s]	0.0	0.0	1.1
System Spin Rate [rad/s]	3.436×10^{-4}	0.0	1.77×10^{-5}
Rel. Euler Axis 1 [deg]	0.0	-30	30
Rel. Euler Axis 2 [deg]	0.0	-30	30
Rel. Euler Axis 3 [deg]	0.0	-30	30

Because DP107 was initialized with the secondary set in the primary's equatorial crate and not principally aligned, comparison of the Monte Carlo results with Moshup is not simple. The statistics from the DP107 simulations are presented in Table 4.11. These results show all simulations colliding with the primary, suggesting extreme difficulty for the inset mass process of binary formation.

Table 4.11: Statistical results for DP107 formation simulations

Fate	Captured	Collision	Escape	Secondary Fission
#	0	150	0	0
%	0%	100%	0%	0%
Median Time	N/A	0.2 dy	N/A	N/A

4.5.1 Recollision

Unfortunately for the case of DP107 we see that all secondaries collide for the nominal Monte Carlo perturbations. The likely cause of this is the placement of the secondary within the recess of the crater such that from the point of fission it does not have the outward velocity or energy to quickly move out of the crater without hitting the crater's edge. The points are colored by the magnitude of the surface velocity at impact. All secondary's are initialized within the crater seen on the right side of the equator in this view.

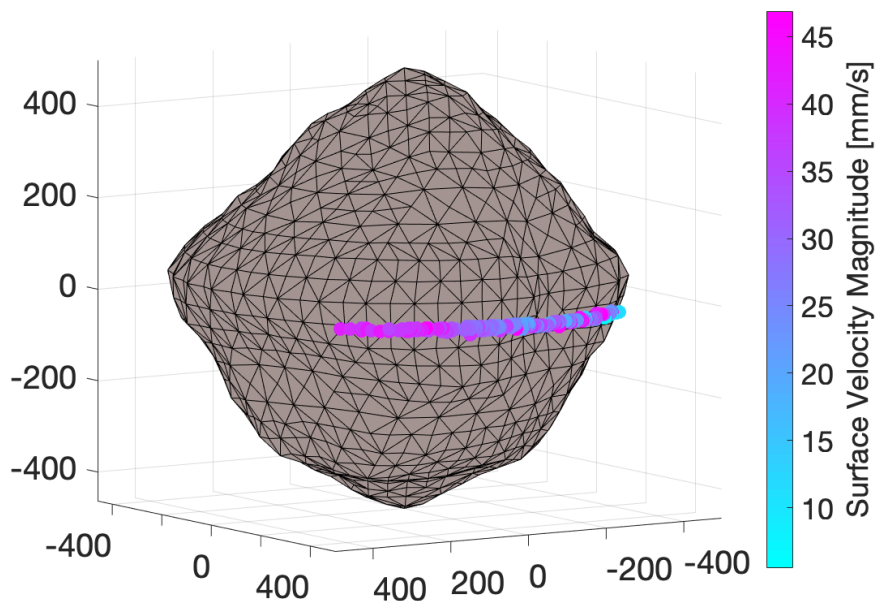


Figure 4.21: Location of impact locations for collision cases shown in the body fixed frame of the DP107 primary.

Looking at the impact locations, Fig. 4.21, we can see that this explanation describes a large

fraction of the collisions. For a subset of cases the secondary is able to leave the confines of the crater, but still recollide shortly after. These cases likely fission onto a highly elliptical orbit, with periapsis below the asteroid surface, and begin their descent back towards the primary before their orbits have been sufficiently circularized.

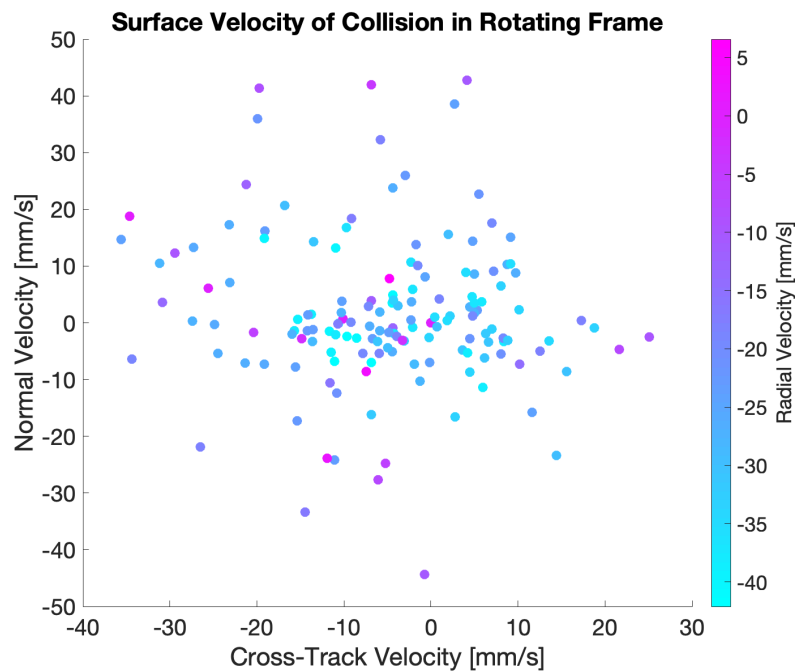


Figure 4.22: Instantaneous surface velocities of colliding secondaries at the moment of impact.

The distribution of the surface velocity directions, Fig. 4.22, appears to further support this explanation. Firstly, it shows that a majority of the collisions occur at low, and sometimes outward, radial velocities. These points correspond the secondaries which fail to escape the crater, colliding within the crater surface or edge mostly with cross-track and normal-velocity on their way out of the crater. Comparing the larger radial velocity impacts we see that the velocity magnitude in the other directions is much smaller, implying a more direct collision than what was seen for Moshup or HW1.

4.5.2 Further Analysis of Secondary Fission

An argument can be made for the DP107 cases that the secondary may have sufficient energy to fission and launch one portion of the body into the orbit under the bi-lobed secondary fission model. This argument can be taken to the extreme by applying the model with equally sized lobes, equivalent to a mass fraction of 0.5. Unfortunately, as shown in Table 4.12, the majority of the recollisions occur so quickly that only a single secondary experiences fission before returning to the surface of the primary.

Table 4.12: Statistical results for DP107 formation simulations with the bi-lobed secondary fission model and a secondary mass fraction of 0.5

Fate	Captured	Collision	Escape	Secondary Fission
#	0	149	0	1
%	0%	99.3%	0%	0.7%
Median Time	N/A	0.2 dy	N/A	0.1 dy

Further exploring the results of the bi-lobed secondary fission model for DP107 we can identify the bounds of the secondary mass-fraction which enable secondary fission to occur before recollision. The identified condition is

$$0.107 \leq \nu_s \leq 0.816 \quad (4.7)$$

This tells us that such a secondary fission requires that the body be composed of relatively large mass elements.

4.5.3 Higher Energy Formation

Based on the results of this initial set of simulations it is clear that for the DP107 secondary to successfully fission from the equatorial crater, the initial conditions must be more energetic. This would allow the secondary to escape the crater and enter a captured orbit. We use two approaches to try and explore the DP107 formation conditions. The first is to assume cohesion plays a more significant role in the fission as was attempted with HW1 in 4.4.4. In this case the Monte Carlo

conditions and perturbation bounds are maintained, but the system initial spin period is sped up from 5.08 hours to 3.85 hours. The second approach is to explore the dynamical space more widely by increasing the perturbation bounds while maintaining the same initial conditions. The perturbation bounds for this wider Monte Carlo are provided in Table 4.13.

Table 4.13: Wide Monte Carlo conditions for the DP107 analysis. We sample uniformly between the upper and lower perturbation bounds.

State	Equilibrium Value	Lower Pert. Bound	Upper Pert. Bound
Radial Separation [m]	652.0	0.0	160
Radial Velocity [mm/s]	0.0	0.0	45.3
System Spin Rate [rad/s]	3.436×10^{-4}	0.0	1.37×10^{-4}
Rel. Euler Axis 1 [deg]	0.0	-30	30
Rel. Euler Axis 2 [deg]	0.0	-30	30
Rel. Euler Axis 3 [deg]	0.0	-30	30

The results of these Monte Carlo sets are best compared using both the cohesive and bilobed secondary fission models. In Table 4.14 the statistical results for both Monte Carlo sets post-processed with both secondary fission models are provided.

Table 4.14: Comparison of secondary fission results for faster spin rate and wider perturbation Monte Carlo analyses of DP107.

Model	Secondary Mass Fraction	Captured	Collision	Escape	Secondary Fission
DP107 with Initial Spin Period of 3.85 hours					
COH	N/A	0	91	58	1 (4.92 dy)
BL	1×10^{-7}	0	86	58	6 (2.64 dy)
BL	1×10^{-5}	0	84	58	8 (2.377 dy)
BL	1×10^{-3}	0	70	56	24 (2.137 dy)
BL	0.5	0	0	0	150 (0.03 dy)
DP107 with Wider Monte Carlo Perturbation Bounds					
COH	N/A	0	146	4	0
BL	1×10^{-7}	0	145	4	1 (1.02 dy)
BL	1×10^{-5}	0	145	4	1(1.00 dy)
BL	1×10^{-3}	0	148	4	8 (0.827 dy)
BL	0.5	0	56	0	94 (0.05 dy)

The broad conclusion to be made from these results is that in both cases the majority of

secondaries recollide or escape unless the secondary is composed of fairly large mass elements. In the case that the secondary does fission it occurs very quickly, potentially in less than an hour. This suggests that formation of binaries with equatorial craters like DP107, assuming the secondary fission pathway described in JS2011, is only likely given a particular case of rubble pile asteroid with sufficiently large boulders or other mass elements. Looking more closely at the 3.85 hour initial spin period case the dynamics appear to dictate that a similar number of secondaries either collide or escape, ignoring secondary fission of these cases. There is a delicate balance based on the initial spin period that leads to this; if the initial spin period is reduced to 4 hours the secondaries all recollide and if the spin period is increased to 3.75 hours the secondaries all escape. This presents an interesting comparison with the 2.2 hour spin barrier traditionally observed in the NEA population; suggesting that systems fissioning near this barrier would be more likely to form asteroid pairs than binary systems. In the case of wider Monte Carlo perturbation bounds the vast majority of secondaries recollide with a small subset having the potential to escape due to the relatively large range of velocity perturbations. One possible explanation for the difficulty identifying a formation pathway for DP107 is the initialization of the secondary near the crater as opposed to being closer to the unstable equilibrium. This would reinforce the importance of this state as a boundary or gateway for binary formation. As such it may have implications for the mass distribution of binaries with equatorial craters, assuming the crater was the original site of the secondary before fission.

4.6 Broad Comparison to Past Work

Many past binary formation and evolution studies have relied on a range of assumptions in order to broadly study the system dynamics or particular processes. Within this work we are able to apply computationally efficient high fidelity dynamics models in order to lift these assumptions and more rigorously test the theories and conclusions presented in past work. In broad strokes, we reconfirm many past findings. We find that low mass ratio binaries like Moshup and DP107 tend towards disruption and require a fast acting means of energy dissipation, such as the secondary

fission process proposed in JS2011, in order to relax into their current observed orbital states. Likewise the slow angular momentum transfer available to high mass ratio binaries prevents excitement to secondary fission, instead suggesting a slower evolutionary pathway as described by Jacobson and Scheeres. We additionally find explicit examples of the angular momentum transfer from an elongated primary into the mutual orbit of a binary leading to escape in the HW1 simulations; similar behaviors occur for Moshup and DP107 although not as easily illustrated[68]. In studying the formation of binaries via inset mass ejection we identify the difficulty of this process without the inclusion of secondary fission. Likely this can be argued to be a result of the dynamical structure of the F2BP away from the unstable equilibrium. In general we show that the inclusion of higher order gravity terms and non-planar dynamics slows the evolutionary processes at play but does not significantly alter the formation of binaries. However, these more complex dynamics do topologically morph the zero velocity curves near the unstable equilibrium as discussed in Sec. 3.3. This complicates its behavior as a barrier to fission and introducing the possibility of low velocity recollision with the primary. Given the relatively high rate of recollision we see it would be expected that binaries or contact binaries may have small craters or impacts from these events, but a better understand of these interactions would be necessary to identify the exact observable markers.

In detailed comparison with the JS2011 we identify slower formation processes and recollision as a new form of potential disruption. For low mass ratio binaries, like Moshup, we see that both escape and secondary fission occur on a much slower time scale, albeit with the same number of cases. As a result of the recollision events possible in our model we also see a significantly decreased number of escaping secondaries, with the number of chaotic capture and secondary fission remaining roughly the same. This suggests potentially fewer asteroid pairs resulting from this type of binary fission than may have been expected by Jacobson and Scheeres. For the high mass binaries, like HW1, Jacobson and Scheeres see most secondaries remaining chaotically captured and slowly relaxing towards the doubly synchronous equilibrium. Our study of HW1 seems to support this with the caveat of potential recollision. While our study of DP107 deviates from the Jacobson and Scheeres study it does support the need for secondary fission as a means to dissipate

the energy of the secondary in order to form a stable low mass ratio binary.

In our study of secondary fission two models can be tested against one another, one assuming only cohesive forces while the other focused on the gravitational effects of the primary on the components making up the secondary. In the case of the Moshup system we show that regardless of the secondary fission model employed and the size of the fissioning particles, between one and two thirds of systems experience secondary fission. While the ejection of meter sized objects from the secondary is not likely to alter the secondary's orbit as significantly as larger masses, realistic secondaries are likely to be more complex than the bi-lobed model used. This suggests that secondary fission remains a likely pathway for the evolution of low mass ratio binaries, while also indicating that a more complex and rigorous study be performed. The difficulty of stabilizing a binary like DP107 before recollision without secondary fission further supports this argument, although the system is a unique subset of binary fission. In comparison with previous work by Walsh et al., where the secondary asteroids are assumed to be rubble piles potentially containing large components with radii in the 10's of meters, our secondary fission study of Moshup, Table 4.4, suggests these binaries are likely to experience secondary fission[72].

4.7 Summary

Building on past work by Scheeres, Jacobson, Walsh, and others we are able to apply improved binary asteroid simulation tools to further analyze the formation and evolution of these systems. Moshup, 1996 HW1 and 2000 DP107 are used as example systems to capture the particular evolutionary pathways identified in past studies. For each of these systems a Monte Carlo analysis of their conditions at formation is performed to understand the dynamics at play. We find that for low mass ratio binaries, like Moshup and DP107, disruption, via escape or re-collision, is the most likely outcome unless some form of secondary fission is allowed to occur. For high mass ratio binaries, like HW1, our simulations show short term escape to be an unlikely outcome given standard models of contact binary fission; instead suggesting a slower evolution towards a stable doubly synchronous state. In our analysis of these three systems we also identify topological effects

of higher order gravity terms and out of plane motion on the inner unstable equilibrium of the F2BP. Previously this equilibrium was considered a barrier to re-collision, however we find that the increased dimensionality of the dynamics warps the topology of the dynamical structure such that re-collision is able to occur. While the re-collision case is new within the framework of our analysis, it does not appear to significantly change the evolutionary pathways identified in previous studies.

Chapter 5

Remote Estimation of Doubly Synchronous Binary Asteroid Mass Parameters

In this chapter we explore the feasibility of binary asteroid mass parameter estimation based on remote observations. In Sec. 3.2 we identified the eight dynamical families or oscillations about the outer stable doubly synchronous equilibrium, hereto after referred to as the doubly synchronous equilibrium. We leverage this analysis to understand the observability of the mass parameters based on the sensitivity of the dynamics matrix and associated eigenvalues to the mass parameters. We begin with a numerical study of the planar problem wherein we vary the mass parameters and identify the numerical change in the linearized periods of the dynamical families. Next, we linearize the dynamics matrix with respect to the mass parameters, allowing for the computation of sensitivity of the linearized dynamical family frequencies with respect to the mass parameters. From here, a prototype estimation approach is developed for the planar problem using a differential corrector. As this approach is under-constrained, it is expanded to the nonplanar problem and used to analyze the estimation of the mass parameters. Finally, we explore the feasibility for near-spherical binaries, such as Pluto-Charon, where many of the dynamical families are not feasibly observable.

5.1 Mass Parameter Estimation in the Planar Problem

The initial estimation analysis is performed for the planar problem as this is the simplest form of the dynamics. Before employing an analytical approach, we perform a numerical analysis of the sensitivity of the fundamental frequencies to the mass parameters. Using this approach we

are able to identify specific trends in the dynamics associated with particular mass parameters. Additionally, the numerical analysis provides a rough approximation of the how sensitive the dynamics are to the mass parameters. Once we can ascertain the trends present in the system, we derive an analytical sensitivity of the fundamental frequencies, essentially the eigenvalues, to the mass parameters. Given the analytical model we can implement gradient descent estimation of the mass parameters from simulated measurements of the fundamental frequencies. While we find that the planar problem is under-constrained for estimation, it provides a prototype for the nonplanar implementation in the following section.

5.1.1 Numerical Sensitivity of Dynamical Families to the Mass Parameters

To begin we numerically survey the dynamical families of the planar problem to explore their sensitivity to the mass parameters. In the linear form, the dynamical families each form an elliptic oscillation of arbitrary amplitude about their associated state with a unique linear period (Table 3.2). Of interest in the linear system is the influence of the mass parameters on the linear periods of each dynamical family. To explore this we evaluate the linear periods of the system as the density, volume and axes of each body are scaled, shown in Figs. 5.1-5.3.

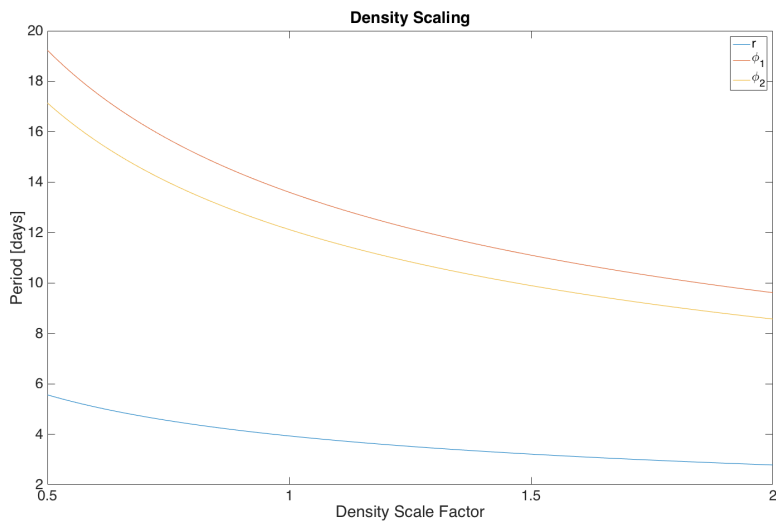


Figure 5.1: Behavior of planar doubly synchronous dynamical family linear periods as the density of the system is scaled.

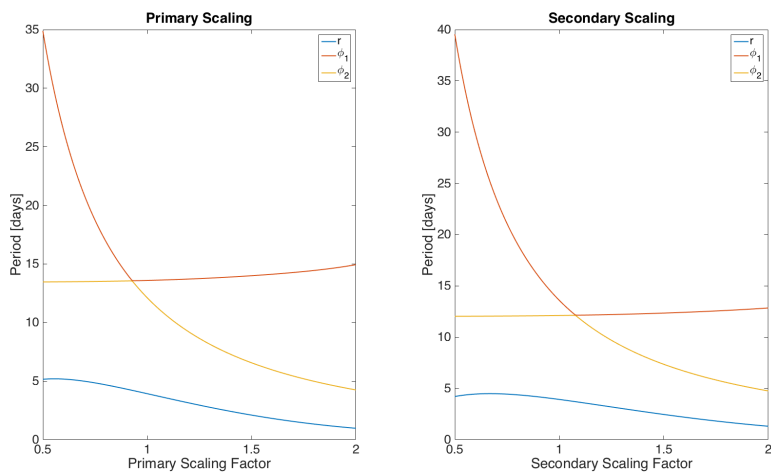


Figure 5.2: Behavior of planar doubly synchronous dynamical family linear periods as the volume of each body is scaled.

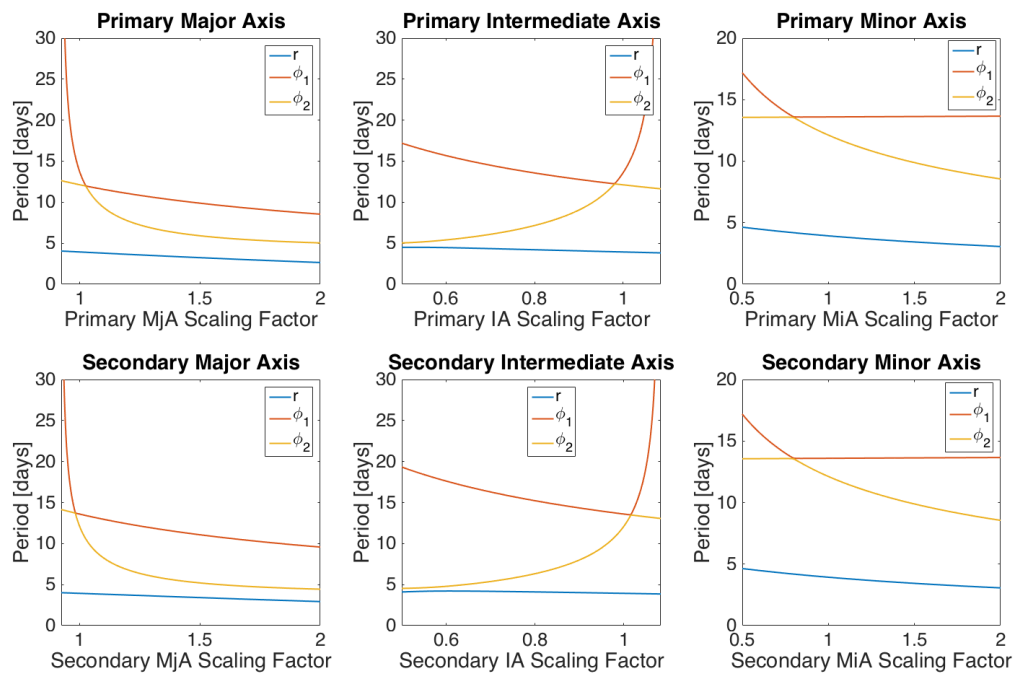


Figure 5.3: Behavior of planar doubly synchronous dynamical family linear periods as the length of each ellipsoid axis is scaled.

As the density is scaled upwards in Fig. 5.1, the periods each decrease in length. This implies a link between the system mass and the speed of its motion. The two phase angle periods also show very similar behavior. They have a roughly constant gap between their period values, a unique behavior associated with density scaling. In the case of volumetric, or mass ratio, scaling, Fig. 5.2, the separation and secondary phase angle periods show a muted response, while the behavior of the primary phase angle period shows a high sensitivity. In this figure, and the axis scaling figure, Fig. 5.3, there is an apparent switching of the primary and secondary phase angle periods near the unity scaling factor. This occurs when the secondary becomes more massive than the primary as the bodies are scaled, resulting in the gravitational dominance switching from the primary to the secondary. It is also of note that the scaling of the minor and intermediate axes is truncated near the scaling factor of one, this is done to avoid degeneration of the system by scaling the body to an oblate spheroidal shape. In the axial scaling analysis, Fig. 5.3, as each of the three axes is independently scaled, regardless of the body, a unique response occurs in the periods for each axis scaling. This implies unique behavior associated with each moment of inertia. While the analysis does not provide a definite method of determining the observability of the mass parameters, it does point towards unique behaviors of the system as different aspects of the mass distribution are scaled. We thus conclude that oscillations about the equilibrium likely will impact observations of binary systems to a significant degree.

5.1.2 Planar Estimation

To further understand the influence of the mass parameters on the fundamental frequencies, we derive their analytical sensitivity to the mass parameters under the planar and second-order assumptions. The periods of the fundamental frequencies are considered as idealized measurements made by observers. While direct observations of the dynamics would require extensive observations in close proximity, the frequencies more succinctly contain the same information content. Compared to direct observations of the dynamics, the fundamental frequencies provide a best case analysis. We approximate the sensitivity of the fundamental frequencies to the mass parameters as

$$\delta\vec{\Omega} = \frac{\partial\vec{\Omega}}{\partial\vec{T}} \bullet \delta\vec{T} \quad (5.1)$$

Where the vector $\vec{\Omega}$ is the set of fundamental frequencies derived from the eigen decomposition and the doubly synchronous orbit rate

$$\vec{\Omega} = \left[\vec{\Lambda}, \dot{\theta} \right], \text{ where } \vec{\Lambda} = \left[\beta_R, \beta_{\phi_1}, \beta_{\phi_2} \right] \quad (5.2)$$

with β_i representing the linearized dynamical family periods, P_{β_i} . The vector \vec{T} is the set of second order principal-axis inertia integrals

$$\vec{T} = \left[T_A^{2,0,0}, T_A^{0,2,0}, T_A^{0,0,2}, T_B^{2,0,0}, T_B^{0,2,0}, T_B^{0,0,2} \right] \quad (5.3)$$

It is assumed that knowledge about the mass of each body is gained from its relative separation and the reflex motion of the system about its center of mass. We define $\frac{\partial\vec{\Omega}}{\partial\vec{T}}$ as the sensitivity matrix, with which a least norm differential corrector can be used to estimate the mass parameters based on the observed frequencies.

The three frequencies arising from the dynamical family analysis are not analytically derived because of the complexity of the dynamics matrix and instead were computed numerically. Because of this, the partials of these frequencies could not be derived in closed form. Instead we leverage properties of the characteristic equation

$$|A - \lambda_i I| = 0 \quad (5.4)$$

$$0 = a_n \lambda_i^n + a_{n-1} \lambda_i^{n-1} + \dots + a_1 \lambda_i + a_0 \quad (5.5)$$

Where the coefficients a_n represent coefficients found from the determinant computation. Here the dynamics matrix, A , is identical to that in 3.2.1. We then take the partial of the characteristic equation in its polynomial form with respect each element j of the mass parameter vector, \vec{T} .

$$\begin{aligned} 0 = \frac{\partial a_n}{\partial \vec{T}(j)} \lambda_i^n + a_n \frac{\partial \lambda_i}{\partial \vec{T}(j)} \lambda_i^{n-1} + \frac{\partial a_{n-1}}{\partial \vec{T}(j)} \lambda_i^{n-1} + a_{n-1} \frac{\partial \lambda_i}{\partial \vec{T}(j)} \lambda_i^{n-2} + \dots \\ + \frac{\partial a_1}{\partial \vec{T}(j)} \lambda_i + a_1 \frac{\partial \lambda_i}{\partial \vec{T}(j)} \end{aligned} \quad (5.6)$$

We can then solve for the the partial $\frac{\partial \lambda_i}{\partial \vec{T}(j)}$ by substituting the numerically generated values of λ . Using the imaginary component of this partial, we can compute the matrix $\frac{\partial \vec{\beta}}{\partial \vec{T}}$ for use in the sensitivity matrix.

For the planar and second-order realization of the problem, the sensitivity matrix is rank deficient at rank 4 while having 6 columns from vector \vec{T} . As a result the differential corrector will find a solution lying in a two dimensional solution plane, defined by two nullspace vectors of the sensitivity matrix. Because the mass parameters of interest are the second order principal-axis inertia integrals, we can utilize the definition of the inertia ellipsoid

$$I_{zz} \leq I_{xx} + I_{yy} \quad (5.7)$$

$$I_{zz} \geq I_{yy} \geq I_{xx} \quad (5.8)$$

and thus constrain the valid area on the solution plane.

If such an estimation scheme were to be used, then other system observations and measurements would need to be gathered to find an exact solution. For instance flybys of either asteroid measuring the spherical harmonics or other mass tracking techniques. In the case of spherical harmonics measurements, constraints can be derived from the relationship[73]

$$I_{xx} - I_{yy} = -4Mr_s^2 C_{22} \quad (5.9)$$

$$I_{yy} - I_{zz} = r_s^2 (C_{20} - 2C_{22}) \quad (5.10)$$

Where r_s is an arbitrary scaling length. The projection of these constraint lines onto the solution plane provides the information necessary to reduce the estimated solution from a two dimensional space to a single point.

We illustrate the planar estimation approach in Fig. 5.4 by computing a set of initial mass parameter guesses with a Gaussian perturbation up to 5% from the “truth” mass parameter values. These are then projected onto the solution plane, shown as the red points, where the axes are the two nullspace vectors. We then project the inertia ellipsoid constraints onto the solution plane as

the sets of green and magenta lines, for the primary and secondary. Finally, the spherical harmonics constraints are projected onto the solution plane as the blue and black lines for the primary and red and cyan lines for the secondary. Because of the similarity in shape between Patroclus and the secondary Menoetius, the constraint lines appear to be overlapping in the figure. For a more dissimilar binary pair the spherical harmonics constraint lines would be more distinct. With all of these bounds and constraints in the figure, the different steps of this estimation process are clear; resulting in the final green truth at the crossing of the spherical harmonics constraints.

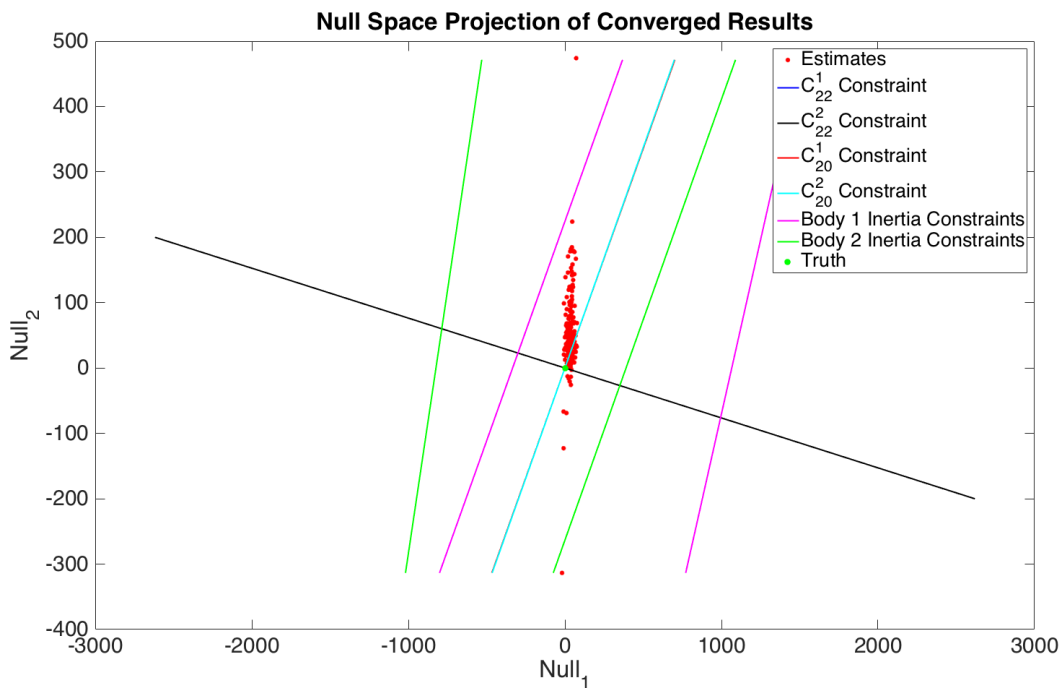


Figure 5.4: Projection of planar mass parameter estimates onto the solution nullspace plane.

5.2 Mass Parameter Estimation in the Nonplanar Problem

While the planar approach to remote mass parameter estimation turns out to be under-constrained, it does show the mathematical feasibility of such an approach. Thus the dynamics are expanded to the nonplanar problem, for which there are sufficient constraints between the dynamics and mass parameters. We begin the nonplanar approach by following the same general structure as for the planar problem. Mass parameters of interest, up to the second-order, are identified and the sensitivity of all eight nonplanar fundamental frequencies is derived. An example case is provided for the nominal 617 Patroclus system and the statistics of the estimate are analyzed. Next, the approach is analyzed for broader set of ellipsoidal dimensions to test the breadth of the mass parameter estimation.

5.2.1 Dynamical Oscillation Constrained Estimation

As with the planar case, for observations of the nonplanar system, we make the assumption that the reflex motion has been well characterized, providing constraints on the relative separation and the mass ratio, defined here as

$$\mu = \frac{M_2}{M_1 + M_2} \quad (5.11)$$

Thus the mass of each body can be evaluated based on an estimate of the total mass

$$M_T = M_1 + M_2 \quad (5.12)$$

As a result our estimated mass parameters can be the total mass and second order inertia integrals for both bodies.

$$\vec{T} = \left[M_T, T_A^{2,0,0}, T_A^{0,2,0}, T_A^{0,0,2}, T_B^{2,0,0}, T_B^{0,2,0}, T_B^{0,0,2} \right] \quad (5.13)$$

Given the increase in the number of system dynamical families the system frequency vector, $\vec{\Omega}$, for the nonplanar estimation becomes

$$\vec{\Omega} = \left[\beta_1, \beta_2, \beta_3, \beta_4, \beta_5, \beta_6, \beta_7, \dot{\theta} \right] \quad (5.14)$$

For this estimation we now have more observables than estimated values, thus the problem is over-constrained and can provide a full solution for the mass parameters from a theoretical standpoint.

The process of estimation will again apply Eq. 5.1, however the larger and more complex dynamics matrix for the nonplanar problem requires a new approach to computing the partials of the fundamental frequencies with respect to the mass parameters. Properties of the left and right eigenvectors are leveraged to compute the frequency partials. The left eigenvectors are defined as

$$\lambda_i \vec{v}_i = \mathbf{A}^T(\vec{T}) \vec{v}_i \quad (5.15)$$

while the right eigenvectors are defined as

$$\lambda_i \vec{u}_i = \mathbf{A}(\vec{T}) \vec{u}_i \quad (5.16)$$

where the i indicates the specific eigenvalue-vector pair. To begin the derivation, the partial of the right eigenvalue equation is taken with respect to the j th mass parameter

$$\frac{\partial \lambda_i}{\partial \vec{T}(j)} \vec{u}_i + \lambda_i \frac{\partial \vec{u}_i}{\partial \vec{T}(j)} = \frac{\partial \mathbf{A}}{\partial \vec{T}(j)} \vec{u}_i + \mathbf{A} \frac{\partial \vec{u}_i}{\partial \vec{T}(j)} \quad (5.17)$$

Left multiplying this partial by the transpose of the left eigenvectors, \vec{v}_i^T , the equation becomes

$$\frac{\partial \lambda_i}{\partial \vec{T}(j)} \vec{v}_i^T \vec{u}_i + \lambda_i \vec{v}_i^T \frac{\partial \vec{u}_i}{\partial \vec{T}(j)} = \vec{v}_i^T \frac{\partial \mathbf{A}}{\partial \vec{T}(j)} \vec{u}_i + \vec{v}_i^T \mathbf{A} \frac{\partial \vec{u}_i}{\partial \vec{T}(j)} \quad (5.18)$$

in which the $\frac{\partial \vec{u}_i}{\partial \vec{T}(j)}$ terms cancel based on the definition of the left eigenvector. Rearranging to solve for the partial of the frequency, β_i only

$$\frac{\partial \beta_i}{\partial \vec{T}(j)} = \mathbf{Im} \left(\frac{1}{\vec{v}_i^T \vec{u}_i} \vec{v}_i^T \frac{\partial \mathbf{A}}{\partial \vec{T}(j)} \vec{u}_i \right) \quad (5.19)$$

Thus the sensitivity matrix for the nonplanar problem can be computed element by element, iterating over this equation.

Given the complete solution generated by the estimation process, we can now analyze the uncertainties of the estimated mass parameters. The covariance and correlation of the mass parameters generated from this approach help to quantify the influence of the mass parameters on dynamical observations. To begin this analysis the covariance matrix for the mass parameters,

P_{TT} , is formulated by relating the pseudo-inverse of the sensitivity matrix and the observational covariance of the fundamental frequencies, $\mathbf{P}_{\Omega\Omega}$

$$\mathbf{P}_{TT} = \delta\vec{T}\delta\vec{T}^T = \left(\frac{\partial\vec{\Omega}^T}{\partial\vec{T}} \quad \frac{\partial\vec{\Omega}}{\partial\vec{T}} \right)^{-1} \frac{\partial\vec{\Omega}^T}{\partial\vec{T}} \bullet \mathbf{P}_{\Omega\Omega} \bullet \frac{\partial\vec{\Omega}}{\partial\vec{T}} \left(\frac{\partial\vec{\Omega}^T}{\partial\vec{T}} \quad \frac{\partial\vec{\Omega}}{\partial\vec{T}} \right)^{-1} \quad (5.20)$$

Because the frequencies are not an intuitive measurement the covariance of the fundamental frequencies is converted to the covariance of fundamental periods

$$\mathbf{P}_{\Omega\Omega} = \frac{\partial\vec{\Omega}}{\partial\vec{P}} \bullet \mathbf{P}_{PP} \bullet \frac{\partial\vec{\Omega}^T}{\partial\vec{P}} \quad (5.21)$$

This conversion is simply the derivative of the frequency and period relationship.

$$\frac{\partial\vec{\Omega}}{\partial\vec{P}} = \frac{\mathbf{diag}(\vec{\Omega})^2}{2\pi} \quad (5.22)$$

To define the covariance of the fundamental periods it is assumed that all periods would be independently measured using the same observation technique.

$$\mathbf{P}_{PP} = \sigma_P^2 \bullet \mathbf{I}_{8x8} \quad (5.23)$$

where there is a single period observational variance, σ_P , that is applied to the observations of each period. This observational variance can be considered to be a temporal resolution of the period measurements or the precision of each measurement.

5.2.2 An Idealized Estimation Method

This formulation of the covariance allows us to treat the sensitivity analysis approach as an idealized estimation approach. Here the observational variance, σ_P , would act as an observational accuracy requirement to constrain the mass parameter estimates to a specific accuracy level. In Table 5.1 this is leveraged to predict the observational variance necessary in order to gain 10% knowledge of each of the seven mass parameters of the 617 Patroclus system.

Table 5.1: Allowable observational variance of observations for 10% certainty of mass parameter estimates of the 617 Patroclus system.

Mass Parameter	Observational Accuracy Requirement [sec]
M_T	10584.0
T_A^{200}	25.3
T_A^{020}	25.3
T_A^{002}	25.3
T_B^{200}	15.0
T_B^{020}	15.0
T_B^{002}	15.0

To provide further insight, we compute the mass parameter variance for 617 Patroclus, given a 1 second observation variance

$$\bar{\sigma}_T = \begin{bmatrix} 9.45 \times 10^{-6} & 3.95 \times 10^{-3} & 3.94 \times 10^{-3} & 3.95 \times 10^{-3} & 6.64 \times 10^{-3} & 6.64 \times 10^{-3} & 6.64 \times 10^{-3} \end{bmatrix} \quad (5.24)$$

and the correlation matrix

$$\rho_{TT} = \begin{bmatrix} 1. & -0.27 & -0.27 & -0.27 & -0.64 & -0.64 & -0.64 \\ -0.27 & 1. & 0.99 & 0.99 & -0.55 & -0.55 & -0.55 \\ -0.27 & 0.99 & 1. & 0.99 & -0.55 & -0.55 & -0.55 \\ -0.27 & 0.99 & 0.99 & 1. & -0.55 & -0.55 & -0.55 \\ -0.64 & -0.55 & -0.55 & -0.55 & 1. & 0.99 & 0.99 \\ -0.64 & -0.55 & -0.55 & -0.55 & 0.99 & 1. & 0.99 \\ -0.64 & -0.55 & -0.55 & -0.55 & 0.99 & 0.99 & 1. \end{bmatrix} \quad (5.25)$$

The values for the variance and correlation in Eq. 5.24 and 5.25 are generated from the covariance matrix, which is not included for the sake of brevity and clarity. The bar used with variance values are normalized by the mass parameters corresponding to each element, such that they represent fractional covariances and variances

$$\bar{P}_{TT}(i, j) = \frac{P_{TT}(i, j)}{\bar{T}(i)\bar{T}(j)} \quad (5.26)$$

$$\bar{\sigma}_T(i) = \frac{\sigma_T(i)}{\bar{T}(i)} \quad (5.27)$$

5.2.3 Scaling with Ellipsoidal Shape

While these results show the mass parameters to be well estimated based on their variances, the observational requirement of 1 second variance on each frequency is highly restrictive. Likewise, the observational requirements to achieve 10% knowledge of the inertia integrals in table 5.1 further illustrates the accuracy of observations necessary for second order parameter measurements. In combination with the high correlation on the second order parameters, it becomes clear that without further constraints, via in-situ gravity measurement or other methods, such an estimation approach is not feasible even with these idealized observations.

To better understand the estimation of binary systems as a whole we now investigate the effects of scaling the mass parameters on the correlation and covariance matrices. Specifically we scale the the mass ratio and second order principal inertia integrals of Menoetius, the 617 Patroclus secondary. This is done as a means to explore the effects of mass ratio and differing asteroid mass distributions on the mass parameter estimation. We do not simultaneously scale the second order asteroid inertia integrals as this would merely scale the correlation and covariance as opposed to changing their structure. Likewise only the secondary is scaled as the system is nearly symmetric such that scaling either body will show the same sensitivity. The scaling of the inertia integrals is limited such that the asteroid remains a triaxial ellipsoid as opposed to an oblate spheroid; this is to avoid the degeneration of the dynamical families of the system caused by symmetric semi-axes.

For simplicity the second order principal axis inertia integrals of the secondary are referred to here as T_x , T_y , and T_z . The study performed scales the mass ratio by .1 and .55, T_x by .88 and .94, T_y by .7 and .85, and T_z by .01 and .51. The scaling floor for T_x and T_y is selected to avoid the the inertia integral dropping below the next smallest inertia integral which would cause a spherical degeneracy, thus T_z has no floor. Fig. 5.5 and 5.6 illustrate the covariance and correlation with the covariance elements colored by their log value and the correlation elements colored by their linear value from -1 to 1. The key point of interest in this case is whether the scaling of these mass parameters can lower the correlation between the each body's second order inertia integrals.

What both results show is that outside of the case of an extremely flattened body, the second order inertia integrals remain highly correlated. Even in the case of an extremely flattened body only the T_z correlation changes significantly while the T_x and T_y relationship remains very coupled. This implies that the dynamical effects of these unknown mass parameters can be significant for most shapes and configurations.

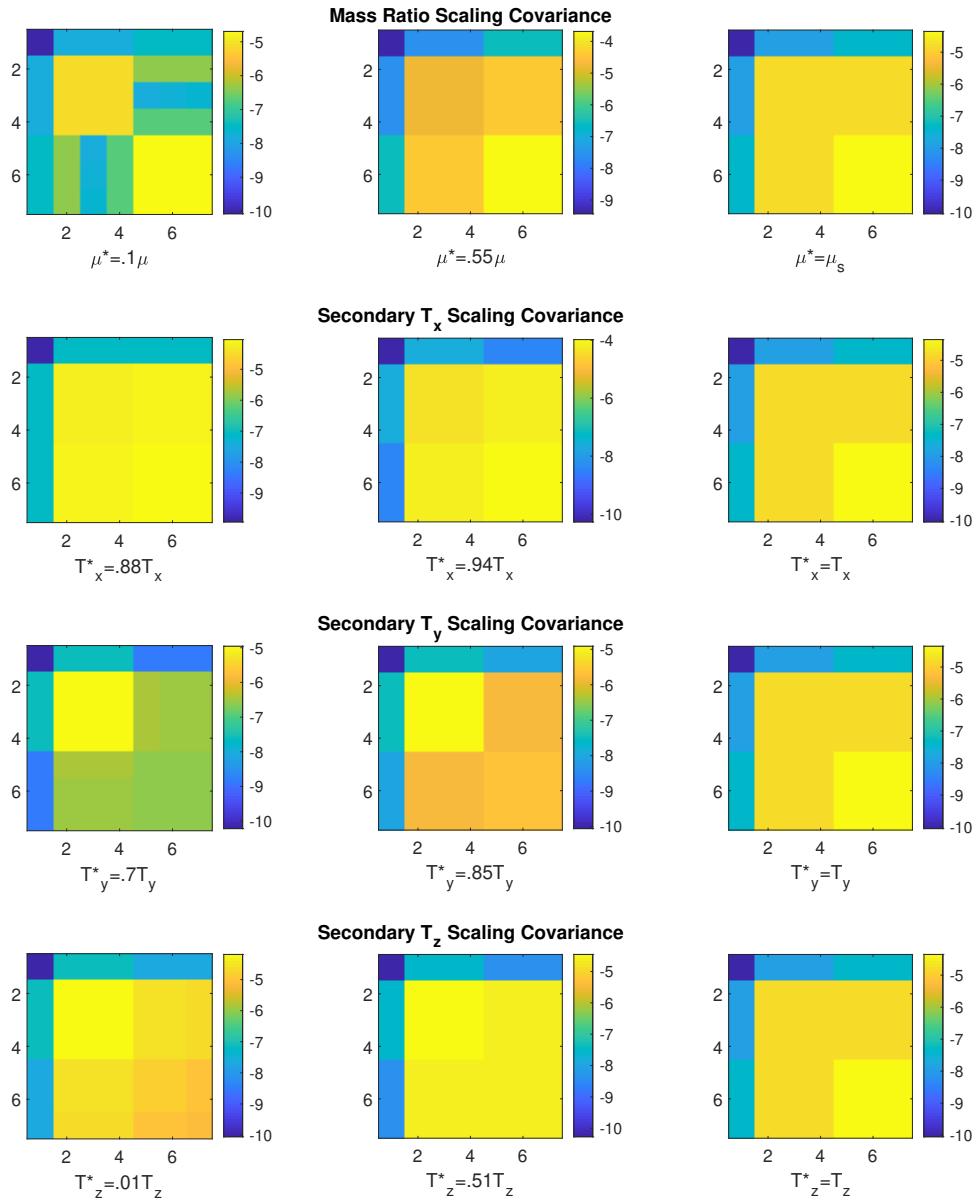


Figure 5.5: Effects of secondary mass parameter scaling on mass parameter covariance matrix with magnitude of matrix elements shown in log color.

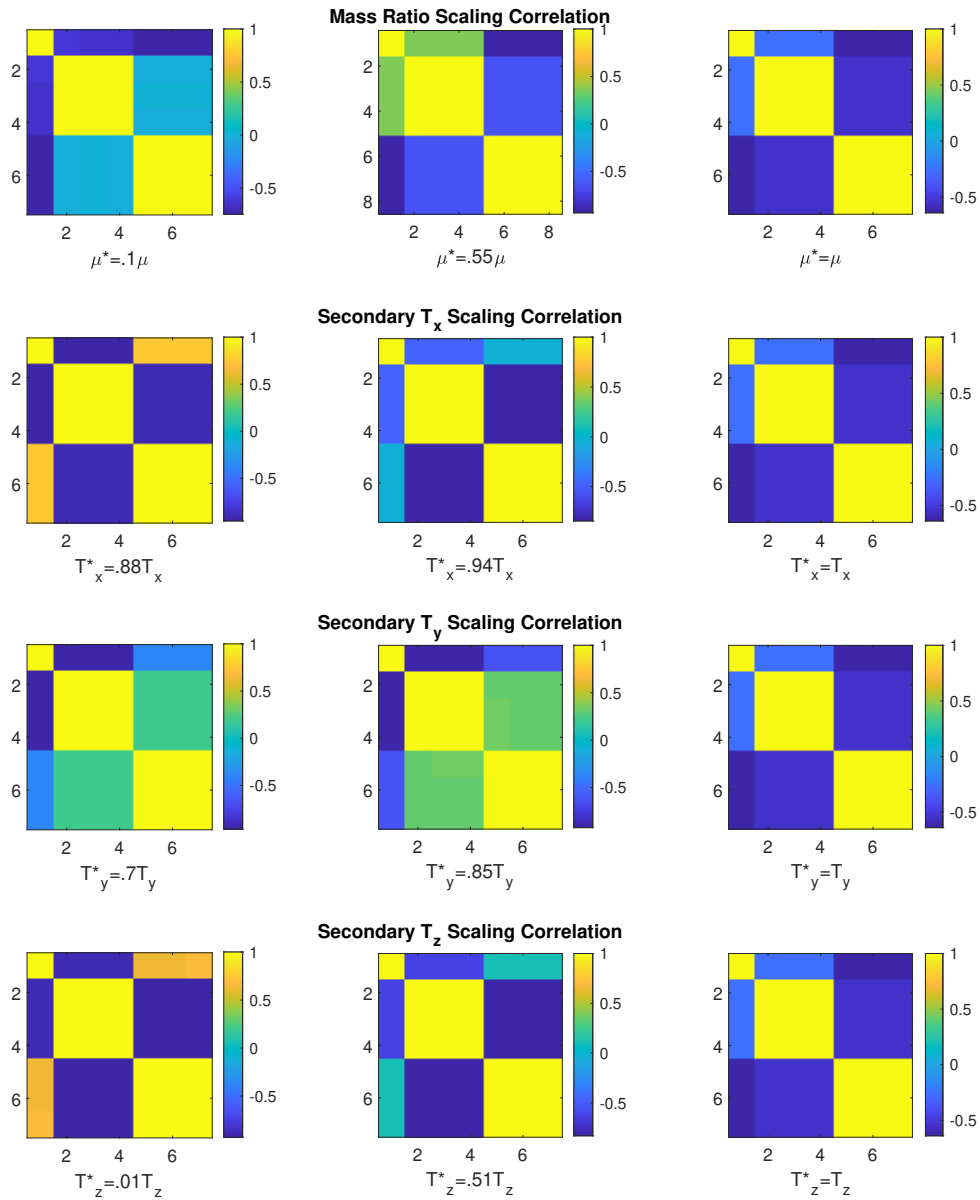


Figure 5.6: Effects of secondary mass parameter scaling on mass parameter correlation matrix with magnitude of matrix elements shown in linear color.

5.3 Near-Spherical Doubly Synchronous Systems

For a number of observed doubly synchronous binaries current shape knowledge is limited to a mean radius value or spherical shape estimate. However, for a binary system to remain in a stable doubly synchronous orbit, dynamical analysis has shown that the mass distribution of the bodies must be elongated such that the bodies mutual gravity torques enforce tidal locking. One result of this is that for a sphere-sphere doubly synchronous system four of the dynamical families become zero eigenvalues due to the lack of attitude interaction between the bodies, described in Table 5.2 for the Pluto-Charon system. In addition, for a nearly spherical body the effects of any elongation will be so low that the periods of these four dynamical families will be functionally immeasurable.

To better analyze these near spherical systems we perform a linearization about the spherical shape of the bodies using an elongation factor ϵ which perturbs the bodies as triaxial ellipsoids defined such that

$$abc = R^3 \quad (5.28)$$

$$a = R(1 + \epsilon), \quad b = R, \quad c = R(1 - \epsilon) \quad (5.29)$$

$$I_x = \frac{2MR^2}{5}(1 - \epsilon), \quad I_y = \frac{2MR^2}{5}, \quad I_z = \frac{2MR^2}{5}(1 + \epsilon) \quad (5.30)$$

where a , b , and c are the semi-axes.

Using these definitions of the near-spherical mass distributions we can linearize the dynamics as

$$\delta\vec{\Omega} = \left[\frac{\partial\vec{\Omega}}{\partial\vec{\epsilon}} \right]_{sphere} \delta\vec{\epsilon} \quad (5.31)$$

$$\delta\vec{\Omega} = \left[\frac{\partial\vec{\Omega}}{\partial\vec{T}} \frac{\partial\vec{T}}{\partial\vec{\epsilon}} \right]_{sphere} \delta\vec{\epsilon} \quad (5.32)$$

$$\frac{\partial \vec{T}}{\partial \vec{\epsilon}} = \begin{bmatrix} -\frac{2R_P^2}{5} & 0 \\ 0 & 0 \\ 0 & \frac{2R_P^2}{5} \\ -\frac{2R_C^2}{5} & 0 \\ 0 & 0 \\ 0 & \frac{2R_C^2}{5} \end{bmatrix} \quad (5.33)$$

where $\vec{\Omega}$ represents the remaining system frequencies, \vec{T} again represents the vector of only the second-order principal-axis inertia integrals, and $\vec{\epsilon}$ represents the elongation factors applied to the primary and secondary body independently. It is of note that this linearization assumes that the equilibrium separation remains constant as the bodies are elongated. This means that the equilibrium orbit rate must scale as the bodies are elongated while maintaining the observed separation. This effect on the orbit rate is analogous to the effect on the other three periods of the elongation, however they are not as simply expressed as the orbit rate, whose change can be directly computed. By analyzing the linearized effects of the deformation on the four remaining periods and observing the behavior of these measurable dynamical family periods, we provide a different approach to understand the effects of the the mass distributions of near-spherical systems.

To illustrate this approach we apply it to the Pluto-Charon system, a doubly synchronous binary for which only mean radius information has been reliably measured. The density and shape results of Nimmo et al.'s analysis of New Horizons images report the density of Pluto and Charon to be $1854 \frac{kg}{m^3}$ and $1701 \frac{kg}{m^3}$ and the mean radii to be 1188.3 ± 1.6 km and 606.0 ± 1.0 km respectively[74]. Applying our analysis to these parameters the system periods can be computed for the spherical system, Table 5.2.

Beginning from the spherical system periods we apply the linearization in three ways to understand what information can be gained from this analysis. The first approach is to perturb only the shape of Pluto, next only the shape of Charon is perturbed, and finally the shape of both bodies are identically perturbed. This is to say that the vector $\vec{\epsilon}$ can be expressed as $[1, 0] \bullet \epsilon_{Pluto}$, $[0, 1] \bullet \epsilon_{Charon}$, and $[1, 1] \bullet \epsilon_{system}$ respectively. From these three approaches, illustrated in Fig.

Table 5.2: Linear periods of dynamical families about the nonplanar doubly synchronous equilibrium evaluated for the spherical Pluto-Charon system. DNE, does not exist, is used to denote frequencies which cease to be periodic for the two sphere system

Family	Linear Period [days]
P_1	DNE
P_2	DNE
P_3	DNE
P_4	DNE
P_5	6.39
P_6	6.39
P_7	6.39
Orbit Period	6.39

5.7, we see that the relative behavior of the periods differs uniquely for deformation of each body. From left to right the figures show and elongation of only Pluto, elongation of only Charon, and equal elongation of both Pluto and Charon. This implies that through measurement of the relative lengths of the periods, information on the mass distribution could be gathered to help constrain each body's mass distribution. As is clear from these results however, the deformation of the bodies would need to be sufficiently large to be detected by realistic measurement methods.

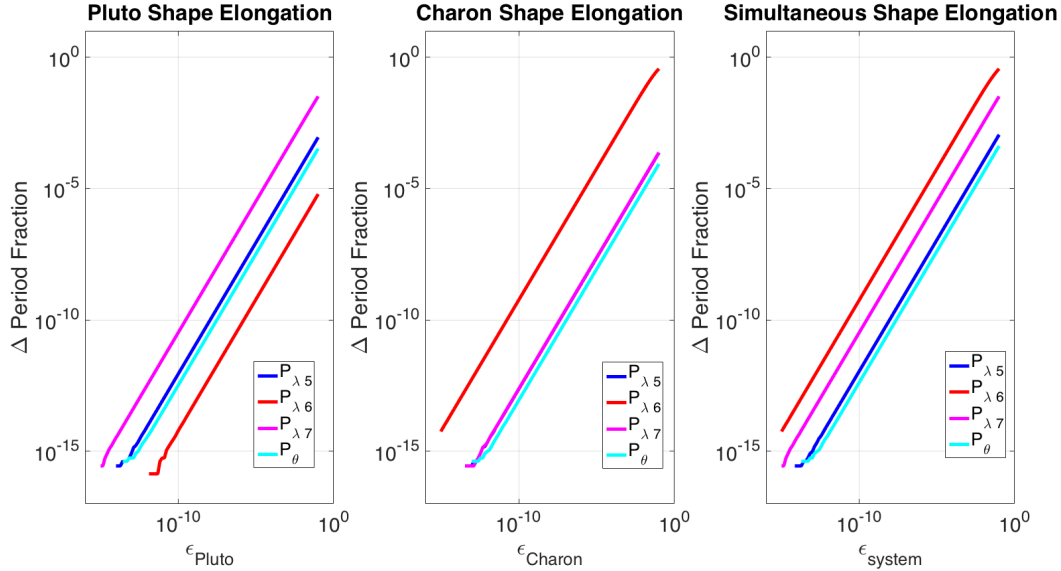


Figure 5.7: Linearized change in Pluto-Charon dynamical family periods as shape is modified by ϵ parameter.

For a comparison point we also compute the complete set of nonplanar periods associated with an ellipsoidal mass distribution for both Pluto and Charon generated with a value of $\epsilon = .0008$. This value of ϵ is selected because it lies in the middle of the certainty bounds on the mean radius values reported by Nimmo et al; representing roughly a 1 km deformation in Pluto's semi-axes and a .5 km change in Charon's semi-axes. This is reported in Table 5.3 and further confirms the difficulty of applying our approach to a system so near to the spherical case. The four short periods would not be feasible to distinguish or measure with sufficient accuracy. The four long periods on the other hand would require logistically impossible measurement efforts to be accurately and precisely observed, due to their length.

Table 5.3: Linear periods of dynamical families about the nonplanar doubly synchronous equilibrium evaluated for the $\epsilon=.0008$ Pluto-Charon system.

Family	Linear Period [days]
P_1	4659.25
P_2	1442.06
P_3	393.35
P_4	96.37
P_5	6.39
P_6	6.39
P_7	6.33
Orbit Period	6.39

5.4 Summary

In this chapter we have shown that the influence of mass parameters on the observable dynamics of binary asteroids. This was accomplished using second order order dynamics for the outer stable equilibrium. The use of the doubly synchronous equilibrium assumption allowed for a relatively simple differential corrector method to estimate fundamental frequencies of the system as a target binary oscillates near the equilibrium. We analyzed the dynamical families of the planar problem and investigated the influence of mass parameters on the linear behavior of these dynamical families to understand how they may affect observations of these systems. For the planar case we found that the mass parameters were not fully observable based purely on observations of the dynamics and would require other in-situ or remote observations to constrain a system's mass parameters. For the nonplanar F2BP we were able to show that the mass parameters were fully measurable using only observations of the system dynamics, although the observational requirements are demanding. For the nonplanar differential corrector estimation we were able to investigate the achievable covariance of the estimated mass parameters based on the accuracy of observations of the system dynamics. This provides an understanding of the information quality requirements for the proposed mass parameter estimation approach to be effective. From this analysis we can conclude that more robust measurements, likely from an in-situ spacecraft, would be necessary for mass parameter estimation. Finally, a limited approach applying this analysis to

near-spherical systems was presented and applied to the Pluto-Charon system.

Chapter 6

A Covariance Study for Gravity Estimation at Binary Asteroids

Having previously investigated mass parameter estimation based on dynamic coupling in the F2BP, this chapter seeks to understand the estimation of mass parameters for an in-situ spacecraft. This requires that a new set of dynamics be established which include a spacecraft in the F2BP; referred to here as the restricted full three-body problem (RF3BP). The RF3BP maintains the dynamics of the F2BP, but incorporates the motion of a massless spacecraft. In addition to developing the EOMs for the the RF3BP, the associated dynamics matrix and mass parameter sensitivity matrix (MPSM) must also be developed to enable a consider covariance analysis. The consider covariance analysis implemented builds off of a standard classical Kalman filter (CKF) and is used to consider the uncertainty in the system caused by mass parameters ignored in the estimation. This analysis is applied to the HERA spacecraft, which will orbit and measure 65803 Didymos after the DART mission impact on the system. Two long-term stable trajectories (passively stable for >40 days) are analyzed for their sensitivity to the asteroid masses, inertias, and higher order mass parameters. Additionally, the effects of relaxed and excited binary dynamics as well as mass parameter uncertainty sources are investigated. The analysis shows that the RF3BP is highly sensitive to all orders of mass parameters, providing better mass parameter observability than for single asteroid systems.

6.1 The Restricted Full Three-Body Problem

To begin our analysis we must derive the equations of motion and sensitivity matrices for the RF3BP. Within the RF3BP the binary asteroid dynamics remain the same as the F2BP dynamics, presented in Sec. 2.1. Because of the tendency towards quasi-periodicity or chaos in the F2BP, fixed-point solutions like the Lagrange points devolve into chaotic oscillations about their traditional locations. As a result the RF3BP diverges significantly from classical three-body problem solutions in the circular restricted three-body problem (CR3BP). The key change in the derivation of the dynamics is addition of the mutual gravity potential between the point mass spacecraft and the irregularly shaped asteroids. It is the introduction of these higher order gravity terms that complicate the development of the dynamics matrix and mass parameter sensitivity matrix.

6.1.1 Equations of Motion

Like the CR3BP, the spacecraft's state is measured relative to the binary system's center of mass. The spacecraft state has 3 degrees of freedom, with its state consisting only of its position and velocity, $\vec{r}_{s/c}$ and $\dot{\vec{r}}_{s/c}$.

$$\vec{X}_3 = \begin{bmatrix} \vec{r}_{s/c} & \dot{\vec{r}}_{s/c} \end{bmatrix}^T \quad (6.1)$$

The geometry of the spacecraft in the system is illustrated in Fig. 6.1. The EOM for the spacecraft

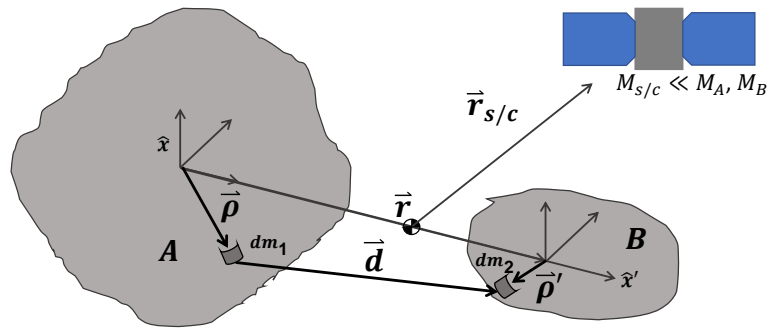


Figure 6.1: Diagram of RF3BP geometry.

can be derived directly from Newton's Second Law as

$$\ddot{\vec{r}}_{s/c} = -\frac{\partial U_{13}}{\partial \vec{r}_{A,s/c}} - \frac{\partial U_{23}}{\partial \vec{r}_{B,s/c}} \quad (6.2)$$

Where U_{i3} represents the gravity potential between body i and the spacecraft. The relative position from body i to the spacecraft is

$$\vec{r}_{A,s/c} = \vec{r}_{s/c} + \mu \mathbf{C} \vec{r} \quad (6.3)$$

$$\vec{r}_{B,s/c} = \vec{r}_{s/c} + (\mu - 1) \mathbf{C} \vec{r} \quad (6.4)$$

Where the μ is the binary's mass fraction, defined as

$$\mu = \frac{M_B}{M_A + M_B} \quad (6.5)$$

To treat the spacecraft as a massless particle, its 0th order inertia integral or, the spacecraft mass, is set to 1 and all other values are set to 0. In so doing the gravity accelerations on the spacecraft are automatically computed in a mass normalized form by the inertia integral mutual gravity potential.

6.1.2 Partial Matrices

With the EOMs defined we now derive the partials of the RF3BP dynamics to the uncertainty in the state and mass parameters of this system. To capture this uncertainty the STM, $\Phi(t, t_0)$, and MPSM, Ψ , are developed for the full state of the RF3BP,

$$\vec{X} = \begin{bmatrix} \vec{X}_2 & \vec{X}_3 \end{bmatrix}^T = \begin{bmatrix} \vec{r} & \vec{\theta}_1 & \vec{\theta}_2 & \dot{\vec{r}} & \vec{\omega}_1 & \vec{\omega}_2 & \vec{r}_{s/c} & \dot{\vec{r}}_{s/c} \end{bmatrix}^T \quad (6.6)$$

and the mass parameters up to the second order,

$$\vec{T} = \begin{bmatrix} M_A & M_B & T_A^{200} & T_A^{020} & T_A^{002} & T_B^{200} & T_B^{020} & T_B^{002} \end{bmatrix}^T \quad (6.7)$$

When higher order mass parameters are considered, the mass parameters up the second order are instead added to the state vector. Instead the considered higher order mass parameters are

$$\vec{T}_{HOT} = \begin{bmatrix} \vec{T}_A(N=3,4) & \vec{T}_B(N=3,4) \end{bmatrix} \quad (6.8)$$

The derivation of the STM begins by defining the dynamics matrix, \mathbf{A} , for the full dynamics

$$\dot{\vec{X}} = \mathbf{A}\vec{X} \quad (6.9)$$

such that

$$\mathbf{A} = \begin{bmatrix} 0_{3 \times 3} & 0_{3 \times 3} & 0_{3 \times 3} & I_{3 \times 3} & 0_{3 \times 3} & 0_{3 \times 3} & 0_{3 \times 3} & 0_{3 \times 3} \\ 0_{3 \times 3} & \frac{\partial \dot{\theta}_1}{\partial \theta_1} & 0_{3 \times 3} & 0_{3 \times 3} & \mathbf{B}_1 & 0_{3 \times 3} & 0_{3 \times 3} & 0_{3 \times 3} \\ 0_{3 \times 3} & 0_{3 \times 3} & \frac{\partial \dot{\theta}_2}{\partial \theta_2} & 0_{3 \times 3} & 0_{3 \times 3} & \mathbf{B}_2 & 0_{3 \times 3} & 0_{3 \times 3} \\ \frac{\partial \ddot{r}}{\partial r} & 0_{3 \times 3} & \frac{\partial \ddot{r}}{\partial \theta_2} & \frac{\partial \ddot{r}}{\partial r} & \frac{\partial \ddot{r}}{\partial \omega_1} & 0_{3 \times 3} & 0_{3 \times 3} & 0_{3 \times 3} \\ \frac{\partial \dot{\omega}_1}{\partial r} & 0_{3 \times 3} & \frac{\partial \dot{\omega}_1}{\partial \theta_2} & 0_{3 \times 3} & \frac{\partial \dot{\omega}_1}{\partial \omega_1} & 0_{3 \times 3} & 0_{3 \times 3} & 0_{3 \times 3} \\ \frac{\partial \dot{\omega}_2}{\partial r} & 0_{3 \times 3} & \frac{\partial \dot{\omega}_2}{\partial \theta_2} & 0_{3 \times 3} & \frac{\partial \dot{\omega}_2}{\partial \omega_1} & \frac{\partial \dot{\omega}_2}{\partial \omega_2} & 0_{3 \times 3} & 0_{3 \times 3} \\ 0_{3 \times 3} & I_{3 \times 3} \\ \frac{\partial \ddot{r}_{s/c}}{\partial r} & \frac{\partial \ddot{r}_{s/c}}{\partial \theta_1} & \frac{\partial \ddot{r}_{s/c}}{\partial \theta_2} & 0_{3 \times 3} & 0_{3 \times 3} & 0_{3 \times 3} & \frac{\partial \ddot{r}_{s/c}}{\partial r_{s/c}} & 0_{3 \times 3} \end{bmatrix} \quad (6.10)$$

The STM is then computed during integration as

$$\dot{\Phi}(t, t_0) = \mathbf{A}\Phi(t, t_0) \quad (6.11)$$

where

$$\Phi(t_0, t_0) = I_{24 \times 24} \quad (6.12)$$

The derivation of the MPSM begins with a linearization of the dynamics with respect to the mass parameters

$$\frac{\partial}{\partial t} \left[\frac{\partial \vec{X}}{\partial \vec{T}} \right] = \frac{\partial \dot{\vec{X}}}{\partial \vec{X}} \Big|_{\vec{T}}^* \frac{\partial \vec{X}}{\partial \vec{T}} + \frac{\partial \dot{\vec{X}}}{\partial \vec{T}} \Big|_{\vec{X}}^* \quad (6.13)$$

Where the $|^*$ indicates evaluation at the reference state. $\frac{\partial \dot{\vec{X}}}{\partial \vec{X}} \Big|_{\vec{T}}^*$ is defined to be the MPSM, Ψ , $\frac{\partial \dot{\vec{X}}}{\partial \vec{T}} \Big|_{\vec{X}}^*$ is the dynamics matrix defined above, \mathbf{A} , and $\frac{\partial \dot{\vec{X}}}{\partial \vec{T}} \Big|_{\vec{T}}^*$ is defined as the mass parameter partials matrix, \mathbf{B} . The linearization is thus simplified to

$$\dot{\Psi} = \mathbf{A}\Psi + \mathbf{B} \quad (6.14)$$

such that

$$\mathbf{B} = \begin{bmatrix} 0_{3 \times 1} & 0_{3 \times 1} & 0_{3 \times 3} & 0_{3 \times 3} \\ 0_{3 \times 1} & 0_{3 \times 1} & 0_{3 \times 3} & 0_{3 \times 3} \\ 0_{3 \times 1} & 0_{3 \times 1} & 0_{3 \times 3} & 0_{3 \times 3} \\ \frac{\partial \ddot{\mathbf{r}}}{\partial M_A} & \frac{\partial \ddot{\mathbf{r}}}{\partial M_B} & \frac{\partial \ddot{\mathbf{r}}}{\partial \vec{T}_A} & \frac{\partial \ddot{\mathbf{r}}}{\partial \vec{T}_B} \\ \frac{\partial \dot{\omega}_1}{\partial M_A} & \frac{\partial \dot{\omega}_1}{\partial M_B} & \frac{\partial \dot{\omega}_1}{\partial \vec{T}_A} & \frac{\partial \dot{\omega}_1}{\partial \vec{T}_B} \\ \frac{\partial \dot{\omega}_2}{\partial M_A} & \frac{\partial \dot{\omega}_2}{\partial M_B} & \frac{\partial \dot{\omega}_2}{\partial \vec{T}_A} & \frac{\partial \dot{\omega}_2}{\partial \vec{T}_B} \\ 0_{3 \times 1} & 0_{3 \times 1} & 0_{3 \times 3} & 0_{3 \times 3} \\ \frac{\partial \ddot{\mathbf{r}}_{s/c}}{\partial M_A} & \frac{\partial \ddot{\mathbf{r}}_{s/c}}{\partial M_B} & \frac{\partial \ddot{\mathbf{r}}_{s/c}}{\partial \vec{T}_A} & \frac{\partial \ddot{\mathbf{r}}_{s/c}}{\partial \vec{T}_B} \end{bmatrix} \quad (6.15)$$

where for brevity we introduce the notation

$$\vec{T}_i = \begin{bmatrix} T_i^{200} & T_i^{020} & T_i^{002} \end{bmatrix}^T \quad (6.16)$$

For the detailed contents of \mathbf{A} and \mathbf{B} see Appendix B.

6.2 Consider Covariance Filter

In this analysis we apply a consider covariance filter in order to measure the uncertainty in the estimated state caused by each mass parameter. The goal of this is to identify a mass parameter truncation order or particular terms which minimize the computational burden of navigation and radio science while providing reliable results. For this initial study we use a standard CKF to generate estimates of the binary and spacecraft states, and pair it with a sequential consider covariance analysis in order to measure the uncertainty in the state introduced by each mass parameter[75]. We note that when this analysis is performed for higher order terms, the mass and second order inertia integrals are added into the estimated state.

The consider covariance analysis introduces several new variables to the standard Kalman filter in order to capture the uncertainty introduced by each considered parameter. The considered parameters, for this work, are defined as an error relative to the truth for the system parameters

of interest, here the shape derived mass parameters

$$\bar{c} = .1\vec{T} \quad (6.17)$$

Where the column vector, \vec{T} , is the set of considered mass parameters. These mass parameters also have a corresponding apriori covariance

$$\bar{P}_{cc} = \bar{c}^T \mathbf{I}_{m \times m} \bar{c} \quad (6.18)$$

Where \mathbf{I} is the identity matrix and m denotes the length of \bar{c} . In order to track the effect of the consider parameter covariance on the state we must also introduce the matrix

$$\Psi = \frac{\partial \vec{X}}{\partial \bar{c}} = \frac{\partial \vec{X}}{\partial \vec{T}} \quad (6.19)$$

which we will refer to here as the mass parameter sensitivity matrix, derived in the previous section.

The MPSM measures the linearized affect of the consider parameters \bar{c} on the full state \vec{X} . Within the consider covariance filter we will also need the consider sensitivity matrix

$$\mathbf{S} = \frac{\partial \hat{x}}{\partial \bar{c}} \quad (6.20)$$

which relates the sensitivity of the estimated state error \vec{x} to the consider parameter error \bar{c} . Finally we define the define the cross covariance

$$\mathbf{P}_{xc} = \mathbf{S} \bar{P}_{cc} \quad (6.21)$$

Which relates the coupling between apriori consider parameter covariance and the state covariance.

6.2.1 Measurement Update

The measurement update for the consider covariance filter follows the normal structure of the CKF with the addition of two covariance updates and a states update. To begin the consider sensitivity matrix must be updated as

$$\mathbf{S}_k = \left(\mathbf{I}_{n \times n} - \mathbf{K}_k \tilde{\mathbf{H}}_{xk} \right) \bar{\mathbf{S}}_k - \mathbf{K}_k \tilde{\mathbf{H}}_{ck} \quad (6.22)$$

Where \mathbf{K}_k is the standard Kalman update, $\tilde{\mathbf{H}}_{xk}$ is the observation-state map, and $\tilde{\mathbf{H}}_{ck}$ is the observation-consider parameter map. n denotes the number of states and k denotes the measurement number. Next the total state covariance measurement update is

$$\mathbf{P}_{ck} = \mathbf{P}_k + \mathbf{S}_k \bar{\mathbf{P}}_{cc} \mathbf{S}_k^T \quad (6.23)$$

where \mathbf{P}_k denotes the estimated state covariance and \mathbf{P}_{ck} denotes the total state covariance accounting for the influence of the consider covariance. The cross covariance measurement update is simply

$$\mathbf{P}_{xck} = \mathbf{S}_k \bar{\mathbf{P}}_{cc} \quad (6.24)$$

Additionally the consider state error estimate is updated as

$$\hat{x}_{ck} = \hat{x}_k + \mathbf{S}_k \bar{c} \quad (6.25)$$

where \hat{x}_k is the standard state estimate.

6.2.2 Time Update

The time update for the consider covariance filter follows the same pattern as the measurement update. The consider sensitivity apriori update is first performed as

$$\bar{\mathbf{S}}_k = \Phi_{t_k, t_{k-1}} \mathbf{S}_{k-1} + \Psi_{t_k, t_{k-1}} \quad (6.26)$$

where Φ is the state transition matrix (STM), t_k denotes the time at measurement k and the $\bar{\cdot}$ denotes the apriori values. The total covariance apriori is then updated as

$$\bar{\mathbf{P}}_{ck} = \bar{\mathbf{P}}_k + \bar{\mathbf{S}}_k \bar{\mathbf{P}}_{cc} \bar{\mathbf{S}}_k^T \quad (6.27)$$

and the cross covariance is updated as

$$\bar{\mathbf{P}}_{xck} = \bar{\mathbf{S}}_k \bar{\mathbf{P}}_{cc} \quad (6.28)$$

Finally the consider state update is performed as

$$\bar{x}_{ck} = \bar{x}_k + \bar{\mathbf{S}}_k + \bar{c} \quad (6.29)$$

6.2.3 Measurement Model

For this study we develop a set of idealized measurements likely to be available for a realistic mission. We first assume there is DSN tracking of the spacecraft which provides range and range-rate measurements of the spacecraft relative to Earth. We use a simplified model for these measurements where range is

$$\rho = \sqrt{(x_{s/c} - x_{\oplus})^2 + (y_{s/c} - y_{\oplus})^2 + (z_{s/c} - z_{\oplus})^2} \quad (6.30)$$

Where x_i , y_i , and z_i are the J2000 positions of the spacecraft and Earth. The range-rate is then

$$\dot{\rho} = \frac{1}{\rho}((x_{s/c} - x_{\oplus})(\dot{x}_{s/c} - \dot{x}_{\oplus}) + (y_{s/c} - y_{\oplus})(\dot{y}_{s/c} - \dot{y}_{\oplus}) + (z_{s/c} - z_{\oplus})(\dot{z}_{s/c} - \dot{z}_{\oplus})) \quad (6.31)$$

To simplify the generation of the synthetic DSN measurements we assume the separation between the Earth and binary center of mass is fixed to the inertial x-axis. Additionally we ignore any motion of the DSN stations. Because our integrations are performed over periods on the order of a single day, we do not expect significant error from these assumptions. In addition to radar tracking the spacecraft is assumed to perform landmark tracking and altimetry measurements for both asteroids. Landmark tracking is simulated as a measurement of the unit direction towards the spacecraft in the body-fixed frame of each asteroid

$$\hat{\sigma}_i = \mathbf{C}_i^T \frac{\vec{r}_{i,s/c}}{R_{i,s/c}} \quad (6.32)$$

where i denotes the asteroid of interest such that the position is from asteroid i to the spacecraft. The rotation matrix, \mathbf{C}_i , is then the matrix mapping from the body fixed frame of asteroid i to the inertial from. The altimetry measure from each asteroid is then

$$l_i = \frac{\vec{r}_{i,s/c}}{R_{i,s/c}} \quad (6.33)$$

following the same notation of i . For both landmark tracking and altimetry it is assumed that both bodies are always of observable and unaffected by field of view or other measurement restrictions.

Given these simulated measurements we construct the measurement model

$$\vec{y} = \begin{bmatrix} \rho & \dot{\rho} & \hat{\sigma}_1 & \hat{\sigma}_2 & l_1 & l_2 \end{bmatrix}^T \quad (6.34)$$

and compute the measurement matrix H_x and H_c for the filter states and consider covariance parameters respectively.

$$H_x = \begin{bmatrix} \vec{0}_{1x3} & \vec{0}_{1x3} & \vec{0}_{1x3} & \vec{0}_{1x3} & \vec{0}_{1x3} & \vec{0}_{1x3} & \frac{\partial \rho}{\partial \vec{r}_{s/c}} & \vec{0}_{1x3} \\ \vec{0}_{1x3} & \vec{0}_{1x3} & \vec{0}_{1x3} & \vec{0}_{1x3} & \vec{0}_{1x3} & \vec{0}_{1x3} & \frac{\partial \dot{\rho}}{\partial \vec{r}_{s/c}} & \frac{\partial \dot{\rho}}{\partial \vec{r}_{s/c}} \\ \frac{\partial \hat{\sigma}_1}{\partial \vec{r}} & \frac{\partial \hat{\sigma}_1}{\partial \theta_1} & \vec{0}_{3x3} & \vec{0}_{3x3} & \vec{0}_{3x3} & \vec{0}_{3x3} & \frac{\partial \hat{\sigma}_1}{\partial \vec{r}_{s/c}} & \vec{0}_{3x3} \\ \frac{\partial \hat{\sigma}_2}{\partial \vec{r}} & \frac{\partial \hat{\sigma}_2}{\partial \theta_1} & \frac{\partial \hat{\sigma}_2}{\partial \theta_2} & \vec{0}_{3x3} & \vec{0}_{3x3} & \vec{0}_{3x3} & \frac{\partial \hat{\sigma}_2}{\partial \vec{r}_{s/c}} & \vec{0}_{3x3} \\ \frac{\partial l_1}{\partial \vec{r}} & \vec{0}_{1x3} & \vec{0}_{1x3} & \vec{0}_{1x3} & \vec{0}_{1x3} & \vec{0}_{1x3} & \frac{\partial l_1}{\partial \vec{r}_{s/c}} & \vec{0}_{1x3} \\ \frac{\partial l_2}{\partial \vec{r}} & \vec{0}_{1x3} & \vec{0}_{1x3} & \vec{0}_{1x3} & \vec{0}_{1x3} & \vec{0}_{1x3} & \frac{\partial l_2}{\partial \vec{r}_{s/c}} & \vec{0}_{1x3} \end{bmatrix} \quad (6.35)$$

$$H_c = \begin{bmatrix} 0 & 0 & \vec{0}_{1x3} & \vec{0}_{1x3} \\ 0 & 0 & \vec{0}_{1x3} & \vec{0}_{1x3} \\ \frac{\partial \hat{\sigma}_1}{\partial M_A} & \frac{\partial \hat{\sigma}_1}{\partial M_B} & \vec{0}_{3x3} & \vec{0}_{3x3} \\ \frac{\partial \hat{\sigma}_2}{\partial M_A} & \frac{\partial \hat{\sigma}_2}{\partial M_B} & \vec{0}_{3x3} & \vec{0}_{3x3} \\ \frac{\partial l_1}{\partial M_A} & \frac{\partial l_1}{\partial M_B} & \vec{0}_{3x3} & \vec{0}_{3x3} \\ \frac{\partial l_2}{\partial M_A} & \frac{\partial l_2}{\partial M_B} & \vec{0}_{3x3} & \vec{0}_{3x3} \end{bmatrix} \quad (6.36)$$

The details of both matrices are available in Appendix B.

The equations for H_c and H_x here describe the case when the masses and second order inertia integrals are considered. In the case that the third and fourth order mass parameters are considered, the masses and second order inertia integrals are estimated, and their measurement partials are moved into H_x . H_c then becomes a matrix of 0's because the measurements are not directly a function of the higher order mass parameters.

6.3 Application to 65803 Didymos

We focus our analysis on the HERA mission operations about 65803 Didymos. As such we use the current mission standard for the binary system. The current model of Didymos is an asymmetric binary with the secondary in a singularly synchronous orbit. This assumes that the secondary is tidally locked in a circular orbit whose period matches the secondary's spin period.

Table 6.1 provides the orbit parameters and spin periods of the bodies. The values are based on Naidu et al while the mass parameters are based on a constant density evaluation of the radar shape model assuming a density of 2.104 g/cm^3 [5]

Table 6.1: Current Observed 65803 Didymos orbit parameters and spin state.

Primary Spin Period [hr]	Orbit and Secondary Spin Period [hr]	SMA [km]	Ecc.	Total Mass [kg]	Mass Fraction
2.26	11.92	1.18	0.0	5.28×10^{11}	0.0092

For the current model the shape of the primary is assumed to be the radar shape model observe by Naidu et al. in 2016. While they were unable to measure the full shape of the secondary ellipsoidal constraints were determined. In Table 6.2 we provide the ellipsoidal dimensions of each body and Fig. 6.2 illustrates a snapshot of their mutual orbit.

Table 6.2: Current ellipsoidal dimensions for 65803 Didymos [5]

$a_{pri.}$ [m]	$b_{pri.}$ [m]	$c_{pri.}$ [m]	$a_{sec.}$ [m]	$b_{sec.}$ [m]	$c_{sec.}$ [m]
414.8	410.4	395.7	104.0	80.0	67.0

When the HERA mission arrives at the Didymos system the DART spacecraft will have already impacted the secondary, leaving it in an excited state. In order to capture the effects of an excited secondary we introduce the perturbed Didymos orbit and secondary spin state parameters. This state is selected based on the expected geometry of the DART impact but exaggerated to provide clearer insight into the affect of the excitation[76].

Table 6.3: Perturbed Didymos secondary spin and orbit state

Secondary Spin Period [hr]	Secondary Precession [deg]	Secondary Nutation [deg]	Orbit Period [hr]	SMA [km]	Inc. [deg]	Ecc.
13.71	0.0	13.63	9.75	1.032	2.6	0.067

The perturbed state assumes that the mass distributions of both bodies remain the same after the impact and that the primary's spin state is unperturbed by the DART impact. While the

DART impact on the secondary will leave a crater, its effect on the mass distribution should be negligible and any dynamical coupling between the excited secondary and the primary should also be negligible because of the much lower mass of the secondary.

6.3.1 Consideration of Mass and Inertia

Our initial analysis is performed under the nominal conditions of the Didymos system provided in Table 6.1. Following the trajectory implementation described by Dell’Elce et al[48], we compare the long-term stable geometries for a terminator orbit and interior retrograde orbit. The initial conditions for the terminator orbit approximate the orbit as a circular orbit about the primary with an orbital radius of 2.5 km and an inclination of 90 degrees. Its initial position is selected as its ascending node and aligned to be ahead of the secondary by a 90 degree phase of the secondary’s orbit. The interior retrograde orbit is also approximated as a circular orbit about the primary with a .65 km orbital radius and 5 degrees of inclination. Its initial position is aligned with the initial phase of the secondary halfway between the spacecraft’s ascending and descending nodes. Fig. 6.2 illustrates both orbits in the rotating frame of the binary over a 24 hour period. We

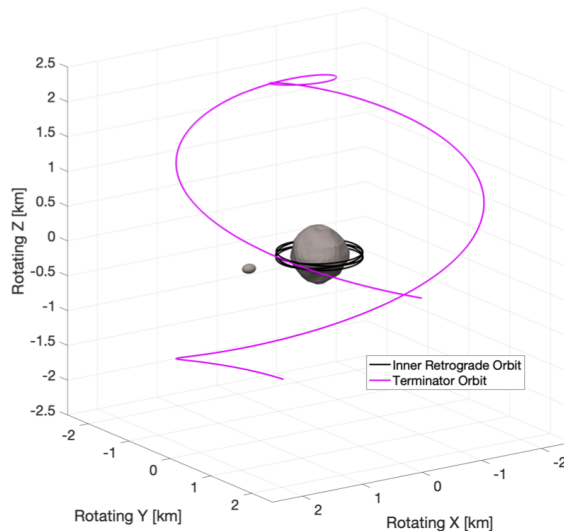


Figure 6.2: Terminator and retrograde orbits in the Didymos rotating frame over a 24 hour period.

numerically integrate both orbits and the Didymos system using the fourth-order constant-density

shape-derived mass distributions and a series of perturbed mass distributions. A perturbed mass distribution is generated for a 10% increase each body’s mass and second order inertia integrals. Thus eight perturbed mass distributions are simulated each identical to the nominal mass distribution except for the one perturbed mass or second order inertia integral term. As described in the previous section this produces an estimated consider covariance, estimated state covariance and consider state error estimate after a single iteration of the filter. As an example of this analysis Fig. 6.3 illustrates the binary position and velocity state estimate, covariance and considered covariance for a terminator orbit when the secondary’s T^{200} term is considered. It is immediately clear that

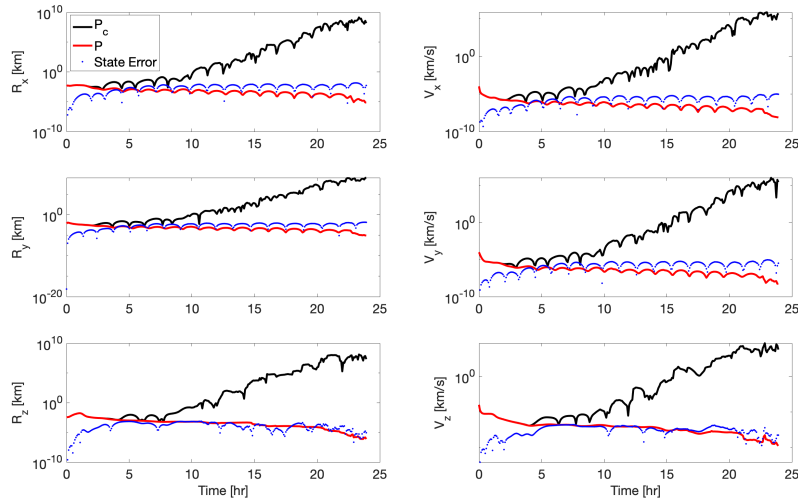


Figure 6.3: Relative position and velocity of binary state error(blue), 1 sigma covariance(red) and 1 sigma consider covariance(black) for T_B^{200} based on a spacecraft in a terminator orbit.

even a relatively small amount of uncertainty in the secondary’s inertia can lead to extreme levels of uncertainty in the estimated dynamics. We also see that the growth in state error for a small 10% error in T_B^{200} very quickly falls outside of the estimated covariance. The dramatic growth in the consider covariance is consistent across all the binary states and spacecraft states. This figure shows only one of the eight considered parameters for one of two orbits. To better capture the comparative error between all eight consider parameters for both orbits we instead plot only the final consider covariance values for each of the mass parameters, Fig. 6.4. We also reduce the state

for which the consider covariance is provided to the x-component of the binary's relative position as the behavior of the consider covariance is relatively uniform across all 24 estimated states. These

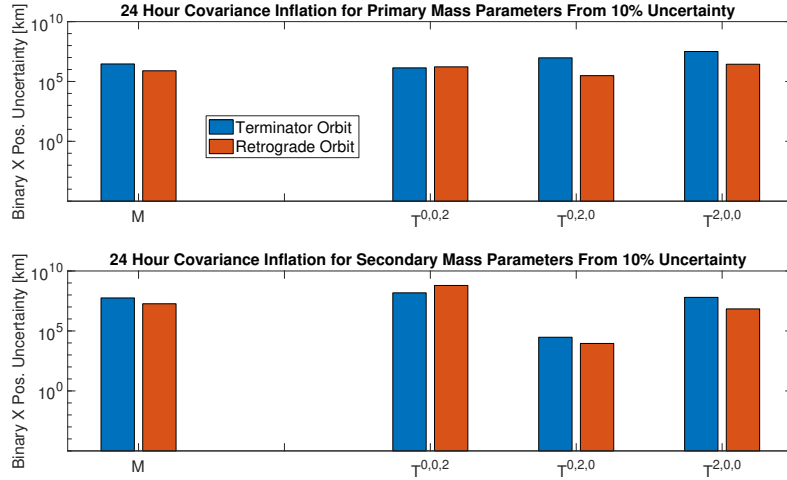


Figure 6.4: Values of the 1 sigma consider covariance after 24 hours. Results for the the masses and second order inertia integrals of both asteroids considering a spacecraft in the terminator and retrograde orbits.

results show a large growth in uncertainty introduced by errors in the masses and second order inertia integrals. While there are small differences between the effects of the primary and secondary's mass parameters this result makes it clear that all of these terms should be estimated in a true mission setting.

We can however learn more about the evolution of the uncertainty by focusing on one of the two orbits. Fig. 6.5 illustrates the the evolution of the consider covariance envelopes for the spacecraft position and velocity in the retrograde orbit. The consider covariances for the retrograde orbit reveal much about the structure of the uncertainty evolution. Firstly, the effect of uncertainty in the primary is uniformly more significant from uncertainty in the secondary until roughly 12 hour into the orbit. For each body the relative structure between the mass parameters is such that mass is most significant followed by T^{200} , then T^{020} , and finally T^{002} . This structure follows logic of the most significant size of each mass parameter as T^{200} is a component of I_{zz} and I_{yy} , the larger moments of inertia, while T^{002} is a component of I_{xx} and I_{yy} , the smaller two moments of

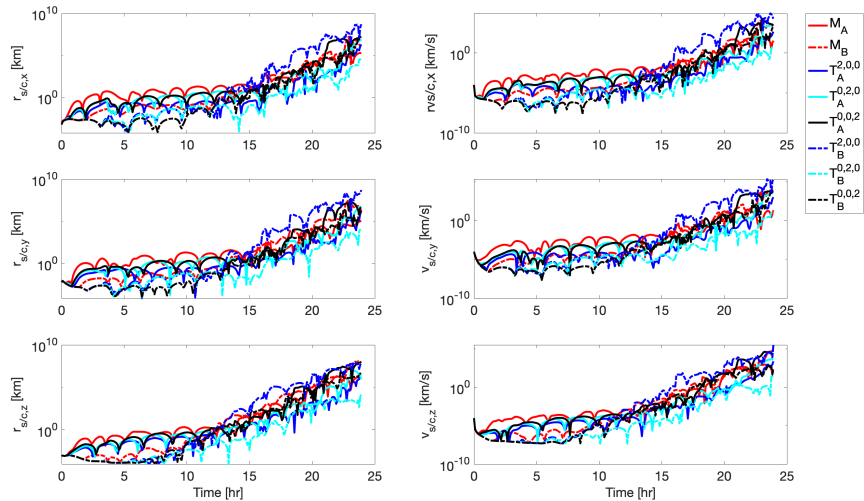


Figure 6.5: Spacecraft state 1 sigma consider covariance for each considered mass parameters based on a spacecraft in a retrograde orbit.

inertia. A similar analysis can be performed to compare the effects of the DSN measurements on the growth of uncertainty. In Fig. 6.6, we compare the final value of the consider covariance for each parameter at the end of the 24 hour integration both with and without the DSN-derived range and range-rate measurements included. In this analysis we see that the terminator has little to no

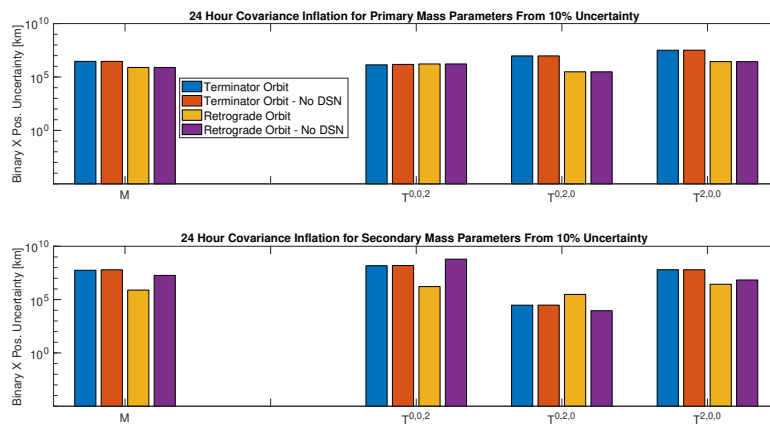


Figure 6.6: Values of the 1 sigma consider covariance after 24 hours. Results for the the masses and second order inertia integrals of both asteroids considering a spacecraft in the terminator and retrograde orbits both with and without DSN measurements.

change in the uncertainty caused by each parameter, while the retrograde orbit appears to have some sensitivity to DSN measurements when considering the secondary's mass parameters. This difference is likely because the secondary interacts more closely with both bodies and its dynamics operate of a faster time scale, thus it sees more significant improvements from DSN measurements. It is likely that these improvements are more pronounced for the secondary because of its more elongated shape relative to the much more spherical shape of the primary, at least to second order.

6.3.2 Consideration of Higher Order Terms

Following this initial exploration, the third and fourth order terms are considered. When considering the higher order terms we modify the consider covariance filter to include the masses and second order inertia integrals as estimated states such that the only considered parameters are the higher order terms. As a result no perturbed mass parameter sets are developed for these lower order terms, although the results from the previous second order consider analysis are included in the following figures for comparison. Fifty new perturbed sets are generated, reflecting the two bodies' sets of ten third order terms and fifteen fourth order terms. In Fig. 6.7 and 6.8 we provide the consider covariance final value for all mass parameters up to the fourth order for both orbits. Fig. 6.7 captures primary's mass parameters, while Fig. 6.8 captures those of the secondary. In both figures the mass and second order inertia integral results are identical to those in Fig. 6.6 when these parameters are considered and not estimated as states. From these two figures it is clear that the primary's higher order mass parameters generally have a larger impact on the uncertainty when compared to those of the secondary. The uncertainty from five of the secondary's fourth order terms do exceed the uncertainty caused by several of the primary's third and fourth order terms. These mass parameters are the secondary's T^{004} , T^{022} , T^{202} , T^{220} , and T^{400} . The clear pattern amongst these terms being that they are the terms directed along only one or two principal axes, with the exception of T^{040} . While still large relative to most of the secondary's higher order terms, T^{040} likely remains smaller due to particularities of the the secondary's shape. This provides a very important constraint on which parameters of the system are most important to be estimated in a

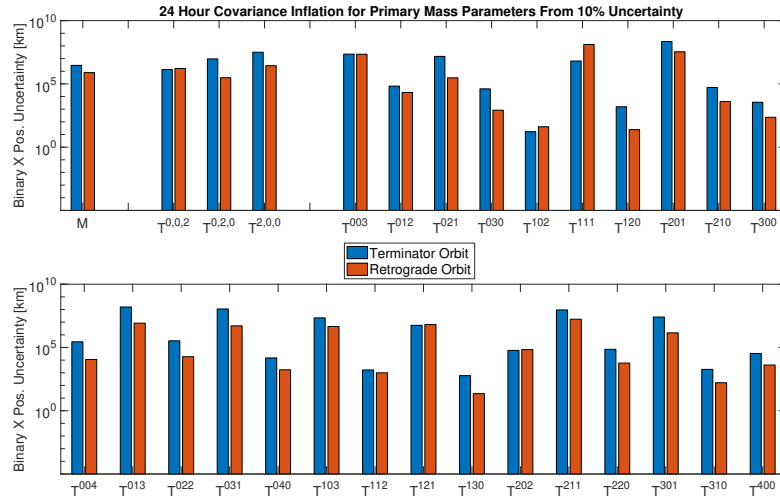


Figure 6.7: Values of the 1 sigma consider covariance after 24 hours. Results for all mass parameters of the primary considering a spacecraft in the terminator and retrograde orbits.

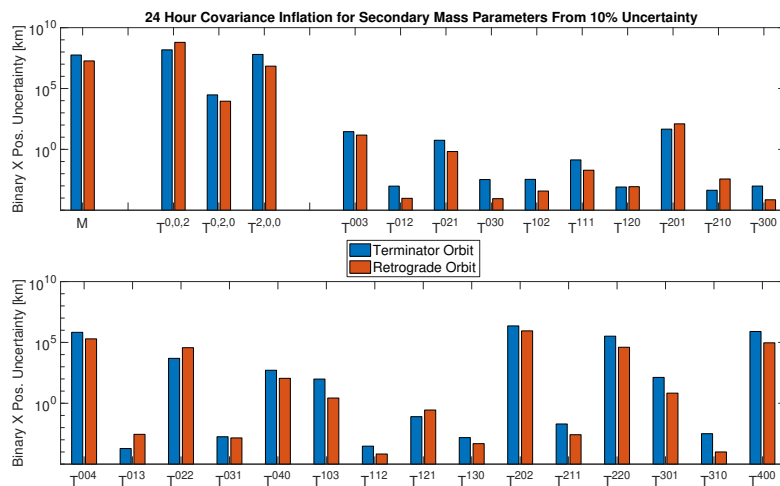


Figure 6.8: Values of the 1 sigma consider covariance after 24 hours. Results for all mass parameters of the secondary considering a spacecraft in the terminator and retrograde orbits.

mission scenario. Comparing the uncertainty between the two orbits the difference seem generally small, but more favorable to the retrograde orbit. This is likely due to the closer interactions of the retrograde orbit allowing it to better sample the dynamical space.

6.3.3 Separating Direct and Indirect Effects of Mass Parameters on the Spacecraft

To better understand the sources of uncertainty in the system we identify two subsets of error, direct and indirect error. The direct error is defined as an error in the estimated dynamical state of the binary such that the filter believes the sources of the gravity accelerations on the spacecraft to be in an incorrect location. The indirect error is then caused by uncertainty in the mass parameters of either asteroid such that the filter knows the correct dynamical states of the sources of the accelerations on the spacecraft but has erroneous values for their mass parameters. In order to separate the effect of the direct and indirect errors we run the consider covariance analysis for all mass parameters but now simulate the binary dynamics with the true mass parameters and integrate the spacecraft with the perturbed mass parameters. In so doing we remove direct errors caused by the mass distribution perturbation in the binary dynamics and isolate the indirect errors on the spacecraft motion. In Fig. 6.9 and 6.10 we provide comparative results for the previous analysis with the full system perturbed by the mass parameters and the system integrated with the nominal binary dynamics. Fig. 6.9 captures primary's mass parameters for both orbits and Fig. 6.10 captures the secondary's mass parameters for both orbits. For both orbits we include the consider covariance for the system fully perturbed by the mass parameters and the system run with nominal binary dynamics. Only the x-component of the binary relative position is provided as the behavior of the consider covariance is relatively uniform across all states. The clearest trend from this analysis is the much larger impact on the uncertainty of the masses and second order inertia integrals than the higher order terms. The reason for this is likely that these terms dominate the system dynamics whereas the higher order terms have a more subtle effect on the system. This also tells us that the larger source of uncertainty here is the direct errors, that is errors in the estimate of the binary dynamics. Of additional interest is the spike in uncertainty for the primary's T^{310} term in the retrograde orbit with nominal binary dynamics. It may be that the spacecraft has some close interaction with a zone or section of the primary linked to this term. Thus no comparable spike is seen for the terminator orbit.

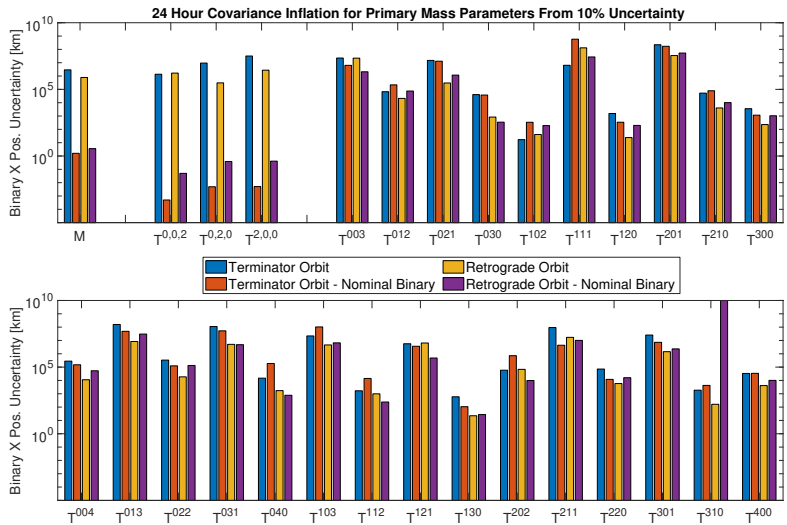


Figure 6.9: Values of the 1 sigma consider covariance after 24 hours. Results for all mass parameters of the primary considering a spacecraft in the terminator and retrograde orbits.

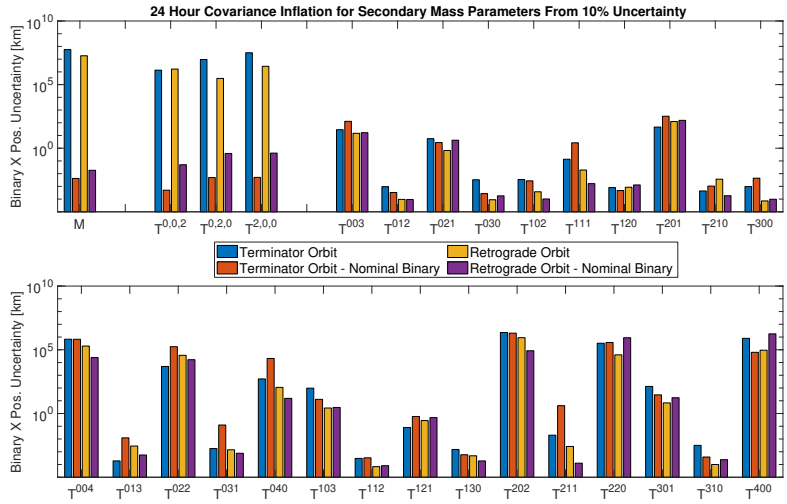


Figure 6.10: Values of the 1 sigma consider covariance after 24 hours. Results for all mass parameters of the secondary considering a spacecraft in the terminator and retrograde orbits.

6.3.4 Effects of Excited Mutual Dynamics

It is also important that the effects of excited dynamics are well understood. To capture this we rerun the consider covariance analysis for all mass parameters given the excited binary state

described in Table 6.3. The same spacecraft orbit types and initial conditions are selected in order to provide a more direct comparison to the uncertainty in the nominal system. As in the previous subsection, we provide two figures, Fig. 6.11 and 6.12, which respectively compare the uncertainty in the primary and secondary’s mass parameters for both orbits given the nominal and perturbed dynamics. For both orbits we include the consider covariance for the system nominal dynamics and excited dynamics. Only the x-component of the binary relative position is provided as the behavior of the consider covariance is relatively uniform across all states. For this analysis we see a general

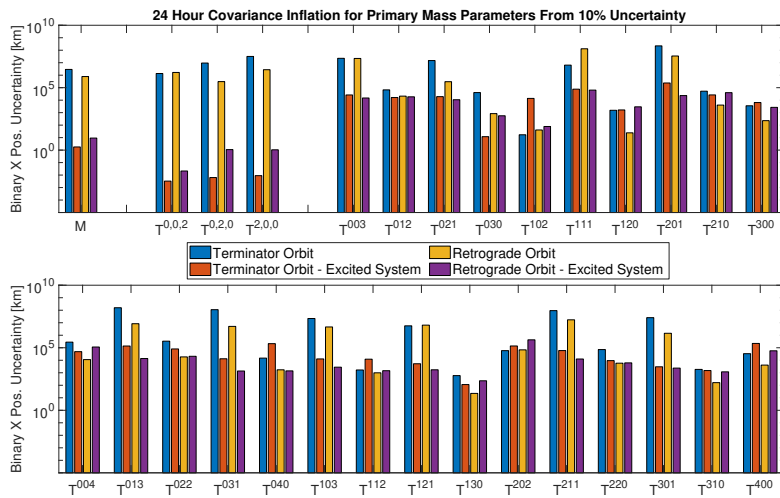


Figure 6.11: Values of the 1 sigma consider covariance after 24 hours. Results for all mass parameters of the primary considering a spacecraft in the terminator and retrograde orbits.

decrease in uncertainty given the excited system with a larger impact for the masses and second order inertia integrals. The decrease in uncertainty under excited dynamics is a result of increased observability of the excited dynamics. Under the nominal dynamics the secondary is tidally locked such that it has very little change in attitude and orbit over time. On the other hand the excited system will oscillate about this tidally locked state providing more observability simply due to the increased degree of motion in the system. The impact remains most significant for the lower order terms because they influence the overall dynamics of the system more significantly. We do see for the secondary that the fourth order mass parameters directed purely along one or two principal

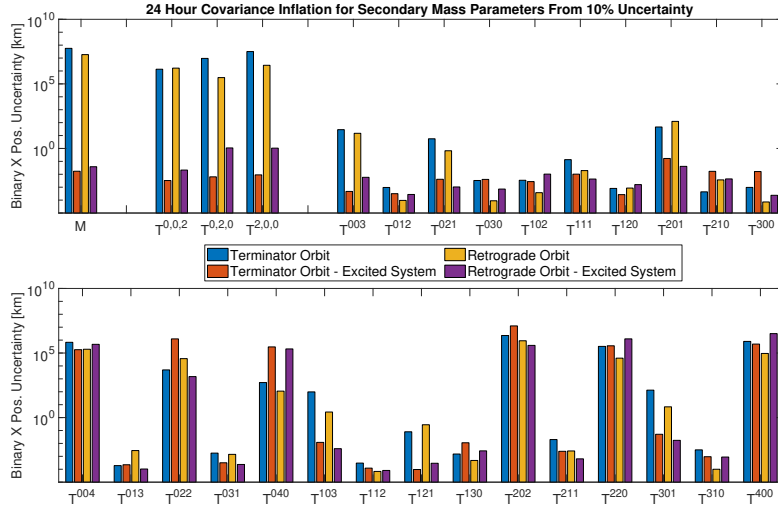


Figure 6.12: Values of the 1 sigma consider covariance after 24 hours. Results for all mass parameters of the secondary considering a spacecraft in the terminator and retrograde orbits.

axes remain the most significant of the higher order terms, further supporting the importance of estimating these higher order terms.

6.4 Summary

In this chapter we develop a consider covariance framework for a spacecraft estimating the mass parameters of a binary asteroid system. Analytical formulations for the RF3BP dynamic matrix and mass parameter sensitivity matrix are computed and provided in detail. A simple measurement model is developed assuming DSN and OPNAV measurements. Combined, these tools allow us to perform a consider covariance analysis on the estimation of binary mass parameters. We find that regardless of the orbit, the masses and second order inertia integrals are necessary to achieve meter level accuracy in the spacecraft state. Additionally, we find that DSN measurements are do not have a significant impact on uncertainty for the relative navigation filter implemented here, Fig. 6.6; this shows value for an autonomous mission. For the higher order terms we see that the primary's terms are most significant, with the fourth order terms of both bodies being more important than the third order terms in the case of the Didymos system. In particular the

secondary's fourth order terms directed along two or fewer principal axes; T^{004} , T^{040} , T^{400} , T^{202} , T^{220} , and T^{022} , seem to be most important for the secondary. In assessing the source of error most impactful on the filter, we see that error in the binary dynamics is likely to contribute more to the uncertainty than errors in the mass parameters. Finally, we see that excited systems, that is binaries oscillating about the singly synchronous equilibrium, are more observable than relaxed systems in which the secondary is tidally locked. Moving towards a mission ready filter other perturbations, such as solar radiation pressure, will be important effects to understand.

Chapter 7

Conclusion

In this thesis we have broadly applied improved dynamics models of the F2BP to better understand the formation, remote estimation, and in-situ estimation of binary asteroids. We first implemented and developed an arbitrary shape and order form of the F2BP. The equilibria within this dynamics model and their dynamical structure were then studied to map the dynamical families of the stable equilibrium and identify a breakdown in structure about the unstable equilibrium. High fidelity F2BP models were then implemented to understand their impact, as well as that of the unstable equilibrium's warped structure, on the formation and evolution of binary asteroids. Further investigating the dynamical structure of the stable equilibrium, we leveraged the sensitivity of its fundamental frequencies to study the remote estimation of binary mass parameters. Finally, a consider covariance analysis was performed for an in-situ spacecraft orbiting a binary system in order to identify the sensitivity of the dynamics to the asteroid mass parameters. Working from high fidelity dynamical models, we developed the tools to better understand binary formation and evolution, provide robust mission planning techniques, and safer navigation about binary asteroid systems.

In Chapter 2 of this thesis we delineated the inertia integral implementation of the F2BP and detailed a benchmarking campaign between several F2BP implementations. In the first half of the benchmarking campaign we compared the high accuracy of the polyhedral implementation with that of the inertia integral implementation. It was shown that individual evaluations of the mutual gravity potential agree to numerical precision and that when integrated with the LGVI

the results showed good agreement. In the second half of the benchmarking, the computational efficiency between several forms of the polyhedral implementation and the packed spheres method were compared with the inertia integral implementation. This test showed that the inertia integral implementation can be run at a higher expansion order than other models while still remaining orders of magnitude faster than other methods. Thus it was shown that the inertia integral implementation of the F2BP provides improvements in both dynamical accuracy and computational efficiency.

The thesis then focused on the equilibria and dynamical structure of the F2BP. For the outer stable equilibrium, three dynamical families of the planar F2BP were mapped into nonlinear space and their behaviors characterized. The dynamical families of the nonplanar F2BP were then identified. The nonplanar case showed the continued existence of planar libration and relative separation families, while also identifying families associated with the precession and nutation of both asteroids and their mutual orbit in addition to a relative twist family. For the inner unstable equilibrium, analysis identified the breakdown of the unstable equilibrium as a barrier to binary fission and recollision. While this structure was maintained when expanding from the planar to nonplanar problem at order 2, the expansion to order 4 introduced stronger dynamical coupling between the attitude and orbit. The strengthened coupling warps the dynamical structure about the inner equilibrium such that recollision is possible.

With the breakdown of the inner unstable equilibrium as a barrier to recollision, its impact on binary formation and evolution theories were investigated. In Monte Carlo simulations of Moshup and 1996 HW1 the broad statistical conclusions of JS2011 are generally consistent. The key differences identified for these two binaries were the out of plane, and often tumbling, ejection of escaping secondaries and complex behavior at the moment of secondary fission. Both of these new behaviors are likely to have consequences for explaining observed binaries, but also asteroid pairs. Beyond this, the existence of recollisions showed significant deviation from past theories, while not disproving their general predictions. The Monte Carlo studies of DP107 also show the difficulty, at least in this case, of binary formation from equatorial mass ejection. While the studies of Moshup

and DP107 seem to support the importance of secondary fission as a means of energy dissipation, they do suggest that this is likely to be a much more complex process in need of further study.

In Chapter 5 the thesis further explored the outer stable equilibrium, attempting to probe the estimation of binary mass parameters from remote observations. In an initial study of the planar problem, the mathematical feasibility of the proposed approach was proved, but the planar problem is under-constrained. The analysis was expanded to the well posed nonplanar problem and it is shown that remote estimation of mass parameters from observations of binary asteroid dynamics is technically feasible. Unfortunately, the required accuracy of dynamical measurements would likely be unrealistic for distant observers. In the case of a long approaching flyby, like that of the LUCY mission at 617 Patroclus, the required measurements may be attainable. When adapted to near-spherical binaries, like the Pluto-Charon system, the approach was shown to provide helpful constraints for other analysis, but unlikely to provide high-precision results.

Chapter 6 further developed estimation of binary asteroid mass parameters by implementing a consider covariance analysis for in-situ spacecraft. This analysis showed that in-situ spacecraft are sensitive to mass parameters up to the fourth order, suggesting they should be able to be estimated. Amongst the higher order terms the spacecraft appears to be most sensitive to mass parameters directed along one or two axes as opposed to all three axes. For example, T^{400} and T^{022} would be more observable than terms like T^{112} . Because of the use of the relatively spherical Didymos as a target for the study herein, this may not hold for other less symmetric asteroids. In addition to the sensitivity to different mass parameters, the effect of error sources and dynamical excitement were also investigated. Direct errors, i.e. errors in the dynamical state of the binary, were shown to be more impactful on the filter uncertainty than indirect errors from errors in the mass parameters. Finally, a more excited system was shown to be more observable due to the increased mutual motion of the system providing better constraints.

While the research presented in this thesis lays the groundwork for future studies and mission capabilities, like all research, it identifies many new questions. Firstly, the dynamical structure about both equilibria warrants further investigation. In particular, a continuation of the nonplanar

dynamical families about the stable equilibrium and an investigation of the mass parameter impacts on the structure about the unstable equilibrium. Secondary fission during binary evolution also poses many questions which would require a Full N-body Problem (FNBP) dynamics model in order to be studied. In the realm of estimation the full estimation of higher order mass parameters and more realistic measurement models will be important steps for these tools to be mission ready.

Continuation of the nonplanar dynamical families about the stable equilibrium, while conceptually simple, faces technical challenges due to the stronger dynamical coupling present in nonplanar problem. While their characterization is interesting from an academic sense, identification of these behaviors has been identified as a key interest for the DART mission. Given an excited binary, potentially having been recently impacted by a spacecraft, the behavior would be expected to be a coupling of these dynamical families. A nonlinear understanding of their behavior will provide insight into how they might couple but could also provide information about the perturbations which cause the excitement. In the case of the DART mission this would provide further constraints on the spacecraft impact conditions.

The breakdown of the unstable equilibrium as a barrier to recollision for higher order evaluations complicates the story of binary formation and evolution. To better understand the reasons for this breakdown it will be helpful to isolate the impact of each higher order mass parameter has on the dynamics. Whether this is approached analytically, via dynamical systems theory, or by numerical study, it is suspected that particular asymmetric mass parameters will excite the behavior of interest. Building on this a broader approach to the dynamical structure about the unstable equilibria which attempts to identify the influences on this structural bifurcation.

Our analysis of secondary fission during binary asteroid evolution left many questions about how this process could occur. In addition to identifying the likelihood of both bi-lobed secondary fission and cohesive fission, the fates of fissioned particles are also of interest. Understanding the fates of secondary fission particles, produced by both fission models, will require an FNBP based approach. Understanding these behaviors would have important consequences for understanding the fates of ejected or reimpacting secondary components. It may be possible that telltale cratering

behaviors could be identified or that ejected secondary debris may have identifiable characteristics. These types of results would produce predictions for both binary asteroid evolution, asteroid pairs and more generally, solar system formation.

In order to develop mission ready estimation tools for binary asteroids, several aspects of the filtering model developed herein must be improved. Firstly, the observation model is simplified to a level that likely makes particular terms appear more observable than they would be under realistic measurement conditions. In addition to this, the observability of spacecraft and binary state would be improved by developing an inertial estimation framework as opposed to a relative navigation framework. The relative navigation approach used in the covariance analysis is a part of Chapter 6 found DSN measurements to be less important. Higher order mass parameters should also be incorporated into the filter's estimated parameters, particularly those that follow the two or fewer axis alignment, i.e T^{220} and T^{400} . Further the effects of perturbations of the spacecraft like solar radiation pressure and gravity from external perturbers should be studied for potential effect on estimation quality. It would also be of interest to reevaluate remote mass parameter estimation under the more complete filtering framework developed in Chapter 6. While it is unlikely that better results would be available, it would provide better constraints on how close an observer may need to be and what measurements types would be ideal.

Bibliography

- [1] Steven J Ostro, Jean-Luc Margot, Lance AM Benner, Jon D Giorgini, Daniel J Scheeres, Eugene G Fahnestock, Stephen B Broschart, Julie Bellerose, Michael C Nolan, Christopher Magri, et al. Radar imaging of binary near-earth asteroid (66391) 1999 kw4. Science, 314(5803):1276–1280, 2006.
- [2] Christopher Magri, Ellen S Howell, Michael C Nolan, Patrick A Taylor, Yanga R Fernández, Michael Mueller, Ronald J Vervack Jr, Lance AM Benner, Jon D Giorgini, Steven J Ostro, et al. Radar and photometric observations and shape modeling of contact binary near-earth asteroid (8567) 1996 hw1. Icarus, 214(1):210–227, 2011.
- [3] Ellen S Howell, C Magri, MC Nolan, PA Taylor, RJ Vervack Jr, YR Fernandez, M Mueller, LAM Benner, JD Giorgini, DJ Scheeres, et al. Radar shape modeling of (8567) 1996 hw1 combined with thermal observations. In Bulletin of the American Astronomical Society, volume 42, page 1080, 2010.
- [4] Shantanu P Naidu, Jean-Luc Margot, Patrick A Taylor, Michael C Nolan, Michael W Busch, Lance AM Benner, Marina Brozovic, Jon D Giorgini, Joseph S Jao, and Chris Magri. Radar imaging and characterization of the binary near-earth asteroid (185851) 2000 dp107. The Astronomical Journal, 150(2):54, 2015.
- [5] Shantanu Naidu, L Benner, M Brozovic, SJ Ostro, MC Nolan, JL Margot, JD Giorgini, C Magri, P Pravec, P Scheirich, et al. Observations and characterization of binary near-earth asteroid 65803 didymos, the target of the aida mission. In AGU Fall Meeting Abstracts, 2016.
- [6] DJ Scheeres. Stability of the planar full 2-body problem. Celestial Mechanics and Dynamical Astronomy, 104(1-2):103–128, 2009.
- [7] Masatoshi Hirabayashi and Daniel J Scheeres. Rotationally induced failure of irregularly shaped asteroids. Icarus, 317:354–364, 2019.
- [8] MJS Belton, CR Chapman, PC Thomas, ME Davies, R Greenberg, K Klaasen, D Byrnes, L D’amario, S Synnott, TV Johnson, et al. Bulk density of asteroid 243 ida from the orbit of its satellite dactyl. Nature, 374(6525):785–788, 1995.
- [9] Keith S Noll, William M Grundy, Eugene I Chiang, Jean-Luc Margot, and Susan D Kern. Binaries in the kuiper belt. arXiv preprint astro-ph/0703134, 2007.
- [10] Jean-Luc Margot, MC Nolan, LAM Benner, SJ Ostro, RF Jurgens, JD Giorgini, MA Slade, and DB Campbell. Binary asteroids in the near-earth object population. Science, 296(5572):1445–1448, 2002.

- [11] Petr Pravec, P Scheirich, P Kušnirák, L Šarounová, Stefano Mottola, Gerhard Hahn, P Brown, G Esquerdo, N Kaiser, Z Krzeminski, et al. Photometric survey of binary near-earth asteroids. Icarus, 181(1):63–93, 2006.
- [12] Jean-Luc Margot, Petr Pravec, Patrick Taylor, Benoît Carry, and Seth Jacobson. Asteroid systems: binaries, triples, and pairs. Asteroids IV, pages 355–374, 2015.
- [13] Kevin J Walsh, Derek C Richardson, and Patrick Michel. Rotational breakup as the origin of small binary asteroids. Nature, 454(7201):188, 2008.
- [14] Patrick Michel, Andrew Cheng, Michael Küppers, Petr Pravec, J Blum, Marco Delbo, SF Green, P Rosenblatt, K Tsiganis, Jean-Baptiste Vincent, et al. Science case for the asteroid impact mission (aim): a component of the asteroid impact & deflection assessment (aida) mission. Advances in Space Research, 57(12):2529–2547, 2016.
- [15] HF Levison et al. Lucy: surveying the diversity of the trojan asteroids, the fossils of planet formation. In Lunar and Planetary Science Conference, volume 47, page 2061, 2016.
- [16] DJ Scheeres, JW McMahon, J Wood, EB Bierhaus, LAM Benner, C Hartzell, P Hayne, J Hopkins, R Jedicke, L LeCorre, et al. Janus: A nasa simplex mission to explore two neo binary asteroids. LPI, (2326):1965, 2020.
- [17] GD Cassini. Traité de l’origine et du progrès de l’astronomie. Paris (1693).
- [18] Peter Goldreich and Stanton J Peale. The dynamics of planetary rotations. Annual Review of Astronomy and Astrophysics, 6(1):287–320, 1968.
- [19] GJ Cloutier. Stable rotation states of dual-spin spacecraft. Journal of Spacecraft and Rockets, 5(4):490–492, 1968.
- [20] Andrzej J Maciejewski. Reduction, relative equilibria and potential in the two rigid bodies problem. Celestial Mechanics and Dynamical Astronomy, 63(1):1–28, 1995.
- [21] Derek C Richardson, William F Bottke Jr, and Stanley G Love. Tidal distortion and disruption of earth-crossing asteroids. Icarus, 134(1):47–76, 1998.
- [22] Kevin J Walsh and Derek C Richardson. Binary near-earth asteroid formation: Rubble pile model of tidal disruptions. Icarus, 180(1):201–216, 2006.
- [23] Robert A Werner and Daniel J Scheeres. Mutual potential of homogeneous polyhedra. Celestial Mechanics and Dynamical Astronomy, 91(3-4):337–349, 2005.
- [24] Eugene G Fahnestock and Daniel J Scheeres. Simulation of the full two rigid body problem using polyhedral mutual potential and potential derivatives approach. Celestial Mechanics and Dynamical Astronomy, 96(3-4):317–339, 2006.
- [25] Pasquale Tricarico. Figure–figure interaction between bodies having arbitrary shapes and mass distributions: a power series expansion approach. Celestial Mechanics and Dynamical Astronomy, 100(4):319–330, 2008.
- [26] Joshua Ashenberg. Mutual gravitational potential and torque of solid bodies via inertia integrals. Celestial Mechanics and Dynamical Astronomy, 99(2):149–159, 2007.

- [27] Gwenaél Boué and Jacques Laskar. Spin axis evolution of two interacting bodies. *Icarus*, 201(2):750–767, 2009.
- [28] Xiyun Hou, Daniel J Scheeres, and Xiaosheng Xin. Mutual potential between two rigid bodies with arbitrary shapes and mass distributions. *Celestial Mechanics and Dynamical Astronomy*, pages 1–27, 2016.
- [29] Alex B. Davis. General use binary asteroid simulator: <https://github.com/alex-b-davis/gubas>, August 2019.
- [30] Seth A Jacobson and Daniel J Scheeres. Dynamics of rotationally fissioned asteroids: Source of observed small asteroid systems. *Icarus*, 214(1):161–178, 2011.
- [31] Daniel Jay Scheeres. Rotational fission of contact binary asteroids. *Icarus*, 189(2):370–385, 2007.
- [32] Paul Sánchez and Daniel J Scheeres. Disruption patterns of rotating self-gravitating aggregates: A survey on angle of friction and tensile strength. *Icarus*, 271:453–471, 2016.
- [33] Petr Pravec, Marek Wolf, and Lenka Šarounová. Lightcurves of 26 near-earth asteroids. *Icarus*, 136(1):124–153, 1998.
- [34] Petr Pravec and Alan W Harris. Fast and slow rotation of asteroids. *Icarus*, 148(1):12–20, 2000.
- [35] LAG Boldrin, DJ Scheeres, and OC Winter. Dynamics of rotationally fissioned asteroids: non-planar case. *Monthly Notices of the Royal Astronomical Society*, 461(4):3982–3992, 2016.
- [36] David Jewitt, Jessica Agarwal, Jing Li, Harold Weaver, Max Mutchler, and Stephen Larson. Anatomy of an asteroid breakup: the case of p/2013 r3. *The Astronomical Journal*, 153(5):223, 2017.
- [37] Akira Fujiwara, J Kawaguchi, DK Yeomans, M Abe, T Mukai, T Okada, J Saito, H Yano, M Yoshikawa, DJ Scheeres, et al. The rubble-pile asteroid itokawa as observed by hayabusa. *Science*, 312(5778):1330–1334, 2006.
- [38] Lance AM Benner, J Margot, MC Nolan, JD Giorgini, M Brozovic, DJ Scheeres, C Magri, and SJ Ostro. Radar imaging and a physical model of binary asteroid 65803 didymos. In *Bulletin of the American Astronomical Society*, volume 42, page 1056, 2010.
- [39] Patrick A Taylor, Brian D Warner, Christopher Magri, Alessondra Springmann, Michael C Nolan, Ellen S Howell, Kevin J Miller, Luisa F Zambrano-Marin, James E Richardson, Melissa Hannan, et al. The smallest binary asteroid? the discovery of equal-mass binary 1994 cj1. In *AAS/Division for Planetary Sciences Meeting Abstracts# 46*, volume 46, 2014.
- [40] Patrick A Taylor, Marina Brozovic, Joseph S Jao, Shantanu Naidu, Lance Benner, Flaviane C Venditti, Sean E Marshall, Anne Virkki, Amber Bonsall, Frank G Ghigo, et al. Radar and optical observations of equal-mass binary near-earth asteroid 2017 ye5. In *AAS/Division for Planetary Sciences Meeting Abstracts*, volume 50, 2018.
- [41] Simon Tardivel, Paul Sánchez, and Daniel J Scheeres. Equatorial cavities on asteroids, an evidence of fission events. *Icarus*, 304:192–208, 2018.

- [42] Yu Takahashi, Michael W Busch, and Daniel J Scheeres. Spin state and moment of inertia characterization of 4179 toutatis. The Astronomical Journal, 146(4):95, 2013.
- [43] Anton I Ermakov, Maria T Zuber, David E Smith, Carol A Raymond, Georges Balmino, Roger R Fu, and Boris A Ivanov. Constraints on vesta’s interior structure using gravity and shape models from the dawn mission. Icarus, 240:146–160, 2014.
- [44] DJ Scheeres, SG Hesar, S Tardivel, M Hirabayashi, D Farnocchia, JW McMahan, SR Chesley, O Barnouin, RP Binzel, WF Bottke, et al. The geophysical environment of bennu. Icarus, 276:116–140, 2016.
- [45] DS Lauretta, CW Hergenrother, SR Chesley, JM Leonard, JY Pelgrift, CD Adam, M Al Asad, PG Antreasian, R-L Ballouz, KJ Becker, et al. Episodes of particle ejection from the surface of the active asteroid (101955) bennu. Science, 366(6470), 2019.
- [46] DJ Scheeres, AS French, JW McMahan, AB Davis, DN Brack, JM Leonard, Peter Antreasian, Marina Brozovic, SR Chesley, Davide Farnocchia, et al. Osiris-*rex* gravity field estimates for bennu using spacecraft and natural particle tracking data. 2019.
- [47] Julie Bellerose and Daniel J Scheeres. Restricted full three-body problem: application to binary system 1999 kw4. Journal of guidance, control, and dynamics, 31(1):162–171, 2008.
- [48] L Dell’Elce, N Baresi, SP Naidu, LAM Benner, and DJ Scheeres. Numerical investigation of the dynamical environment of 65803 didymos. Advances in Space Research, 59(5):1304–1320, 2017.
- [49] Loic Chappaz and Kathleen C Howell. Exploration of bounded motion near binary systems comprised of small irregular bodies. Celestial Mechanics and Dynamical Astronomy, 123(2):123–149, 2015.
- [50] Jinglang Feng and Xiyun Hou. Dynamics of equilibrium points in a uniformly rotating second-order and degree gravitational field. The Astronomical Journal, 154(1):21, 2017.
- [51] HF Agrusaa, DC Richardson, AB Davis, E Fahnestock, M Hirabayashi, Chabot NL, Cheng AF, Rivkin AS, Michel P, and DART Dynamics Working Group. A simulation benchmarking and sensitivity study of the full two-body gravitational dynamics of the dart mission target, binary asteroid 65803 didymos. Icarus, In Revisions.
- [52] Taeyoung Lee, Melvin Leok, and N Harris McClamroch. Lie group variational integrators for the full body problem in orbital mechanics. Celestial Mechanics and Dynamical Astronomy, 98(2):121–144, 2007.
- [53] HF Agrusa, DC Richardson, AB Davis, E Fahnestock, M Hirabayashi, NL Chabot, AF Change, AS Rivkin, P Michel, and DART Dynamics Working Group. A simulation benchmarking and sensitivity study of the full two-body gravitational dynamics of the dart mission target, binary asteroid 65803 didymos. Icarus, 2020.
- [54] DJ Scheeres. Minimum energy configurations in the n-body problem and the celestial mechanics of granular systems. Celestial Mechanics and Dynamical Astronomy, 113(3):291–320, 2012.

- [55] Marc W Buie, Catherine B Olkin, William J Merline, Kevin J Walsh, Harold F Levison, Brad Timerson, Dave Herald, William M Owen Jr, Harry B Abramson, Katherine J Abramson, et al. Size and shape from stellar occultation observations of the double jupiter trojan patroclus and menoitius. The Astronomical Journal, 149(3):113, 2015.
- [56] DJ Scheeres. Relative equilibria for general gravity fields in the sphere-restricted full 2-body problem. Celestial Mechanics and Dynamical Astronomy, 94(3):317–349, 2006.
- [57] GERARD Gómez. Dynamics and Mission Design Near Libration Points. Vol. 1. Fundamentals: the Case of Collinear Libration Points (World scientific monograph series in mathematics; vol. 2). World Scientific, 2001.
- [58] Zubin P Olikara and Kathleen C Howell. Computation of quasi-periodic invariant tori in the restricted three-body problem. Paper No. AAS, pages 1–15, 2010.
- [59] Fabio Ferrari, Alessandro Tasora, Pierangelo Masarati, and Michèle Lavagna. N-body gravitational and contact dynamics for asteroid aggregation. Multibody System Dynamics, 39(1):3–20, Jan 2017.
- [60] Carl D Murray and Stanley F Dermott. Solar system dynamics. Cambridge university press, 1999.
- [61] P Goldreich and T Gold. On the eccentricity of satellite orbits in the solar system. Monthly Notices of the Royal Astronomical Society, 126(3):257–268, 1963.
- [62] KA Holsapple. Equilibrium configurations of solid cohesionless bodies. Icarus, 154(2):432–448, 2001.
- [63] Keith A Holsapple. Equilibrium figures of spinning bodies with self-gravity. Icarus, 172(1):272–303, 2004.
- [64] Paul Sánchez and Daniel J Scheeres. The strength of regolith and rubble pile asteroids. Meteoritics & Planetary Science, 49(5):788–811, 2014.
- [65] Peter J Prince and John R Dormand. High order embedded runge-kutta formulae. Journal of Computational and Applied Mathematics, 7(1):67–75, 1981.
- [66] DJ Scheeres. Stability of binary asteroids. Icarus, 159(2):271–283, 2002.
- [67] Alan W Harris. On the slow rotation of asteroids. Icarus, 156(1):184–190, 2002.
- [68] DJ Scheeres. Changes in rotational angular momentum due to gravitational interactions between two finite bodies. Celestial Mechanics and Dynamical Astronomy, 81(1-2):39–44, 2001.
- [69] David Polishook and Oded Aharonson. Surface slopes of asteroid pairs as indicators of mechanical properties and cohesion. arXiv preprint arXiv:1904.09627, 2019.
- [70] DJ Scheeres, JW McMahon, AS French, DN Brack, SR Chesley, D Farnocchia, Y Takahashi, JM Leonard, J Geeraert, B Page, et al. The dynamic geophysical environment of (101955) bennu based on osiris-rex measurements. Nature Astronomy, 3(4):352, 2019.

- [71] Seiichiro Watanabe, M Hirabayashi, N Hirata, Na Hirata, R Noguchi, Y Shimaki, H Ikeda, E Tatsumi, M Yoshikawa, S Kikuchi, et al. Hayabusa2 arrives at the carbonaceous asteroid 162173 ryugu—a spinning top-shaped rubble pile. *Science*, 364(6437):268–272, 2019.
- [72] Kevin J Walsh, Derek C Richardson, and Patrick Michel. Spin-up of rubble-pile asteroids: Disruption, satellite formation, and equilibrium shapes. *Icarus*, 220(2):514–529, 2012.
- [73] Daniel J Scheeres. Orbital motion in strongly perturbed environments: applications to asteroid, comet and planetary satellite orbiters. Springer, 2016.
- [74] Francis Nimmo, Orkan Umurhan, Carey M Lisse, Carver J Bierson, Tod R Lauer, Marc W Buie, Henry B Throop, Josh A Kammer, James H Roberts, William B McKinnon, et al. Mean radius and shape of pluto and charon from new horizons images. *Icarus*, 287:12–29, 2017.
- [75] Bob Schutz, Byron Tapley, and George H Born. Statistical orbit determination. Academic Press, 2004.
- [76] Aim didymos reference document, v. 10. 10 2015.

Appendix A

Full Two-Body Problem Partial Matrices

A.1 Planar Dynamics Matrix

$$\vec{X} = \left[r \quad \theta \quad \phi_1 \quad \phi_2 \quad \dot{r} \quad \dot{\theta} \quad \dot{\phi}_1 \quad \dot{\phi}_2 \right]^T \quad (\text{A.1})$$

$$\dot{\vec{X}} = \mathbf{A}\vec{X} = \begin{bmatrix} 0 & 0 & 0 & 0 & 1 & 0 & 0 & 0 \\ 0 & 0 & 0 & 0 & 0 & 1 & 0 & 0 \\ 0 & 0 & 0 & 0 & 0 & 0 & 1 & 0 \\ 0 & 0 & 0 & 0 & 0 & 0 & 0 & 1 \\ \frac{\partial \ddot{r}}{\partial r} & 0 & \frac{\partial \ddot{r}}{\partial \phi_1} & \frac{\partial \ddot{r}}{\partial \phi_2} & 0 & \frac{\partial \ddot{r}}{\partial \dot{r}} & 0 & 0 \\ \frac{\partial \ddot{\theta}}{\partial r} & 0 & \frac{\partial \ddot{\theta}}{\partial \phi_1} & \frac{\partial \ddot{\theta}}{\partial \phi_2} & \frac{\partial \ddot{\theta}}{\partial \dot{r}} & \frac{\partial \ddot{\theta}}{\partial \dot{\theta}} & 0 & 0 \\ \frac{\partial \ddot{\phi}_1}{\partial r} & 0 & \frac{\partial \ddot{\phi}_1}{\partial \phi_1} & \frac{\partial \ddot{\phi}_1}{\partial \phi_2} & \frac{\partial \ddot{\phi}_1}{\partial \dot{r}} & \frac{\partial \ddot{\phi}_1}{\partial \dot{\theta}} & 0 & 0 \\ \frac{\partial \ddot{\phi}_2}{\partial r} & 0 & \frac{\partial \ddot{\phi}_2}{\partial \phi_1} & \frac{\partial \ddot{\phi}_2}{\partial \phi_2} & \frac{\partial \ddot{\phi}_2}{\partial \dot{r}} & \frac{\partial \ddot{\phi}_2}{\partial \dot{\theta}} & 0 & 0 \end{bmatrix} \begin{bmatrix} r \\ \theta \\ \phi_1 \\ \phi_2 \\ \dot{r} \\ \dot{\theta} \\ \dot{\phi}_1 \\ \dot{\phi}_2 \end{bmatrix} \quad (\text{A.2})$$

$$\frac{\partial \ddot{r}}{\partial r} = \dot{\theta}^2 - \frac{V_{rr}}{m} \quad (\text{A.3})$$

$$\frac{\partial \ddot{r}}{\partial \phi_1} = -\frac{V_{r\phi_1}}{m} \quad (\text{A.4})$$

$$\frac{\partial \ddot{r}}{\partial \phi_2} = -\frac{V_{r\phi_2}}{m} \quad (\text{A.5})$$

$$\frac{\partial \ddot{r}}{\partial \dot{\theta}} = 2\dot{\theta}r \quad (\text{A.6})$$

$$\frac{\partial \ddot{\theta}}{\partial r} = -2\frac{V_{\phi_1}}{mr^3} + \frac{V_{\phi_1}}{mr^2} - 2\frac{V_{\phi_2}}{mr^3} + \frac{V_{\phi_2}}{mr^2} + 2\frac{\dot{r}\dot{\theta}}{r^2} \quad (\text{A.7})$$

$$\frac{\partial \ddot{\theta}}{\partial \phi_1} = \frac{V_{\phi_1\phi_1}}{mr^2} \quad (\text{A.8})$$

$$\frac{\partial \ddot{\theta}}{\partial \phi_2} = \frac{V_{\phi_2\phi_2}}{mr^2} \quad (\text{A.9})$$

$$\frac{\partial \ddot{\theta}}{\partial \dot{r}} = -2\frac{\dot{\theta}}{r} \quad (\text{A.10})$$

$$\frac{\partial \ddot{\theta}}{\partial \dot{\theta}} = -2\frac{\dot{r}}{r} \quad (\text{A.11})$$

$$\frac{\partial \ddot{\phi}_1}{\partial r} = 2\frac{(V_{\phi_1} + V_{\phi_2})}{mr^3} - \frac{(V_{r\phi_1} + V_{r\phi_2})}{mr^2} - \frac{V_{r\phi_1}}{M_A I_{A,zz}} - 2\frac{\dot{r}\dot{\theta}}{r^2} \quad (\text{A.12})$$

$$\frac{\partial \ddot{\phi}_1}{\partial \phi_1} = -\frac{V_{\phi_1\phi_1}}{mr^2} - \frac{V_{\phi_1\phi_1}}{M_A I_{A,zz}} \quad (\text{A.13})$$

$$\frac{\partial \ddot{\phi}_1}{\partial \phi_2} = -\frac{V_{\phi_2\phi_2}}{mr^2} \quad (\text{A.14})$$

$$\frac{\partial \ddot{\phi}_1}{\partial \dot{r}} = 2\frac{\dot{\theta}}{r} \quad (\text{A.15})$$

$$\frac{\partial \ddot{\phi}_1}{\partial \dot{\theta}} = 2\frac{\dot{r}}{r} \quad (\text{A.16})$$

$$\frac{\partial \ddot{\phi}_2}{\partial r} = 2\frac{(V_{\phi_1} + V_{\phi_2})}{mr^3} - \frac{(V_{r\phi_1} + V_{r\phi_2})}{mr^2} - \frac{V_{r\phi_2}}{M_B I_{B,zz}} - 2\frac{\dot{r}\dot{\theta}}{r^2} \quad (\text{A.17})$$

$$\frac{\partial \ddot{\phi}_2}{\partial \phi_1} = -\frac{V_{\phi_1\phi_1}}{mr^2} \quad (\text{A.18})$$

$$\frac{\partial \ddot{\phi}_2}{\partial \phi_2} = -\frac{V_{\phi_2 \phi_2}}{mr^2} - \frac{V_{\phi_2 \phi_2}}{M_B I_{B,zz}} \quad (\text{A.19})$$

$$\frac{\partial \ddot{\phi}_2}{\partial \dot{r}} = 2\frac{\dot{\theta}}{r} \quad (\text{A.20})$$

$$\frac{\partial \ddot{\phi}_2}{\partial \dot{\theta}} = 2\frac{\dot{r}}{r} \quad (\text{A.21})$$

For second order inertia tensor formulation of mutual potential, partials of the potential are as follows:

$$\begin{aligned} V_r = \frac{GM_A M_B}{r^2} & \left(1 + \frac{3}{2r^2} (I_{A,xx} + I_{A,yy} + I_{A,zz} + I_{B,xx} + I_{B,yy} + I_{B,zz} \right. \\ & - \frac{3}{2} (I_{A,xx} + I_{A,yy} - \cos(2\phi_1) (I_{A,yy} - I_{A,xx}) + I_{B,xx} + I_{B,yy} \\ & \left. - \cos(2\phi_2) (I_{B,yy} - I_{B,xx})) \right) \end{aligned} \quad (\text{A.22})$$

$$V_{\phi_1} = 3 \frac{GM_A M_B}{2r^3} \sin(2\phi_1) (I_{A,yy} - I_{A,xx}) \quad (\text{A.23})$$

$$V_{\phi_2} = 3 \frac{GM_A M_B}{2r^3} \sin(2\phi_2) (I_{B,yy} - I_{B,xx}) \quad (\text{A.24})$$

$$\begin{aligned} V_{rr} = 2 \frac{GM_A M_B}{r^3} - 6 \frac{GM_A M_B}{r^5} & (I_{A,xx} + I_{A,yy} + I_{A,zz} + I_{B,xx} + I_{B,yy} + I_{B,zz} \\ & - \frac{3}{2} (I_{A,xx} + I_{A,yy} - \cos(2\phi_1) (I_{A,yy} - I_{A,xx}) + I_{B,xx} + I_{B,yy} \\ & - \cos(2\phi_2) (I_{B,yy} - I_{B,xx})) \end{aligned} \quad (\text{A.25})$$

$$V_{r\phi_1} = -9 \frac{GM_A M_B}{2r^4} \sin(2\phi_1) (I_{A,yy} - I_{A,xx}) \quad (\text{A.26})$$

$$V_{r\phi_2} = -9 \frac{GM_A M_B}{2r^4} \sin(2\phi_2) (I_{B,yy} - I_{B,xx}) \quad (\text{A.27})$$

$$V_{\phi_1 \phi_1} = 3 \frac{GM_A M_B}{r^3} \cos(2\phi_1) (I_{A,yy} - I_{A,xx}) \quad (\text{A.28})$$

$$V_{\phi_2 \phi_2} = 3 \frac{GM_A M_B}{r^3} \cos(2\phi_2) (I_{B,yy} - I_{B,xx}) \quad (\text{A.29})$$

A.2 Nonplanar Dynamics Matrix

Within this section we add the notation $(-)^s$ to denote a skew-symmetric matrix operator in addition to the previous tilde notation.

$$\mathbf{A} = \begin{bmatrix} 0_3 & 0_3 & 0_3 & 0_3 & 0_3 & 0_3 \\ 0_3 & \frac{\partial \dot{\vec{\theta}}_1}{\partial \theta_1} & 0_3 & 0_3 & B_1 & 0_3 \\ 0_3 & 0_3 & \frac{\partial \dot{\vec{\theta}}_2}{\partial \theta_2} & 0_3 & 0_3 & B_2 \\ \frac{\partial \vec{R}}{\partial \vec{r}} & 0_3 & \frac{\partial \vec{r}}{\partial \theta_2} & \frac{\partial \vec{r}}{\partial \vec{r}} & \frac{\partial \vec{r}}{\partial \vec{\omega}_1} & 0_3 \\ \frac{\partial \dot{\vec{\omega}}_1}{\partial \vec{r}} & 0_3 & \frac{\partial \dot{\vec{\omega}}_1}{\partial \theta_2} & 0_3 & \frac{\partial \dot{\vec{\omega}}_1}{\partial \vec{\omega}_1} & 0_3 \\ \frac{\partial \dot{\vec{\omega}}_2}{\partial \vec{r}} & 0_3 & \frac{\partial \dot{\vec{\omega}}_2}{\partial \theta_2} & 0_3 & \frac{\partial \dot{\vec{\omega}}_2}{\partial \vec{\omega}_1} & \frac{\partial \dot{\vec{\omega}}_2}{\partial \vec{\omega}_2} \end{bmatrix} \quad (\text{A.30})$$

$$\frac{\partial \vec{M}_B}{\partial \vec{r}} = -\vec{\alpha}^s \frac{\partial^2 U}{\partial \vec{\alpha} \partial \vec{r}} - \vec{\beta}^s \frac{\partial^2 U}{\partial \vec{\beta} \partial \vec{r}} - \vec{\gamma}^s \frac{\partial^2 U}{\partial \vec{\gamma} \partial \vec{r}} \quad (\text{A.31})$$

$$\begin{aligned} \frac{\partial \vec{M}_B}{\partial \vec{\theta}_2} &= \left(\frac{\partial U}{\partial \vec{\alpha}} \right)^s \frac{\partial \vec{\alpha}}{\partial \vec{\theta}_2} + \left(\frac{\partial U}{\partial \vec{\beta}} \right)^s \frac{\partial \vec{\beta}}{\partial \vec{\theta}_2} + \left(\frac{\partial U}{\partial \vec{\gamma}} \right)^s \frac{\partial \vec{\gamma}}{\partial \vec{\theta}_2} \\ &\quad - \vec{\alpha}^s \left(\vec{\alpha}^s \frac{\partial^2 U}{\partial \vec{\alpha}^2} + \vec{\beta}^s \frac{\partial^2 U}{\partial \vec{\alpha} \partial \vec{\beta}} + \vec{\gamma}^s \frac{\partial^2 U}{\partial \vec{\alpha} \partial \vec{\gamma}} \right) \\ &\quad - \vec{\beta}^s \left(\vec{\alpha}^s \frac{\partial^2 U}{\partial \vec{\beta} \partial \vec{\alpha}} + \vec{\beta}^s \frac{\partial^2 U}{\partial \vec{\beta}^2} + \vec{\gamma}^s \frac{\partial^2 U}{\partial \vec{\beta} \partial \vec{\gamma}} \right) \\ &\quad - \vec{\gamma}^s \left(\vec{\alpha}^s \frac{\partial^2 U}{\partial \vec{\gamma} \partial \vec{\alpha}} + \vec{\beta}^s \frac{\partial^2 U}{\partial \vec{\gamma} \partial \vec{\beta}} + \vec{\gamma}^s \frac{\partial^2 U}{\partial \vec{\gamma}^2} \right) \end{aligned} \quad (\text{A.32})$$

$$\frac{\partial \vec{M}_A}{\partial \vec{r}} = - \left(\frac{\partial U}{\partial \vec{r}} \right)^s + \vec{r}^s \frac{\partial^2 U}{\partial \vec{r}^2} - \frac{\partial \vec{M}_B}{\partial \vec{r}} \quad (\text{A.33})$$

$$\frac{\partial \vec{M}_A}{\partial \vec{\theta}_2} = \vec{r}^s \left(\vec{\alpha}^s \frac{\partial^2 U}{\partial \vec{\alpha} \partial \vec{r}} + \vec{\beta}^s \frac{\partial^2 U}{\partial \vec{\beta} \partial \vec{r}} + \vec{\gamma}^s \frac{\partial^2 U}{\partial \vec{\gamma} \partial \vec{r}} \right) - \frac{\partial \vec{M}_B}{\partial \vec{\theta}_2} \quad (\text{A.34})$$

$$\frac{\partial \dot{\vec{\theta}}_1}{\partial \vec{\theta}_1} = \frac{\partial B_1}{\partial \vec{\theta}_1} \vec{\omega}_1 \quad (\text{A.35})$$

$$\frac{\partial \dot{\vec{\theta}}_2}{\partial \vec{\theta}_2} = \frac{\partial B_2}{\partial \vec{\theta}_2} \vec{\omega}_2 \quad (\text{A.36})$$

$$\frac{\partial \ddot{\vec{r}}}{\partial \vec{r}} = \vec{r}^s \mathbf{I}_A^{-1} \frac{\partial \vec{M}_A}{\partial \vec{r}} - \left(\mathbf{I}_A^{-1} \left(\mathbf{I}_A \vec{\omega}_1 \vec{\omega}_1^s + M_A \right) \right)^s - \vec{\omega}_1^s \vec{\omega}_1^s - \frac{1}{m} \frac{\partial^2 U}{\partial \vec{r}^2} \quad (\text{A.37})$$

$$\frac{\partial \ddot{\vec{r}}}{\partial \vec{\theta}_2} = \vec{r}^s \mathbf{I}_A^{-1} \frac{\partial \vec{M}_A}{\partial \vec{\theta}_2} - \left(\vec{\alpha}^s \frac{\partial^2 U}{\partial \vec{\alpha} \partial \vec{r}} + \vec{\beta}^s \frac{\partial^2 U}{\partial \vec{\beta} \partial \vec{r}} + \vec{\gamma}^s \frac{\partial^2 U}{\partial \vec{\gamma} \partial \vec{r}} \right) \quad (\text{A.38})$$

$$\frac{\partial \ddot{\vec{r}}}{\partial \vec{r}} = -2\vec{\omega}_1^s \quad (\text{A.39})$$

$$\frac{\partial \ddot{\vec{r}}}{\partial \vec{\omega}_1} = \vec{r}^s \mathbf{I}_A^{-1} \left(\left(\mathbf{I}_A \vec{\omega}_1 \right)^s - \vec{\omega}_1^s \mathbf{I}_A \right) + 2 \dot{\vec{r}}^s + \left(\vec{\omega}_1^s \vec{r} \right)^s + \vec{\omega}_1^s \vec{r}^s \quad (\text{A.40})$$

$$\frac{\partial \dot{\vec{\omega}}_1}{\partial \vec{r}} = \mathbf{I}_A^{-1} \frac{\partial \vec{M}_A}{\partial \vec{r}} \quad (\text{A.41})$$

$$\frac{\partial \dot{\vec{\omega}}_1}{\partial \vec{\theta}_2} = \mathbf{I}_A^{-1} \frac{\partial \vec{M}_A}{\partial \vec{\theta}_2} \quad (\text{A.42})$$

$$\frac{\partial \dot{\vec{\omega}}_1}{\partial \vec{\omega}_1} = \mathbf{I}_A^{-1} \left(\mathbf{I}_A \vec{\omega}_1 \vec{\omega}_1^s \mathbf{I}_A \right)^s \quad (\text{A.43})$$

$$\frac{\partial \dot{\vec{\omega}}_2}{\partial \vec{r}} = \mathbf{I}_B^{-1} \frac{\partial \vec{M}_B}{\partial \vec{r}} \quad (\text{A.44})$$

$$\begin{aligned} \frac{\partial \dot{\vec{\omega}}_2}{\partial \vec{\theta}_2} &= \mathbf{I}_B \left(\vec{\omega}_1 + \vec{\omega}_2 \right) \vec{\omega}_1^s \frac{\partial \mathbf{I}_B^{-1}}{\partial \vec{\theta}_2} + \mathbf{I}_B^{-1} \left(-\vec{\omega}_1^s \left(\vec{\omega}_1 + \vec{\omega}_2 \right) \frac{\partial \mathbf{I}_B}{\partial \vec{\theta}_2} + \right. \\ &\quad \left. \frac{\partial \vec{M}_A}{\partial \vec{\theta}_2} - \left(\vec{\omega}_1 + \vec{\omega}_2 \right) \frac{\partial \dot{\mathbf{I}}_B}{\partial \vec{\theta}_2} \right) \\ &\quad + \vec{M}_B \frac{\partial \mathbf{I}_B^{-1}}{\partial \vec{\theta}_2} - \dot{\mathbf{I}}_B \left(\vec{\omega}_1 + \vec{\omega}_2 \right) \frac{\partial \mathbf{I}_B^{-1}}{\partial \vec{\theta}_2} - \mathbf{I}_A^{-1} \frac{\partial \vec{M}_A}{\partial \vec{\theta}_2} \end{aligned} \quad (\text{A.45})$$

$$\frac{\partial \dot{\vec{\omega}}_2}{\partial \vec{\omega}_1} = \mathbf{I}_B^{-1} \left(\mathbf{I}_B \left(\vec{\omega}_1 + \vec{\omega}_2 \right)^s - \vec{\omega}_1^s \mathbf{I}_B - \dot{\mathbf{I}}_B \right) + \mathbf{I}_A^{-1} \left(\vec{\omega}_1^s \mathbf{I}_A - \left(\mathbf{I}_A \vec{\omega}_1 \right)^s \right) \quad (\text{A.46})$$

$$\frac{\partial \dot{\vec{\omega}}_2}{\partial \vec{\omega}_2} = \mathbf{I}_B^{-1} \left(-\vec{\omega}_1^s \mathbf{I}_B - \dot{\mathbf{I}}_B + \left(\vec{\omega}_1 + \vec{\omega}_2 \right) \frac{\partial \dot{\mathbf{I}}_B}{\partial \vec{\omega}_2} \right) \quad (\text{A.47})$$

A.3 Total Mass Partial of Nonplanar Dynamics Matrix

Partials of A with respect to M_T

$$\begin{aligned} \frac{\partial^2 \ddot{\vec{r}}}{\partial \vec{r} \partial M_T} &= \vec{r}^s \frac{\partial \mathbf{I}_A^{-1}}{\partial M_T} \frac{\partial \vec{M}_A}{\partial \vec{r}} + \mathbf{I}_A^{-1} \frac{\partial^2 \vec{M}_A}{\partial \vec{r} \partial M_T} \\ &- \left(\frac{\partial \mathbf{I}_A^{-1}}{\partial M_T} \mathbf{I}_A \vec{\omega}_1 \vec{\omega}_1^s + \mathbf{I}_A^{-1} \frac{\partial \mathbf{I}_A}{\partial M_T} \vec{\omega}_1 \vec{\omega}_1^s \frac{\partial \mathbf{I}_A^{-1}}{\partial M_T} \vec{M}_A + \mathbf{I}_A^{-1} \frac{\partial \vec{M}_A}{\partial M_T} \right)^s \\ &+ \frac{1}{M_T(\mu - \mu^2)} \frac{\partial^2 U}{\partial \vec{r}^2} - \frac{1}{m} \frac{\partial^3 U}{\partial \vec{r}^2 \partial M_T} \end{aligned} \quad (\text{A.48})$$

$$\begin{aligned} \frac{\partial^2 \ddot{\vec{r}}}{\partial \vec{\theta}_2 \partial M_T} &= \vec{r}^s \left(\frac{\partial \mathbf{I}_A^{-1}}{\partial M_T} \frac{\partial \vec{M}_A}{\partial \vec{\theta}_2} + \mathbf{I}_A^{-1} \frac{\partial^2 \vec{M}_A}{\partial \vec{\theta}_2 \partial M_T} \right) \\ &+ \frac{1}{M_T(\mu - \mu^2)} \frac{\partial^2 U}{\partial \vec{r} \partial \vec{\theta}_2} - \frac{1}{m} \frac{\partial^3 U}{\partial \vec{r} \partial \vec{\theta}_2 \partial M_T} \end{aligned} \quad (\text{A.49})$$

$$\begin{aligned} \frac{\partial^2 \ddot{\vec{r}}}{\partial \vec{\omega}_1 \partial M_T} &= \vec{r}^s \left(\frac{\partial \mathbf{I}_A^{-1}}{\partial M_T} \left(\mathbf{I}_A \vec{\omega}_1 \right)^s + \mathbf{I}_A^{-1} \left(\frac{\partial \mathbf{I}_A^{-1}}{\partial M_T} \vec{\omega}_1 \right)^s - \frac{\partial \mathbf{I}_A^{-1}}{\partial M_T} \vec{\omega}_1^s \mathbf{I}_A \right. \\ &\quad \left. - \mathbf{I}_A^{-1} \vec{\omega}_1^s \frac{\partial \mathbf{I}_A}{\partial M_T} \right) \end{aligned} \quad (\text{A.50})$$

$$\frac{\partial^2 \dot{\vec{\omega}}_1}{\partial \vec{r} \partial M_T} = \frac{\partial \mathbf{I}_A^{-1}}{\partial M_T} \frac{\partial \vec{M}_A}{\partial \vec{r}} + \mathbf{I}_A^{-1} \frac{\partial^2 \vec{M}_A}{\partial \vec{r} \partial M_T} \quad (\text{A.51})$$

$$\frac{\partial^2 \dot{\vec{\omega}}_1}{\partial \vec{\theta}_2 \partial M_T} = \frac{\partial \mathbf{I}_A^{-1}}{\partial M_T} \frac{\partial \vec{M}_A}{\partial \vec{\theta}_2} + \mathbf{I}_A^{-1} \frac{\partial^2 \vec{M}_A}{\partial \vec{\theta}_2 \partial M_T} \quad (\text{A.52})$$

$$\begin{aligned} \frac{\partial^2 \dot{\vec{\omega}}_1}{\partial \vec{\omega}_1 \partial M_T} &= \frac{\partial \mathbf{I}_A^{-1}}{\partial M_T} \left(\mathbf{I}_A \vec{\omega}_1 \right)^s + \mathbf{I}_A^{-1} \left(\frac{\partial \mathbf{I}_A}{\partial M_T} \vec{\omega}_1 \right)^s \\ &- \frac{\partial \mathbf{I}_A^{-1}}{\partial M_T} \vec{\omega}_1^s \mathbf{I}_A - \mathbf{I}_A^{-1} \vec{\omega}_1^s \frac{\partial \mathbf{I}_A}{\partial M_T} \end{aligned} \quad (\text{A.53})$$

$$\frac{\partial^2 \dot{\vec{\omega}}_2}{\partial \vec{r} \partial M_T} = \frac{\partial \mathbf{I}_B^{-1}}{\partial M_T} \frac{\partial \vec{M}_B}{\partial \vec{r}} + \mathbf{I}_B^{-1} \frac{\partial^2 \vec{M}_B}{\partial \vec{r} \partial M_T} - \frac{\partial \mathbf{I}_A^{-1}}{\partial M_T} \frac{\partial \vec{M}_A}{\partial \vec{r}} - \mathbf{I}_A^{-1} \frac{\partial^2 \vec{M}_A}{\partial \vec{r} \partial M_T} \quad (\text{A.54})$$

$$\begin{aligned}
\frac{\partial^2 \ddot{\omega}_2}{\partial \vec{\theta}_2 \partial M_T} &= \frac{\partial \mathbf{I}_B}{\partial M_T} (\vec{\omega}_1 + \vec{\omega}_2) \vec{\omega}_1^s \frac{\partial \mathbf{I}_B^{-1}}{\partial \vec{\theta}_2} + \mathbf{I}_B (\vec{\omega}_1 + \vec{\omega}_2) \vec{\omega}_1^s \frac{\partial^2 \mathbf{I}_B^{-1}}{\partial \vec{\theta}_2 \partial M_T} \\
&- \frac{\partial \mathbf{I}_B}{\partial M_T} \vec{\omega}_1^s (\vec{\omega}_1 + \vec{\omega}_2) \frac{\partial^2 \mathbf{I}_B}{\partial \vec{\theta}_2 \partial M_T} + \frac{\partial \vec{M}_B}{\partial M_T} \frac{\partial \mathbf{I}_B^{-1}}{\partial \vec{\theta}_2} + \vec{M}_B \frac{\partial^2 \mathbf{I}_B^{-1}}{\partial \vec{\theta}_2 \partial M_T} \\
&- \frac{\partial \mathbf{I}_B^{-1}}{\partial M_T} \frac{\partial \vec{M}_B}{\partial \vec{\theta}_2} - \mathbf{I}_B^{-1} \frac{\partial^2 \vec{M}_B}{\partial \vec{\theta}_2 \partial M_T} - \frac{\partial \dot{\mathbf{I}}_B}{\partial M_T} (\vec{\omega}_1 + \vec{\omega}_2) \frac{\partial \mathbf{I}_B^{-1}}{\partial \vec{\theta}_2} \\
&- \dot{\mathbf{I}}_B (\vec{\omega}_1 + \vec{\omega}_2) \frac{\partial^2 \mathbf{I}_B^{-1}}{\partial \vec{\theta}_2 \partial M_T} - \frac{\partial \mathbf{I}_A^{-1}}{\partial M_T} \frac{\partial \vec{M}_A}{\partial \vec{\theta}_2} - \mathbf{I}_A^{-1} \frac{\partial^2 \vec{M}_A}{\partial \vec{\theta}_2 \partial M_T} \\
&- \frac{\partial \mathbf{I}_B^{-1}}{\partial M_T} (\vec{\omega}_1 + \vec{\omega}_2) \frac{\partial \dot{\mathbf{I}}_B}{\partial \vec{\theta}_2} - \mathbf{I}_B^{-1} (\vec{\omega}_1 + \vec{\omega}_2) \frac{\partial^2 \dot{\mathbf{I}}_B}{\partial \vec{\theta}_2 \partial M_T}
\end{aligned} \tag{A.55}$$

$$\begin{aligned}
\frac{\partial^2 \ddot{\omega}_2}{\partial \vec{\omega}_1 \partial M_T} &= \frac{\partial \mathbf{I}_B^{-1}}{\partial M_T} \left(\left(\mathbf{I}_B (\vec{\omega}_1 + \vec{\omega}_2) \right)^s - \vec{\omega}_1^s \mathbf{I}_B - \dot{\mathbf{I}}_B \right) \\
&+ \mathbf{I}_B^{-1} \left(\left(\frac{\partial \mathbf{I}_B}{\partial M_T} (\vec{\omega}_1 + \vec{\omega}_2) \right)^s - \vec{\omega}_1^s \frac{\partial \mathbf{I}_B}{\partial M_T} - \frac{\partial \dot{\mathbf{I}}_B}{\partial M_T} \right) \\
&+ \frac{\partial \mathbf{I}_A^{-1}}{\partial M_T} \left(\vec{\omega}_1^s \mathbf{I}_A - \left(\mathbf{I}_A \vec{\omega}_1 \right)^s \right) + \mathbf{I}_A^{-1} \left(\vec{\omega}_1^s \frac{\partial \mathbf{I}_A}{\partial M_T} - \left(\frac{\partial \mathbf{I}_A}{\partial M_T} \vec{\omega}_1 \right)^s \right)
\end{aligned} \tag{A.56}$$

$$\begin{aligned}
\frac{\partial^2 \ddot{\omega}_2}{\partial \vec{\omega}_2 \partial M_T} &= \frac{\partial \mathbf{I}_B^{-1}}{\partial M_T} \left(-\vec{\omega}_1^s \mathbf{I}_B - \dot{\mathbf{I}}_B + (\vec{\omega}_1 + \vec{\omega}_2) \frac{\partial \dot{\mathbf{I}}_B}{\partial \vec{\omega}_2} \right) \\
&- \mathbf{I}_B^{-1} \vec{\omega}_1^s \frac{\partial \mathbf{I}_B}{\partial M_T} - \frac{\partial \dot{\mathbf{I}}_B}{\partial M_T} + (\vec{\omega}_1 + \vec{\omega}_2) \frac{\partial^2 \dot{\mathbf{I}}_B}{\partial \vec{\omega}_2 \partial M_T}
\end{aligned} \tag{A.57}$$

A.4 Second Order Inertia Integral Partial of Nonplanar Dynamics Matrix

Partials of A with respect to T_i^{jkl} , where i represents body A or B and $j, k, l = 0$ or 2 with only one index set to 2 , are needed to compute the sensitivity of the eigenvalues to the mass parameters of interest.

$$\begin{aligned}
\frac{\partial^2 \ddot{\vec{r}}}{\partial \vec{r} \partial T_i^{jkl}} &= \vec{r}^s \left(\frac{\partial \mathbf{I}_A^{-1}}{\partial T_i^{jkl}} \frac{\partial \vec{M}_A}{\partial \vec{r}} + \mathbf{I}_A^{-1} \frac{\partial^2 \vec{M}_A}{\partial \vec{r} \partial T_i^{jkl}} \right) \\
&- \left(\frac{\partial \mathbf{I}_A^{-1}}{\partial T_i^{jkl}} \mathbf{I}_A \vec{\omega}_1 \vec{\omega}_1^s + \mathbf{I}_A^{-1} \frac{\partial \mathbf{I}_A}{\partial T_i^{jkl}} \vec{\omega}_1 \vec{\omega}_1^s + \frac{\partial \mathbf{I}_A^{-1}}{\partial T_i^{jkl}} \vec{M}_A + \mathbf{I}_A^{-1} \frac{\partial \vec{M}_A}{\partial T_i^{jkl}} \right)^s \\
&- \frac{1}{m} \frac{\partial^3 U}{\partial \vec{R}^2 \partial T_i^{jkl}}
\end{aligned} \tag{A.58}$$

$$\frac{\partial^2 \ddot{\vec{r}}}{\partial \vec{\theta}_2 \partial T_i^{jkl}} = \vec{r}^s \left(\frac{\partial \mathbf{I}_A^{-1}}{\partial T_i^{jkl}} \frac{\partial \vec{M}_A}{\partial \vec{\theta}_2} + \mathbf{I}_A^{-1} \frac{\partial^2 \vec{M}_A}{\partial \vec{\theta}_2 \partial T_i^{jkl}} \right) - \frac{1}{m} \frac{\partial^3 U}{\partial \vec{\theta}_2^2 \partial T_i^{jkl}} \tag{A.59}$$

$$\begin{aligned} \frac{\partial^2 \ddot{\vec{r}}}{\partial \vec{\omega}_1 \partial T_i^{jkl}} &= \vec{r}^s \left(\frac{\partial \mathbf{I}_A^{-1}}{\partial T_i^{jkl}} \left(\mathbf{I}_A \vec{\omega}_1 \right)^s + \mathbf{I}_A^{-1} \left(\frac{\partial \mathbf{I}_A}{\partial T_i^{jkl}} \vec{\omega}_1 \right)^s \right. \\ &\quad \left. - \frac{\partial \mathbf{I}_A^{-1}}{\partial T_i^{jkl}} \vec{\omega}_1^s \mathbf{I}_A - \mathbf{I}_A^{-1} \vec{\omega}_1^s \frac{\partial \mathbf{I}_A}{\partial T_i^{jkl}} \right) \end{aligned} \quad (\text{A.60})$$

$$\frac{\partial^2 \dot{\vec{\omega}}_1}{\partial \vec{r} \partial T_i^{jkl}} = \frac{\partial \mathbf{I}_A^{-1}}{\partial T_i^{jkl}} \frac{\partial \vec{M}_A}{\partial \vec{r}} + \mathbf{I}_A^{-1} \frac{\partial^2 \vec{M}_A}{\partial \vec{r} \partial T_i^{jkl}} \quad (\text{A.61})$$

$$\frac{\partial^2 \dot{\vec{\omega}}_1}{\partial \vec{\theta}_2 \partial T_i^{jkl}} = \frac{\partial \mathbf{I}_A^{-1}}{\partial T_i^{jkl}} \frac{\partial \vec{M}_A}{\partial \vec{\theta}_2} + \mathbf{I}_A^{-1} \frac{\partial^2 \vec{M}_A}{\partial \vec{\theta}_2 \partial T_i^{jkl}} \quad (\text{A.62})$$

$$\begin{aligned} \frac{\partial^2 \dot{\vec{\omega}}_1}{\partial \vec{\omega}_1 \partial T_i^{jkl}} &= \frac{\partial \mathbf{I}_A^{-1}}{\partial T_i^{jkl}} \left(\mathbf{I}_A \vec{\omega}_1 \right)^s + \mathbf{I}_A^{-1} \left(\frac{\partial \mathbf{I}_A}{\partial T_i^{jkl}} \vec{\omega}_1 \right)^s \\ &\quad - \frac{\partial \mathbf{I}_A^{-1}}{\partial T_i^{jkl}} \vec{\omega}_1^s \mathbf{I}_A - \mathbf{I}_A^{-1} \vec{\omega}_1^s \frac{\partial \mathbf{I}_A}{\partial T_i^{jkl}} \end{aligned} \quad (\text{A.63})$$

$$\frac{\partial^2 \dot{\vec{\omega}}_2}{\partial \vec{r} \partial T_i^{jkl}} = \frac{\partial \mathbf{I}_B^{-1}}{\partial T_i^{jkl}} \frac{\partial \vec{M}_B}{\partial \vec{r}} + \mathbf{I}_B^{-1} \frac{\partial^2 \vec{M}_B}{\partial \vec{r} \partial T_i^{jkl}} - \frac{\partial \mathbf{I}_A^{-1}}{\partial T_i^{jkl}} \frac{\partial \vec{M}_A}{\partial \vec{r}} - \mathbf{I}_A^{-1} \frac{\partial^2 \vec{M}_A}{\partial \vec{r} \partial T_i^{jkl}} \quad (\text{A.64})$$

$$\begin{aligned} \frac{\partial^2 \dot{\vec{\omega}}_2}{\partial \vec{\theta}_2 \partial T_i^{jkl}} &= \frac{\partial \mathbf{I}_B}{\partial T_i^{jkl}} \left(\vec{\omega}_1 + \vec{\omega}_2 \right) \vec{\omega}_1^s \frac{\partial \mathbf{I}_B^{-1}}{\partial \vec{\theta}_2} + \mathbf{I}_B \left(\vec{\omega}_1 + \vec{\omega}_2 \right) \vec{\omega}_1^s \frac{\partial^2 \mathbf{I}_B^{-1}}{\partial \vec{\theta}_2 \partial T_i^{jkl}} \\ &\quad - \frac{\partial \mathbf{I}_B^{-1}}{\partial T_i^{jkl}} \vec{\omega}_1^s \left(\vec{\omega}_1 + \vec{\omega}_2 \right) \frac{\partial \mathbf{I}_B}{\partial \vec{\theta}_2} - \mathbf{I}_B^{-1} \vec{\omega}_1^s \left(\vec{\omega}_1 + \vec{\omega}_2 \right) \frac{\partial^2 \mathbf{I}_B}{\partial \vec{\theta}_2 \partial T_i^{jkl}} \\ &\quad + \frac{\partial \vec{M}_B}{\partial T_i^{jkl}} \frac{\partial \mathbf{I}_B^{-1}}{\partial \vec{\theta}_2} + \vec{M}_B \frac{\partial^2 \mathbf{I}_B^{-1}}{\partial \vec{\theta}_2 \partial T_i^{jkl}} + \frac{\partial \mathbf{I}_B^{-1}}{\partial T_i^{jkl}} \frac{\partial \vec{M}_B}{\partial \vec{\theta}_2} \\ + \mathbf{I}_B^{-1} \frac{\partial^2 \vec{M}_B}{\partial \vec{\theta}_2 \partial T_i^{jkl}} &- \frac{\partial \dot{\mathbf{I}}_B}{\partial T_i^{jkl}} \left(\vec{\omega}_1 + \vec{\omega}_2 \right) \frac{\partial \mathbf{I}_B^{-1}}{\partial \vec{\theta}_2} - \dot{\mathbf{I}}_B \left(\vec{\omega}_1 + \vec{\omega}_2 \right) \frac{\partial^2 \mathbf{I}_B^{-1}}{\partial \vec{\theta}_2 \partial T_i^{jkl}} \\ &- \frac{\partial \mathbf{I}_B^{-1}}{\partial T_i^{jkl}} \left(\vec{\omega}_1 + \vec{\omega}_2 \right) \frac{\partial \dot{\mathbf{I}}_B}{\partial \vec{\theta}_2} - \mathbf{I}_B^{-1} \left(\vec{\omega}_1 + \vec{\omega}_2 \right) \frac{\partial^2 \dot{\mathbf{I}}_B}{\partial \vec{\theta}_2 \partial T_i^{jkl}} \\ &- \frac{\partial \mathbf{I}_A^{-1}}{\partial T_i^{jkl}} \frac{\partial \vec{M}_A}{\partial \vec{\theta}_2} - \mathbf{I}_A^{-1} \frac{\partial^2 \vec{M}_A}{\partial \vec{\theta}_2 \partial T_i^{jkl}} \end{aligned} \quad (\text{A.65})$$

$$\begin{aligned} \frac{\partial^2 \dot{\vec{\omega}}_2}{\partial \vec{\omega}_1 \partial T_i^{jkl}} &= \frac{\partial \mathbf{I}_B^{-1}}{\partial T_i^{jkl}} \left(\mathbf{I}_B \left(\vec{\omega}_1 + \vec{\omega}_2 \right) \right)^s + \mathbf{I}_B^{-1} \left(\frac{\partial \mathbf{I}_B}{\partial T_i^{jkl}} \left(\vec{\omega}_1 + \vec{\omega}_2 \right) \right)^s \\ &\quad - \frac{\partial \mathbf{I}_B^{-1}}{\partial T_i^{jkl}} \vec{\omega}_1^s \mathbf{I}_B - \mathbf{I}_B^{-1} \vec{\omega}_1^s \frac{\partial \mathbf{I}_B}{\partial T_i^{jkl}} - \frac{\partial \mathbf{I}_B^{-1}}{\partial T_i^{jkl}} \dot{\mathbf{I}}_B - \mathbf{I}_B^{-1} \frac{\partial \dot{\mathbf{I}}_B}{\partial T_i^{jkl}} \\ &- \frac{\partial \mathbf{I}_A^{-1}}{\partial T_i^{jkl}} \left(\mathbf{I}_A \vec{\omega}_1 \right)^s - \mathbf{I}_A^{-1} \left(\frac{\partial \mathbf{I}_A}{\partial T_i^{jkl}} \vec{\omega}_1 \right)^s + \frac{\mathbf{I}_A^{-1}}{\partial T_i^{jkl}} \vec{\omega}_1^s \mathbf{I}_A + \mathbf{I}_A^{-1} \vec{\omega}_1^s \frac{\partial \mathbf{I}_A}{\partial T_i^{jkl}} \end{aligned} \quad (\text{A.66})$$

$$\begin{aligned}
\frac{\partial^2 \dot{\vec{\omega}}_2}{\partial \vec{\omega}_2 \partial T_i^{jkl}} &= -\frac{\partial \mathbf{I}_B^{-1}}{\partial T_i^{jkl}} \vec{\omega}_1^s \mathbf{I}_B - \mathbf{I}_B^{-1} \vec{\omega}_1^s \frac{\partial \mathbf{I}_B}{\partial T_i^{jkl}} - \frac{\partial \mathbf{I}_B^{-1}}{\partial T_i^{jkl}} \dot{\mathbf{I}}_B - \mathbf{I}_B^{-1} \frac{\partial \dot{\mathbf{I}}_B}{\partial T_i^{jkl}} \\
&\quad - \frac{\partial \mathbf{I}_B^{-1}}{\partial T_i^{jkl}} (\vec{\omega}_1 + \vec{\omega}_2) \frac{\partial \dot{\mathbf{I}}_B}{\partial \vec{\omega}_2} - \mathbf{I}_B^{-1} (\vec{\omega}_1 + \vec{\omega}_2) \frac{\partial^2 \dot{\mathbf{I}}_B}{\partial \vec{\omega}_2 \partial T_i^{jkl}}
\end{aligned} \tag{A.67}$$

Appendix B

Restricted Full Three-Body Problem Partial Matrices

B.1 Dynamics Matrix

The dynamics matrix is necessary for numerical integration of the STM and MPSM. It is made up of several submatrices

$$\mathbf{A} = \begin{bmatrix}
 0_{3 \times 3} & 0_{3 \times 3} & 0_{3 \times 3} & I_{3 \times 3} & 0_{3 \times 3} & 0_{3 \times 3} & 0_{3 \times 3} & 0_{3 \times 3} \\
 0_{3 \times 3} & \frac{\partial \dot{\theta}_1}{\partial \theta_1} & 0_{3 \times 3} & 0_{3 \times 3} & \mathbf{B}_1 & 0_{3 \times 3} & 0_{3 \times 3} & 0_{3 \times 3} \\
 0_{3 \times 3} & 0_{3 \times 3} & \frac{\partial \dot{\theta}_2}{\partial \theta_2} & 0_{3 \times 3} & 0_{3 \times 3} & \mathbf{B}_2 & 0_{3 \times 3} & 0_{3 \times 3} \\
 \frac{\partial \ddot{r}}{\partial \vec{r}} & 0_{3 \times 3} & \frac{\partial \ddot{r}}{\partial \theta_2} & \frac{\partial \ddot{r}}{\partial \vec{r}} & \frac{\partial \ddot{r}}{\partial \omega_1} & 0_{3 \times 3} & 0_{3 \times 3} & 0_{3 \times 3} \\
 \frac{\partial \dot{\omega}_1}{\partial \vec{r}} & 0_{3 \times 3} & \frac{\partial \dot{\omega}_1}{\partial \theta_2} & 0_{3 \times 3} & \frac{\partial \dot{\omega}_1}{\partial \omega_1} & 0_{3 \times 3} & 0_{3 \times 3} & 0_{3 \times 3} \\
 \frac{\partial \dot{\omega}_2}{\partial \vec{r}} & 0_{3 \times 3} & \frac{\partial \dot{\omega}_2}{\partial \theta_2} & 0_{3 \times 3} & \frac{\partial \dot{\omega}_2}{\partial \omega_1} & \frac{\partial \dot{\omega}_2}{\partial \omega_2} & 0_{3 \times 3} & 0_{3 \times 3} \\
 0_{3 \times 3} & I_{3 \times 3} \\
 \frac{\partial \ddot{r}_{s/c}}{\partial \vec{r}} & \frac{\partial \ddot{r}_{s/c}}{\partial \theta_1} & \frac{\partial \ddot{r}_{s/c}}{\partial \theta_2} & 0_{3 \times 3} & 0_{3 \times 3} & 0_{3 \times 3} & \frac{\partial \ddot{r}_{s/c}}{\partial \vec{r}_{s/c}} & 0_{3 \times 3}
 \end{bmatrix} \tag{B.1}$$

Where the detailed equations for the submatrices are

$$\frac{\partial \dot{\theta}_i}{\partial \theta_i} = \frac{\partial \mathbf{B}_i}{\partial \theta_i} \vec{\omega}_i \tag{B.2}$$

$$\frac{\partial \ddot{\vec{r}}}{\partial \vec{r}} = \vec{r} \times \left(\mathbf{I}_A^{-1} \frac{\partial \vec{M}_A}{\partial \vec{r}} \right) - \left(\mathbf{I}_A^{-1} \left(\mathbf{I}_A \vec{\omega}_1 \right) \times \vec{\omega}_1 + \mathbf{I}_A^{-1} \vec{M}_A \right)^s - \vec{\omega}_1^s \vec{\omega}_1^s - \frac{1}{m} \frac{\partial^2 U}{\partial \vec{r}^2} \quad (\text{B.3})$$

$$\frac{\partial \ddot{\vec{r}}}{\partial \vec{\theta}_2} = - \left(\mathbf{I}_A^{-1} \frac{\partial \vec{M}_A}{\partial \vec{\theta}_2} \right)^s \vec{r} - \frac{1}{m} \frac{\partial^2 U}{\partial \vec{r} \partial \vec{\theta}_2} \quad (\text{B.4})$$

$$\frac{\partial \ddot{\vec{r}}}{\partial \vec{r}} = -2\vec{\omega}_1^s \quad (\text{B.5})$$

$$\frac{\partial \ddot{\vec{r}}}{\partial \vec{\omega}_1} = - \left(\mathbf{I}_A^{-1} \left(\mathbf{I}_A \vec{\omega}_1 \right)^s - \mathbf{I}_A^{-1} \vec{\omega}_1^s \mathbf{I}_A \right)^s \vec{r} + 2\vec{r}^s + \left(\vec{\omega}_1^s \vec{r} \right)^s + \vec{\omega}_1^s \vec{r}^s \quad (\text{B.6})$$

$$\frac{\partial \dot{\vec{\omega}}_1}{\partial \vec{r}} = \mathbf{I}_A^{-1} \frac{\partial \vec{M}_A}{\partial \vec{r}} \quad (\text{B.7})$$

$$\frac{\partial \dot{\vec{\omega}}_1}{\partial \vec{\theta}_2} = \mathbf{I}_A^{-1} \frac{\partial \vec{M}_A}{\partial \vec{\theta}_2} \quad (\text{B.8})$$

$$\frac{\partial \dot{\vec{\omega}}_1}{\partial \vec{\omega}_1} = \mathbf{I}_A^{-1} \left(\mathbf{I}_A \vec{\omega}_1 \right)^s - \mathbf{I}_A^{-1} \vec{\omega}_1^s \mathbf{I}_A \quad (\text{B.9})$$

$$\frac{\partial \dot{\vec{\omega}}_2}{\partial \vec{r}} = \mathbf{I}_B^{-1} \frac{\partial \vec{M}_B}{\partial \vec{r}} - \mathbf{I}_A^{-1} \frac{\partial \vec{M}_A}{\partial \vec{r}} \quad (\text{B.10})$$

$$\frac{\partial \dot{\vec{\omega}}_2}{\partial \vec{\theta}_2} = \frac{\partial \mathbf{I}_B^{-1}}{\partial \vec{\theta}_2} \left(\mathbf{I}_B \left(\vec{\omega}_1 + \vec{\omega}_2 \right) \times \vec{\omega}_1 \right) - \mathbf{I}_B^{-1} \vec{\omega}_1^s \left(\frac{\partial \mathbf{I}_B}{\partial \vec{\theta}_2} \left(\vec{\omega}_1 + \vec{\omega}_2 \right) \right) + \frac{\partial \mathbf{I}_B^{-1}}{\partial \vec{\theta}_2} \vec{M}_B \quad (\text{B.11})$$

$$+ \mathbf{I}_B^{-1} \frac{\partial \vec{M}_B}{\partial \vec{\theta}_2} + \frac{\partial \mathbf{I}_B^{-1}}{\partial \vec{\theta}_2} \dot{\mathbf{I}}_B \left(\vec{\omega}_1 + \vec{\omega}_2 \right) + \mathbf{I}_B^{-1} \frac{\partial \dot{\mathbf{I}}_B}{\partial \vec{\theta}_2} \left(\vec{\omega}_1 + \vec{\omega}_2 \right) - \mathbf{I}_A^{-1} \frac{\partial \vec{M}_A}{\partial \vec{\theta}_2}$$

$$\frac{\partial \dot{\vec{\omega}}_2}{\partial \vec{\omega}_1} = \mathbf{I}_B^{-1} \mathbf{I}_B \left(\vec{\omega}_1 + \vec{\omega}_2 \right) - \mathbf{I}_B^{-1} \vec{\omega}_1^s \mathbf{I}_B - \mathbf{I}_B^{-1} \dot{\mathbf{I}}_B - \mathbf{I}_A^{-1} \left(\mathbf{I}_A \vec{\omega}_1 \right)^s + \mathbf{I}_A^{-1} \vec{\omega}_1^s \mathbf{I}_A \quad (\text{B.12})$$

$$\frac{\partial \dot{\vec{\omega}}_2}{\partial \vec{\omega}_2} = -\mathbf{I}_B^{-1} \vec{\omega}_1^s \mathbf{I}_B + \mathbf{I}_B^{-1} \dot{\mathbf{I}}_B - \mathbf{I}_B^{-1} \frac{\partial \dot{\mathbf{I}}_B}{\partial \vec{\omega}_1} \left(\vec{\omega}_1 + \vec{\omega}_2 \right) \quad (\text{B.13})$$

$$\frac{\partial \ddot{\vec{r}}_{s/c}}{\partial \vec{r}} = -\mu \frac{\partial^2 U_{13}}{\partial \vec{r}_{A,s/c}^2} \mathbf{C}_A - \left(\mu - 1 \right) \frac{\partial^2 U_{23}}{\partial \vec{r}_{B,s/c}^2} \mathbf{C}_A \quad (\text{B.14})$$

$$\frac{\partial \ddot{\vec{r}}_{s/c}}{\partial \vec{\theta}_1} = -\frac{\partial^2 U_{13}}{\partial \vec{r}_{A,s/c} \partial \vec{\theta}_1} - \frac{\partial^2 U_{23}}{\partial \vec{r}_{B,s/c} \partial \vec{\theta}_1} - \mu \frac{\partial^2 U_{13}}{\partial \vec{r}_{A,s/c}^2} \frac{\partial \mathbf{C}_A}{\partial \vec{\theta}_1} \vec{r} - \left(\mu - 1 \right) \frac{\partial^2 U_{23}}{\partial \vec{r}_{B,s/c}^2} \frac{\partial \mathbf{C}_A}{\partial \vec{\theta}_1} \vec{r} \quad (\text{B.15})$$

$$\frac{\partial \ddot{\vec{r}}_{s/c}}{\partial \vec{\theta}_2} = -\frac{\partial^2 U_{23}}{\partial \vec{r}_{B,s/c} \partial \vec{\theta}_2} \quad (\text{B.16})$$

$$\frac{\partial \ddot{\vec{r}}_{s/c}}{\partial \vec{r}_{s/c}} = -\frac{\partial^2 U_{13}}{\partial \vec{r}_{A,s/c}^2} - \frac{\partial^2 U_{23}}{\partial \vec{r}_{B,s/c}^2} \quad (\text{B.17})$$

B.2 Mass Parameter Partial Matrix

The mass parameter partials matrix is necessary for numerical integration of the MPSM. It is made up of several submatrices

$$\mathbf{B} = \begin{bmatrix}
 0_{3 \times 1} & 0_{3 \times 1} & 0_{3 \times 3} & 0_{3 \times 3} \\
 0_{3 \times 1} & 0_{3 \times 1} & 0_{3 \times 3} & 0_{3 \times 3} \\
 0_{3 \times 1} & 0_{3 \times 1} & 0_{3 \times 3} & 0_{3 \times 3} \\
 \frac{\partial \ddot{\vec{r}}}{\partial M_A} & \frac{\partial \ddot{\vec{r}}}{\partial M_B} & \frac{\partial \ddot{\vec{r}}}{\partial \vec{T}_A} & \frac{\partial \ddot{\vec{r}}}{\partial \vec{T}_B} \\
 \frac{\partial \dot{\vec{\omega}}_1}{\partial M_A} & \frac{\partial \dot{\vec{\omega}}_1}{\partial M_B} & \frac{\partial \dot{\vec{\omega}}_1}{\partial \vec{T}_A} & \frac{\partial \dot{\vec{\omega}}_1}{\partial \vec{T}_B} \\
 \frac{\partial \dot{\vec{\omega}}_2}{\partial M_A} & \frac{\partial \dot{\vec{\omega}}_2}{\partial M_B} & \frac{\partial \dot{\vec{\omega}}_2}{\partial \vec{T}_A} & \frac{\partial \dot{\vec{\omega}}_2}{\partial \vec{T}_B} \\
 0_{3 \times 1} & 0_{3 \times 1} & 0_{3 \times 3} & 0_{3 \times 3} \\
 \frac{\partial \ddot{\vec{r}}_{s/c}}{\partial M_A} & \frac{\partial \ddot{\vec{r}}_{s/c}}{\partial M_B} & \frac{\partial \ddot{\vec{r}}_{s/c}}{\partial \vec{T}_A} & \frac{\partial \ddot{\vec{r}}_{s/c}}{\partial \vec{T}_B}
 \end{bmatrix} \quad (\text{B.18})$$

Where the detailed equations for the submatrices are

$$\frac{\partial \ddot{\vec{r}}}{\partial M_A} = \left(-\frac{\partial \mathbf{I}_A^{-1}}{\partial M_A} (\mathbf{I}_A \vec{\omega}_1)^s \vec{\omega}_1 - \mathbf{I}_A^{-1} \left(\frac{\partial \mathbf{I}_A}{\partial M_A} \vec{\omega}_1 \right)^s \vec{\omega}_1 \right)^s \vec{r} + \left(-\frac{\partial \mathbf{I}_A^{-1}}{\partial M_A} \vec{M}_A - \mathbf{I}_A^{-1} \frac{\partial \vec{M}_A}{\partial M_A} \right)^s \vec{r} + \frac{1}{M_A^2} \frac{\partial U}{\partial \vec{r}} - \frac{1}{m} \frac{\partial^2 U}{\partial \vec{r} \partial M_A} \quad (\text{B.19})$$

$$\frac{\partial \ddot{\vec{r}}}{\partial M_B} = -\left(\mathbf{I}_A^{-1} \frac{\partial \vec{M}_A}{\partial M_B} \right)^s \vec{r} + \frac{1}{M_B^2} \frac{\partial U}{\partial \vec{r}} - \frac{1}{m} \frac{\partial^2 U}{\partial \vec{r} \partial M_B} \quad (\text{B.20})$$

$$\frac{\partial \ddot{\vec{r}}}{\partial \vec{T}_A} = \left(-\frac{\partial \mathbf{I}_A^{-1}}{\partial \vec{T}_A} (\mathbf{I}_A \vec{\omega}_1)^s \vec{\omega}_1 - \mathbf{I}_A^{-1} \left(\frac{\partial \mathbf{I}_A}{\partial \vec{T}_A} \vec{\omega}_1 \right)^s \vec{\omega}_1 \right)^s \vec{r} + \left(-\frac{\partial \mathbf{I}_A^{-1}}{\partial \vec{T}_A} \vec{M}_A - \mathbf{I}_A^{-1} \frac{\partial \vec{M}_A}{\partial \vec{T}_A} \right)^s \vec{r} - \frac{1}{m} \frac{\partial^2 U}{\partial \vec{r} \partial \vec{T}_A} \quad (\text{B.21})$$

$$\frac{\partial \ddot{\vec{r}}}{\partial \vec{T}_B} = -\left(\mathbf{I}_A^{-1} \frac{\partial \vec{M}_A}{\partial \vec{T}_B} \right)^s \vec{r} + \frac{1}{M_B^2} \frac{\partial U}{\partial \vec{r}} - \frac{1}{m} \frac{\partial^2 U}{\partial \vec{r} \partial \vec{T}_B} \quad (\text{B.22})$$

$$\frac{\partial \dot{\vec{\omega}}_1}{\partial M_A} = \frac{\partial \mathbf{I}_A^{-1}}{\partial M_A} (\mathbf{I}_A \vec{\omega}_1)^s \vec{\omega}_1 + \mathbf{I}_A^{-1} \left(\frac{\partial \mathbf{I}_A}{\partial M_A} \vec{\omega}_1 \right)^s \vec{\omega}_1 + \frac{\partial \mathbf{I}_A^{-1}}{\partial M_A} \vec{M}_A + \mathbf{I}_A^{-1} \frac{\partial \vec{M}_A}{\partial M_A} \quad (\text{B.23})$$

$$\frac{\partial \dot{\vec{\omega}}_1}{\partial M_B} = \mathbf{I}_A^{-1} \frac{\partial \vec{M}_A}{\partial M_B} \quad (\text{B.24})$$

$$\frac{\partial \dot{\vec{\omega}}_1}{\partial \vec{T}_A} = \frac{\partial \mathbf{I}_A^{-1}}{\partial \vec{T}_A} (\mathbf{I}_A \vec{\omega}_1)^s \vec{\omega}_1 + \mathbf{I}_A^{-1} \left(\frac{\partial \mathbf{I}_A}{\partial \vec{T}_A} \vec{\omega}_1 \right)^s \vec{\omega}_1 + \frac{\partial \mathbf{I}_A^{-1}}{\partial \vec{T}_A} \vec{M}_A - \mathbf{I}_A^{-1} \frac{\partial \vec{M}_A}{\partial \vec{T}_A} \quad (\text{B.25})$$

$$\frac{\partial \dot{\vec{\omega}}_1}{\partial \vec{T}_B} = \mathbf{I}_A^{-1} \frac{\partial \vec{M}_A}{\partial \vec{T}_B} \quad (\text{B.26})$$

$$\begin{aligned} \frac{\partial \dot{\vec{\omega}}_2}{\partial M_A} = & -\frac{\partial \mathbf{I}_A^{-1}}{\partial M_A} \left(\mathbf{I}_A \vec{\omega}_1 \right)^s \vec{\omega}_1 - \mathbf{I}_A^{-1} \left(\frac{\partial \mathbf{I}_A}{\partial M_A} \vec{\omega}_1 \right)^s \vec{\omega}_1 + \mathbf{I}_B^{-1} \frac{\partial \vec{M}_B}{\partial M_A} - \frac{\partial \mathbf{I}_A^{-1}}{\partial M_A} \vec{M}_A \\ & - \mathbf{I}_A^{-1} \frac{\partial \vec{M}_A}{\partial M_A} \end{aligned} \quad (\text{B.27})$$

$$\begin{aligned} \frac{\partial \dot{\vec{\omega}}_2}{\partial M_B} = & \frac{\partial \mathbf{I}_B^{-1}}{\partial M_B} \left(\mathbf{I}_B (\vec{\omega}_1 + \vec{\omega}_2) \right)^s \vec{\omega}_1 + \mathbf{I}_B^{-1} \left(\frac{\partial \mathbf{I}_B}{\partial M_B} (\vec{\omega}_1 + \vec{\omega}_2) \right)^s \vec{\omega}_1 \\ & + \frac{\partial \mathbf{I}_B^{-1}}{\partial M_B} \left(\vec{M}_B - \mathbf{I}_B (\vec{\omega}_1 + \vec{\omega}_2) \right) + \mathbf{I}_B^{-1} \left(\frac{\partial \vec{M}_B}{\partial M_B} - \frac{\partial \mathbf{I}_B}{\partial M_B} (\vec{\omega}_1 + \vec{\omega}_2) \right) \\ & - \mathbf{I}_A^{-1} \frac{\partial \vec{M}_A}{\partial M_B} \end{aligned} \quad (\text{B.28})$$

$$\begin{aligned} \frac{\partial \dot{\vec{\omega}}_2}{\partial \vec{T}_A} = & -\frac{\partial \mathbf{I}_A^{-1}}{\partial \vec{T}_A} \left(\mathbf{I}_A \vec{\omega}_1 \right)^s \vec{\omega}_1 - \mathbf{I}_A^{-1} \left(\frac{\partial \mathbf{I}_A}{\partial \vec{T}_A} \vec{\omega}_1 \right)^s \vec{\omega}_1 + \mathbf{I}_B^{-1} \frac{\partial \vec{M}_B}{\partial \vec{T}_A} - \frac{\partial \mathbf{I}_A^{-1}}{\partial \vec{T}_A} \vec{M}_A \\ & - \mathbf{I}_A^{-1} \frac{\partial \vec{M}_A}{\partial M_A} \end{aligned} \quad (\text{B.29})$$

$$\begin{aligned} \frac{\partial \dot{\vec{\omega}}_2}{\partial \vec{T}_B} = & \frac{\partial \mathbf{I}_B^{-1}}{\partial \vec{T}_B} \left(\mathbf{I}_B (\vec{\omega}_1 + \vec{\omega}_2) \right)^s \vec{\omega}_1 + \mathbf{I}_B^{-1} \left(\frac{\partial \mathbf{I}_B}{\partial \vec{T}_B} (\vec{\omega}_1 + \vec{\omega}_2) \right)^s \vec{\omega}_1 \\ & + \frac{\partial \mathbf{I}_B^{-1}}{\partial \vec{T}_B} \left(\vec{M}_B - \mathbf{I}_B (\vec{\omega}_1 + \vec{\omega}_2) \right) + \mathbf{I}_B^{-1} \left(\frac{\partial \vec{M}_B}{\partial \vec{T}_B} - \frac{\partial \mathbf{I}_B}{\partial \vec{T}_B} (\vec{\omega}_1 + \vec{\omega}_2) \right) \\ & - \mathbf{I}_A^{-1} \frac{\partial \vec{M}_A}{\partial \vec{T}_B} \end{aligned} \quad (\text{B.30})$$

$$\frac{\partial \ddot{\vec{r}}_{s/c}}{\partial M_A} = -\frac{\partial^2 U_{13}}{\partial \vec{r}_{A,s/c} \partial M_A} \quad (\text{B.31})$$

$$\frac{\partial \ddot{\vec{r}}_{s/c}}{\partial M_B} = -\frac{\partial^2 U_{23}}{\partial \vec{r}_{B,s/c} \partial M_B} \quad (\text{B.32})$$

$$\frac{\partial \ddot{\vec{r}}_{s/c}}{\partial \vec{T}_A} = -\frac{\partial^2 U_{13}}{\partial \vec{r}_{A,s/c} \partial \vec{T}_A} \quad (\text{B.33})$$

$$\frac{\partial \ddot{\vec{r}}_{s/c}}{\partial \vec{T}_B} = -\frac{\partial^2 U_{23}}{\partial \vec{r}_{B,s/c} \partial \vec{T}_B} \quad (\text{B.34})$$

B.3 Observation-State Matrix

$$H_x = \begin{bmatrix} \vec{0}_{1x3} & \vec{0}_{1x3} & \vec{0}_{1x3} & \vec{0}_{1x3} & \vec{0}_{1x3} & \vec{0}_{1x3} & \frac{\partial \rho}{\partial \vec{r}_{s/c}} & \vec{0}_{1x3} \\ \vec{0}_{1x3} & \vec{0}_{1x3} & \vec{0}_{1x3} & \vec{0}_{1x3} & \vec{0}_{1x3} & \vec{0}_{1x3} & \frac{\partial \dot{\rho}}{\partial \vec{r}_{s/c}} & \frac{\partial \dot{\rho}}{\partial \vec{r}_{s/c}} \\ \frac{\partial \hat{\sigma}_1}{\partial \vec{r}} & \frac{\partial \hat{\sigma}_1}{\partial \theta_1} & \vec{0}_{3x3} & \vec{0}_{3x3} & \vec{0}_{3x3} & \vec{0}_{3x3} & \frac{\partial \hat{\sigma}_1}{\partial \vec{r}_{s/c}} & \vec{0}_{3x3} \\ \frac{\partial \hat{\sigma}_2}{\partial \vec{r}} & \frac{\partial \hat{\sigma}_2}{\partial \theta_1} & \frac{\partial \hat{\sigma}_2}{\partial \theta_2} & \vec{0}_{3x3} & \vec{0}_{3x3} & \vec{0}_{3x3} & \frac{\partial \hat{\sigma}_2}{\partial \vec{r}_{s/c}} & \vec{0}_{3x3} \\ \frac{\partial l_1}{\partial \vec{r}} & \vec{0}_{1x3} & \vec{0}_{1x3} & \vec{0}_{1x3} & \vec{0}_{1x3} & \vec{0}_{1x3} & \frac{\partial l_1}{\partial \vec{r}_{s/c}} & \vec{0}_{1x3} \\ \frac{\partial l_2}{\partial \vec{r}} & \vec{0}_{1x3} & \vec{0}_{1x3} & \vec{0}_{1x3} & \vec{0}_{1x3} & \vec{0}_{1x3} & \frac{\partial l_2}{\partial \vec{r}_{s/c}} & \vec{0}_{1x3} \end{bmatrix} \quad (\text{B.35})$$

Where the detailed equations of the submatrices are

$$\frac{\partial \rho}{\partial \vec{r}_{s/c}} = \frac{\vec{r}_{s/c}^T - \vec{r}_{\oplus}^T}{|\vec{r}_{s/c} - \vec{r}_{\oplus}|} \quad (\text{B.36})$$

$$\frac{\partial \dot{\rho}}{\partial \vec{r}_{s/c}} = \frac{-\dot{(\vec{r}_{s/c} - \vec{r}_{\oplus})} \odot (\vec{r}_{s/c} - \vec{r}_{\oplus}) \odot (\dot{(\vec{r}_{s/c} - \vec{r}_{\oplus})})}{|\vec{r}_{s/c} - \vec{r}_{\oplus}|^3} + \frac{\dot{\vec{r}}_{s/c} - \dot{\vec{r}}_{\oplus}}{|\vec{r}_{s/c} - \vec{r}_{\oplus}|} \quad (\text{B.37})$$

$$\frac{\partial \dot{\rho}}{\partial \dot{\vec{r}}_{s/c}} = \frac{\vec{r}_{s/c} - \vec{r}_{\oplus}}{|\vec{r}_{s/c} - \vec{r}_{\oplus}|} \quad (\text{B.38})$$

$$\frac{\partial \hat{\sigma}_1}{\partial \vec{r}} = \mathbf{C}_A^T \left(\frac{\mu \mathbf{I}_{3x3}}{\mu \vec{r} + \vec{r}_{s/c}} - \mu \frac{(\mu \vec{r} + \vec{r}_{s/c})(\mu \vec{r} + \vec{r}_{s/c})^T}{|\mu \vec{r} + \vec{r}_{s/c}|^3} \right) \quad (\text{B.39})$$

$$\frac{\partial \hat{\sigma}_1}{\partial \theta_1} = \frac{\partial \mathbf{C}_A^T}{\partial \theta_1} (\mu \vec{r} + \vec{r}_{s/c}) \quad (\text{B.40})$$

$$\frac{\partial \hat{\sigma}_1}{\partial \vec{r}_{s/c}} = \mathbf{C}_A^T \left(\frac{\mathbf{I}_{3x3}}{\mu \vec{r} + \vec{r}_{s/c}} - \frac{(\mu \vec{r} + \vec{r}_{s/c})(\mu \vec{r} + \vec{r}_{s/c})^T}{|\mu \vec{r} + \vec{r}_{s/c}|^3} \right) \quad (\text{B.41})$$

$$\frac{\partial \hat{\sigma}_2}{\partial \vec{r}} = \mathbf{C}^T \mathbf{C}_A^T \left(\frac{(\mu - 1) \mathbf{I}_{3 \times 3}}{(\mu - 1) \vec{r} + \vec{r}_{s/c}} - (\mu - 1) \frac{((\mu - 1) \vec{r} + \vec{r}_{s/c})((\mu - 1) \vec{r} + \vec{r}_{s/c})^T}{|(\mu - 1) \vec{r} + \vec{r}_{s/c}|^3} \right) \quad (\text{B.42})$$

$$\frac{\partial \hat{\sigma}_2}{\partial \theta_1} = \mathbf{C}^T \frac{\partial \mathbf{C}_A^T}{\partial \theta_1} ((\mu - 1) \vec{r} + \vec{r}_{s/c}) \quad (\text{B.43})$$

$$\frac{\partial \hat{\sigma}_2}{\partial \theta_2} = \frac{\partial \mathbf{C}^T}{\partial \theta_2} \mathbf{C}_A^T ((\mu - 1) \vec{r} + \vec{r}_{s/c}) \quad (\text{B.44})$$

$$\frac{\partial \hat{\sigma}_2}{\partial \vec{r}_{s/c}} = \mathbf{C}^T \mathbf{C}_A^T \left(\frac{\mathbf{I}_{3 \times 3}}{(\mu - 1) \vec{r} + \vec{r}_{s/c}} - \frac{((\mu - 1) \vec{r} + \vec{r}_{s/c})((\mu - 1) \vec{r} + \vec{r}_{s/c})^T}{|(\mu - 1) \vec{r} + \vec{r}_{s/c}|^3} \right) \quad (\text{B.45})$$

$$\frac{\partial l_1}{\partial \vec{r}} = \mu \frac{(\mu \vec{r} + \vec{r}_{s/c})}{|\mu \vec{r} + \vec{r}_{s/c}|} \quad (\text{B.46})$$

$$\frac{\partial l_1}{\partial \vec{r}_{s/c}} = \frac{(\mu \vec{r} + \vec{r}_{s/c})}{|\mu \vec{r} + \vec{r}_{s/c}|} \quad (\text{B.47})$$

$$\frac{\partial l_2}{\partial \vec{r}} = (\mu - 1) \frac{((\mu - 1) \vec{r} + \vec{r}_{s/c})}{|(\mu - 1) \vec{r} + \vec{r}_{s/c}|} \quad (\text{B.48})$$

$$\frac{\partial l_2}{\partial \vec{r}_{s/c}} = \frac{((\mu - 1) \vec{r} + \vec{r}_{s/c})}{|(\mu - 1) \vec{r} + \vec{r}_{s/c}|} \quad (\text{B.49})$$

B.4 Observation-Consider Parameter Matrix

$$H_c = \begin{bmatrix} 0 & 0 & \vec{0}_{1 \times 3} & \vec{0}_{1 \times 3} \\ 0 & 0 & \vec{0}_{1 \times 3} & \vec{0}_{1 \times 3} \\ \frac{\partial \hat{\sigma}_1}{\partial M_A} & \frac{\partial \hat{\sigma}_1}{\partial M_B} & \vec{0}_{3 \times 3} & \vec{0}_{3 \times 3} \\ \frac{\partial \hat{\sigma}_2}{\partial M_A} & \frac{\partial \hat{\sigma}_2}{\partial M_B} & \vec{0}_{3 \times 3} & \vec{0}_{3 \times 3} \\ \frac{\partial l_1}{\partial M_A} & \frac{\partial l_1}{\partial M_B} & \vec{0}_{3 \times 3} & \vec{0}_{3 \times 3} \\ \frac{\partial l_2}{\partial M_A} & \frac{\partial l_2}{\partial M_B} & \vec{0}_{3 \times 3} & \vec{0}_{3 \times 3} \end{bmatrix} \quad (\text{B.50})$$

Where the detailed equations of the submatrices are

$$\frac{\partial \hat{\sigma}_1}{\partial M_A} = \frac{-M_B}{(M_A + M_B)^2} \mathbf{C}_A^T \left(\frac{\vec{r}}{|\mu \vec{r} + \vec{r}_{s/c}|} - \frac{(\mu \vec{r} + \vec{r}_{s/c}) \odot (\mu \vec{r} + \vec{r}_{s/c}) \vec{r}^T}{|\mu \vec{r} + \vec{r}_{s/c}|^3} \right) \quad (\text{B.51})$$

$$\frac{\partial \hat{\sigma}_1}{\partial M_B} = \frac{M_A}{(M_A + M_B)^2} \mathbf{C}_A^T \left(\frac{\vec{r}}{|\mu \vec{r} + \vec{r}_{s/c}|} - \frac{(\mu \vec{r} + \vec{r}_{s/c}) \odot (\mu \vec{r} + \vec{r}_{s/c}) \vec{r}^T}{|\mu \vec{r} + \vec{r}_{s/c}|^3} \right) \quad (\text{B.52})$$

$$\frac{\partial \hat{\sigma}_2}{\partial M_A} = \frac{-M_B}{(M_A + M_B)^2} \mathbf{C}^T \mathbf{C}_A^T \left(\frac{\vec{r}}{|(\mu - 1)\vec{r} + \vec{r}_{s/c}|} - \frac{((\mu - 1)\vec{r} + \vec{r}_{s/c}) \odot ((\mu - 1)\vec{r} + \vec{r}_{s/c})^T \vec{r}}{|(\mu - 1)\vec{r} + \vec{r}_{s/c}|^3} \right) \quad (\text{B.53})$$

$$\frac{\partial \hat{\sigma}_2}{\partial M_B} = \frac{M_A}{(M_A + M_B)^2} \mathbf{C}^T \mathbf{C}_A^T \left(\frac{\vec{r}}{|(\mu - 1)\vec{r} + \vec{r}_{s/c}|} - \frac{((\mu - 1)\vec{r} + \vec{r}_{s/c}) \odot ((\mu - 1)\vec{r} + \vec{r}_{s/c})^T \vec{r}}{|(\mu - 1)\vec{r} + \vec{r}_{s/c}|^3} \right) \quad (\text{B.54})$$

$$\frac{\partial l_1}{\partial M_A} = \frac{-M_B}{(M_A + M_B)^2} \left(\frac{(\mu \vec{r} + \vec{r}_{s/c})^T \vec{r}}{|\mu \vec{r} + \vec{r}_{s/c}|} \right) \quad (\text{B.55})$$

$$\frac{\partial l_1}{\partial M_B} = \frac{M_A}{(M_A + M_B)^2} \left(\frac{(\mu \vec{r} + \vec{r}_{s/c})^T \vec{r}}{|\mu \vec{r} + \vec{r}_{s/c}|} \right) \quad (\text{B.56})$$

$$\frac{\partial l_2}{\partial M_A} = \frac{-M_B}{(M_A + M_B)^2} \left(\frac{((\mu - 1)\vec{r} + \vec{r}_{s/c})^T \vec{r}}{|(\mu - 1)\vec{r} + \vec{r}_{s/c}|} \right) \quad (\text{B.57})$$

$$\frac{\partial l_2}{\partial M_B} = \frac{M_A}{(M_A + M_B)^2} \left(\frac{((\mu - 1)\vec{r} + \vec{r}_{s/c})^T \vec{r}}{|(\mu - 1)\vec{r} + \vec{r}_{s/c}|} \right) \quad (\text{B.58})$$

Appendix C

General Use Binary Asteroid Simulator

As a part of the analysis for this paper we developed a tool for dynamical propagation of binary asteroids of arbitrary shape and expansion order using the Hou mutual gravity potential described in Ch. 2 [28]. We have provided the software tool for free use at <https://github.com/alex-b-davis/gubas>. The tool, referred to as the General Use Binary Asteroid Simulator, is intended to provide the planetary science community with an easily used, fast, and high fidelity simulation tool for the numerical integration of binary asteroid dynamics. It does not include the tools for the fundamental frequency analysis performed in this paper.

The software was designed and implemented to be highly modular to enable a wide set of uses and allow for easy integration into larger tool sets. For this reason the architecture was centered around a C++ executable wrapped in a Python shell. The C++ executable performs the numerical integration and calculation of the inertia integrals while the Python wrapper pre-processes user input from a configuration file to initialize the executable and post-processes the results. This approach allows the user to easily modify the Python shell script to fit their needs. In the standard architecture all interactions are handles through the configuration file and a single command line call to initialize the process. While the software and a detailed user guide can be found by following the github link, Fig. C.1 shows a basic flowchart of the software process.

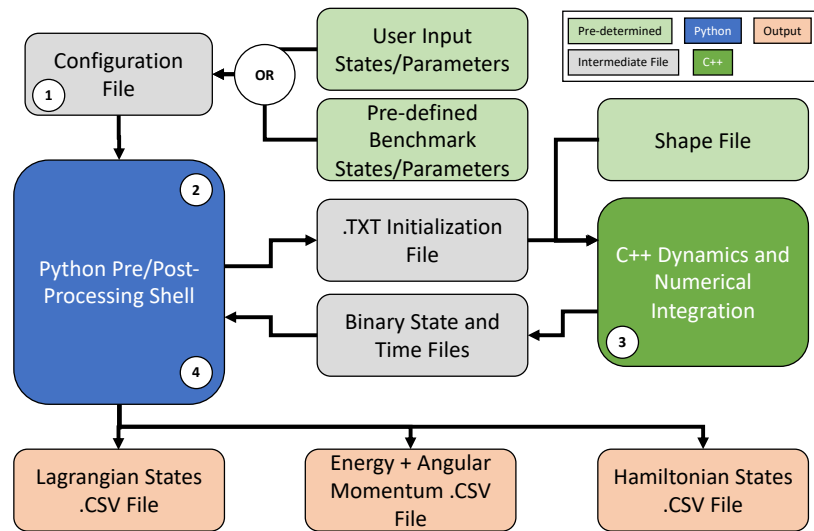


Figure C.1: General Use Binary Asteroid Simulator Software Flowchart